DAFTAR ISI

DARI REDAKSI

   Sidang Pembaca yang kami hormati,
Puji syukur, kita panjatkan kehadirat Tuhan Yang Maha Esa atas rahmat dan karunia-Nya, sehingga Jurnal Teknologi Dirgantara Vol. 18, No. 2, Desember 2020 hadir ke hadapan sidang pembaca dengan mengetengahkan 8 (delapan) artikel sebagai berikut, Stability and controllability analysis on linearized dynamic system equation of motion of lsu 05-ng using kalman rank condition method ditulis Angga Septiyana, Kurnia Hidayat, Ardian Rizaldi, Prasetyo Ardi Probo Suseno, Eries Bagita Jayanti, Novita Atmasari, M. Luthfi Ramadiansyah, Redha Akbar Ramadhan. Numerical investigation on the fuselage airframe of LSU 05 NG ditulis oleh M. Hafid, Abian Nurrohmad, Redha Akbar Ramadhan. A finite element analysis of critical buckling load of composite plate after low velocity impact ditulis oleh Redha Akbar Ramadhan, M. Giri Suada, Hendri Syamsudin. Effect of isomer composition of hydroxyl terminated polybutadiene (htpb) in low shear flow behavior ditulis oleh Afni Restasari, Luthfia Hajar Abdillah, Retno Ardianingsih, Rika Suwana Budi. Comparative study of wing lift distribution analysis using numerical method ditulis oleh Angga Septiyana, Kurnia Hidayat, Ardian Rizaldi, Yusuf Giri Wijaya. Departure trajectory optimization for noise abatement procedure in soekarno-hatta international airport ditulis oleh Vincentius N.s. Suryo, Benedikt Grüter, Johannes Diepolder, Neno Ruseno, Florian Holzapfel. Design of force measuring system on main landing gear weight drop testing machine for the application of lsu series ditulis oleh Yusuf Giri Wijaya, Abian Nurrohmad. Ballistic Flight And Control Simulation Of RKX20TJ/Booster During Boost And Climb-phases ditulis oleh Hakiki.

   Demikianlah 8 artikel yang kami sajikan dalam Jurnal Teknologi Dirgantara Vol. 18, No. 2, Desember 2020. Seperti diketahui jurnal ini memuat hasil penelitian di bidang teknologi dirgantara dalam bahasa Indonesia atau bahasa Inggris dan terbuka bagi ilmuwan-ilmuwan dalam dan luar negeri. Semoga sidang pembaca dapat mengambil manfaatnya.

Bogor, Desember 2020

                          Redaksi

STABILITY AND CONTROLLABILITY ANALYSIS ON LINEARIZED DYNAMIC SYSTEM EQUATION OF MOTION OF LSU 05-NG USING KALMAN RANK CONDITION METHOD

Angga Septiyana[1], Kurnia Hidayat, Ardian Rizaldi, Prasetyo Ardi Probo Suseno, Eries Bagita Jayanti, Novita Atmasari, M. Luthfi Ramadiansyah, Redha Akbar Ramadhan

[1]Aeronautics Technology Center, LAPAN

[1]e-mail: angga.septiyana@lapan.go.id

ABSTRACT

This paper discusses the stability and controllability of the dynamic system of the LAPAN Surveillance UAV 05-NG (LSU 05-NG) aircraft equation. This analysis is important to determine the performance of aircraft when carrying out missions such as photography, surveillance, observation, and as a scientific platform to test communication-based on satellite. Before analyzing the dynamic system, first arranged equations of motion of the plane which include the force equation, moment equation, and kinematics equation. The equation of motion of the aircraft obtained by the equation of motion of the longitudinal and lateral dimensions. Each of these equations of motion will be linearized to obtain state-space conditions. In this state space, A, B, and C are linear matrices that will be obtained in the time domain. Stability analysis using eigenvalue method and controllability analysis using Kalman Rank Condition method. The results of the analysis of matrices A, B, and C show that the dynamic system in the LSU 05-NG motion equation is a stable system on the longitudinal dimension but the lateral dimension on the unstable spiral mode. As for the analysis of the control of both the longitudinal and lateral dimensions, the results show that the system is controlled.

Keywords: *stability, controllability, , Kalman rank condition, dynamical system.*

1 Introduction

The development of unmanned aircraft in various countries is quite significant and the unmanned aircraft is widely applied to the needs of a country. Currently UAV (Unmanned Aerial Vehicle) or Drone aircraft have been used in various applications such as military industry, commercial cargo transportation, and mapping (Parmar & Acharya, 2015). In Indonesia, the development of UAV technology is also developing rapidly and its application is not inferior to other countries. Therefore, as a government agency engaged in the world of aeronautics, Pusat Teknologi Penerbangan continues to conduct research and innovation. One focus of work carried out is the development or development of unmanned aircraft. Until now, there are several variants of UAV owned. From the smallest to the biggest. One of the drones developed was the LAPAN Surveillance UAV 05 Next Generation (LSU 05-NG) aircraft.

LAPAN Surveillance UAV 05 Next Generation (LSU-05 NG) is an unmanned aircraft capable of accommodating large loads (maximum 30 kg) that has missions for research, observation, patrol, surveillance, and SAR activities. The main mission of this aircraft is to support

aerial photography activities by carrying loads in the form of optical devices. In the future, this aircraft will also be used as a scientific platform to test the satellite-based communication system developed by the LAPAN Pustekbang and can also be used for border surveillance (Rizaldi, 2019)

Before carrying out this mission, it is necessary to analyze the stability, control, and observability of the state space matrices. This simulation analysis is carried out to ensure that the LSU 05-NG is stable and can be controlled properly when there is interference. Previous research on stability analysis on UAVs has been conducted by (Purwanto, 2012). The analysis carried out is a dynamic stability analysis on the UAV. The results obtained that the UAV has dynamically stable properties in the longitudinal and lateral dimensions. In addition, an analysis of static stability has also been carried out by (Sugandi *et al.*, 2018). The study was conducted on a UAV with a tandem model or commonly called a tandem wing UAV. Research related to stability is also widely carried out as conducted by (Boschetti & Cárdenas, 2012), (Boschetti *et al.*, 2010) and (Cardenas *et al.*, 2004). On the other hand, research about controllability and observability has been carried out. (Younus & Ur Rahman, 2014) conducted research on control and accuracy to obtain solutions from dynamic systems on voltera type nonlinear matrices. Also conducted by (Tian *et al.*, 2019) research related to control and observation. Research conducted on a linear dynamic system on a multi-agent system.

In this study an analysis of the A, B, C, and D lines that have been linearized in the state space state. The purpose of this analysis is to find out the stability and controllability of the dynamic system that is formed from the equation of the linearized motion of the aircraft.

2   Methodology
2.1 Stability

In designing an aircraft, the stability analysis is very important to know the aircraft's ability to carry out the mission and the aircraft's attitude when there is interference. Stability analysis on aircraft includes static and dynamic stability analysis. Static stability of an aircraft is generally the first type of stability evaluated by a designer. The static stability criteria for the three aircraft rotation modes (pitch, roll, and yaw) must be considered (Yechout, 2003). In addition, it needs to be evaluated for aircraft dynamic stability. The dynamic stability of the aircraft focuses on the time domain when the aircraft is moving and gets outside interference when in a state of balance or trim condition. An analysis of the aircraft's dynamic stability needs to be carried out to determine the aircraft's handling quality and features designed for the aircraft to run well or not when carrying out the mission. The basis for knowing this dynamic stability, the first thing to do is to arrange a plane motion differential equation or equation of motion (EOM). Then from the results of EOM compilation is carried out linearization and will get a matrices A, B, and C in the state space. The matrices will find the roots of their characteristics which will be used to determine stability.

Theorem (1): Given a system of differential equations

$$\dot{x} = Ax \qquad\qquad (2\text{-}1)$$

where A is matrices of size $n \times n$ and has an eigenvalue $\lambda_1, \lambda_2 \cdots\cdots, \lambda_i$ with $i \leq n$. The differential equation system is said to be stable at $x = 0$ if and only if the characteristic roots of matrices A in the real domain are negative or $R_e \lambda_i < 0$. (George, 2015).

2.2 Controllability

Given a system of linear differential equations in the time domain

$$\dot{x}(t) = Ax(t) + Bu(t), \ \ x(t_0) = x_0 \qquad (2\text{-}2)$$

$$y(t) = Cx(t) + Du(t) \qquad (2\text{-}3)$$

where matrices A, B, C dan D have size $n{\times}n, n{\times}r, m{\times}n,$ dan $n{\times}r$.

Theorem (2) Kalman rank conditon: The differential equation system in Eq. (2-2) dan (2-3) s said to be controlled at intervals $[t_0, t_1]$ if and only if the control matrices

$$[B \ \ AB \ \cdots \ A^{n-1}B] \qquad (2\text{-}4)$$

with size $n{\times}nm$ has rank as much n. (Davis *et al.*, 2009) Theorem 2 shows that the system is said to be controllable output if with the unconstrained control vector $u(t)$ Theorem 2 shows that the system is said to be controllable output if with the unconstrained control vector $x(t_0)$ to the condition $x(t_1)$ in interval $t_0 \leq t \leq t_1$.

Based on the understanding of Theorem 2-2 it is important to know that any initial and final state consisting of n components and if all components of the initial state can be controlled to n components that correspond to the final state, then the system can be controlled.

Whereas with the existence of an unrestricted u (t) controller, nothing is required except to transfer just any initial state that is given to any desired final state at a finite time interval (Subiono, 2013)

2.3 Equation of Motion

Airplanes can move on the X, Y, and Z axes. Airplane movements include rolling, pitching, and yawing. Rolling is a rolling motion made by aircraft on the longitudinal axis caused by the aileron control plane. Pitching is a nodding motion down and up on the lateral axis due to the elevator control plane. While yawing is a turning motion on the horizontal body caused by rudder control. LSU 05-NG has flaps for increase lift when taking off. In general, the anatomy of LSU 05-NG is given at Figure 2 - 1.
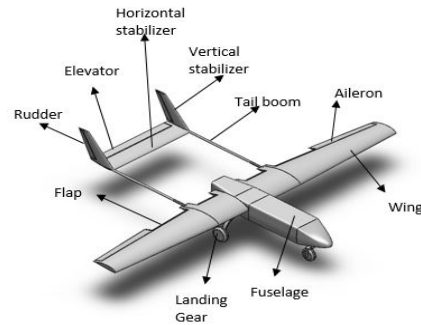
Figure 2-1: Anatomy of LSU 05-NG

To get the equation of motion aircraft, used *first-principle modelling* (Adiprawita *et al.*, 2008). This approach is used by involving the basic equations of mechanics and aerodynamics. This reduction involves a decrease in the force equation, the flight kinematics equation and the moment equation.
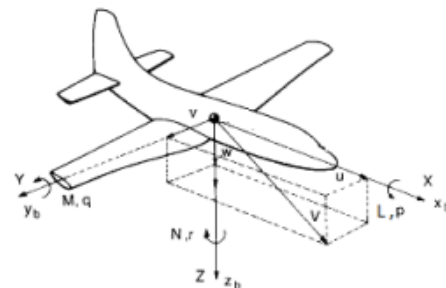
Figure 2-1: Definition of force, moment and speed on airframe (Nelson, 1989)

Based on Figure 2-2, the equation of force on the plane at coordinates X, Y and Z is the sum of the forces that occur on the plane which include gravity, thrust, and aerodynamic forces (Luckner, 2007). Mathematically, the force equation can be written as follows

$$m(\dot{u} + qw - rv) = -mg\sin\Theta \quad (2\text{-}5)$$
$$+ F_{Ax} + F_{fx}$$

$$m(\dot{v} + ru - pw) = mg\sin\Phi\cos\Theta \quad (2\text{-}6)$$
$$+ F_{Ay} + F_{fy}$$

$$m(\dot{w} + pv - qu) \quad (2\text{-}7)$$
$$= mg\cos\Phi\cos\Theta + F_{Az} + F_{fz}$$

The moment equation in the aerospace vehicle is often called the rotational equation and mathematically the moment equation can be written as follows (Ulu s & Ikbal, 2019)

$$\dot{p}I_x + qr(I_x - I_y) - (pq + \dot{r})I_{xz} \quad (2\text{-}8)$$
$$= L_A + L_f$$

$$\dot{q}I_y - pr(I_z - I_x) + (p^2 - r^2)I_{xz} \quad (2\text{-}9)$$
$$= M_A + M_f$$

$$\dot{r}I_z + pq(I_y - I_x) + (qr - \dot{p})I_{xz} \quad (2\text{-}10)$$
$$= N_A + N_f$$

To analyze an aircraft's dynamic response, rotational angle motion is used on an aircraft that is (Φ Θ Ψ) which respectively states roll, pitch, and yaw (Ahmed *et al.*, 2015). The relationship between angular velocity and rotation angle is expressed in the following mathematical form

$$\dot{\Phi} = p + (q\sin\Phi + r\cos\Phi)\tan\Theta \quad (2\text{-}11)$$

$$\dot{\Theta} = q\cos\Phi - r\sin\Phi \quad (2\text{-}12)$$

$$\dot{\Psi} = q\sin\Phi\sec\Theta + r\cos\Phi\sec\Theta \quad (2\text{-}13)$$

2.4 State Space Representations of the UAV Model

In this section, the equation of motion in the longitudinal and lateral dimensions is obtained from Eq. (2-5) to (2-13). Then those equation is linearized. Those longitudinal and lateral equations are obtained in the state sapce. Equations in the form of state space are

84

needed to develop the transfer function for each state variable and control input. For longitudinal equations in state space conditions are given as follows

$$\begin{pmatrix} \dot{u} \\ \dot{w} \\ \dot{q} \\ \dot{\theta} \end{pmatrix} = (A)\begin{pmatrix} u \\ w \\ q \\ \theta \end{pmatrix} + (B)\begin{pmatrix} \delta_e \\ \delta_t \end{pmatrix} \quad (2\text{-}14)$$

with

$$(A) = \begin{pmatrix} X_u & X_w & X_q & -g\cos\theta \\ Z_u & Z_w & Z_q & -g\sin\theta \\ M_u & M_w & M_q & 0 \\ 0 & 0 & 1 & 0 \end{pmatrix}$$

$$(B) = \begin{pmatrix} X_{\delta e} & X_{\delta t} \\ Z_{\delta e} & 0 \\ M_{\delta e} & 0 \\ 0 & 0 \end{pmatrix}$$

The lateral motion equation on the plane involves the rolling moment, the yawing moment and the side force of the equation of motion. The lateral motion equation in the state space state is given as follows (Akyazi *et al.*, 2013)

$$\begin{pmatrix} \dot{v} \\ \dot{p} \\ \dot{r} \\ \dot{\phi} \end{pmatrix} = (A_1)\begin{pmatrix} v \\ p \\ r \\ \phi \end{pmatrix} + (B_1)\begin{pmatrix} \delta_a \\ \delta_r \end{pmatrix} \quad (2\text{-}15)$$

with

$$(A_1) = \begin{pmatrix} Y_v & Y_p & Y_r & -g\cos\theta \\ L_v & L_p & L_r & 0 \\ N_v & N_p & N_r & 0 \\ 0 & 0 & 1 & 0 \end{pmatrix}$$

$$(B) = \begin{pmatrix} Y_{\delta a} & Y_{\delta r} \\ L_{\delta a} & L_{\delta r} \\ N_{\delta a} & N_{\delta r} \\ 0 & 0 \end{pmatrix}$$

3 Result and Discussion

Stability and control analysis is important to do to find out the flight performance of the aircraft when carrying out the mission. This analysis was carried out on the LSU 05-NG aircraft assuming when flying a cruise mission on a cruise with a speed of 30 m / s at an altitude of 1000ft. But before an analysis is carried out to obtain a dynamic system in the state of space, a simulation is

carried out to obtain aerodynamic stability derivatives. When conducting a simulation several variables to be considered as presented in

Table 3-1: .

Table 3-1: Variables that are considered during simulation

Variable	Value
Density	$1.222\ kg/m^3$
Viscosity	$1.463\text{e-}05\ m^2/s$
CG on X direction	$1.515\ m$
CG on Y direction	$0.000\ m$
CG on Z direction	$0.047\ m$
Inertia on X direction	$40.06\ kg\ m^2$
Inertia on Y direction	$63.58\ kg\ m^2$
Inertia on Z direction	$99.79\ kg\ m^2$
Inertia on XZ direction	$4.28\ kg\ m^2$
Mass of aircraft	$76.77\ kg$

The variables in Table 3-1 are entered into the XFLR5 software. In this XFLR5 software, the model of the aircraft was made first. The output of the aircraft model using XFLR5 is given at Figure 2-1: Model LSU 05-NG in XFLR5-1.
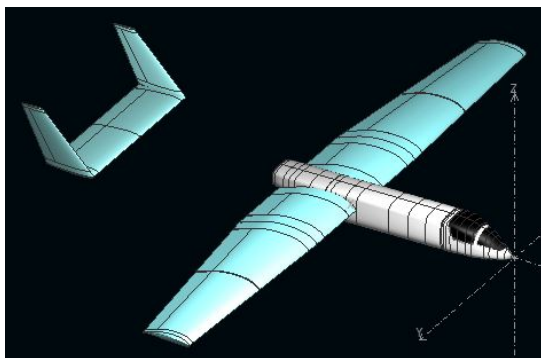
Figure 2-1: Model LSU 05-NG in XFLR5

The results of this simulation provide stability derivative values which will be used as the basis for calculating the elements in matrices A, B, and C. The derivative of aerodynamic stability in question includes the stability derivatives used for longitudinal and lateral motion. The assumption of this simulation is in a state of the cruise where there is no rotation in the control plane or the control plane on the plane.

Derivatives of aerodynamic stability for aircraft motion on the longitudinal dimension are given as follows:

Table 3-2: Stability derivatives of longitudinal axis

Stability derivatives of longitudinal	Values
C_{X_u}	-0.0012921
C_{X_a}	0.11819
C_{Z_u}	-0.00069528
C_{L_a}	5.3799
C_{L_q}	11.331
C_{m_u}	0.035372
C_{m_a}	-4.4388
C_{m_q}	-21.655

While the simulation results of aerodynamic stability derivatives for lateral motion are given in Table 3-3.

Table 3-3: Stability derivatives of lateral axis

Stability derivatives of lateral	Value
C_{Y_v}	-0.25652
C_{Y_p}	0.015134
C_{Y_r}	0.21229
C_{l_v}	-0.012482
C_{l_p}	-0.53234
C_{l_r}	0.062209
C_{n_v}	0.11286
C_{n_p}	-0.017257
C_{n_r}	-0.093463

3.1 Analysis of Stability and Control on the Longitudinal Matrices

Based on the data in Table 3-2, obtained a matrices A and B in the longitudinal motion as follows

$$A = \begin{pmatrix} -0.00271615 & 0.248462 & 0 & -9.81 \\ -0.257616 & -11.3097 & 68.9497 & 0 \\ 0.0576336 & -7.23232 & -11.3237 & 0 \\ 0 & 0 & 1 & 0 \end{pmatrix}$$

$$B = \begin{pmatrix} 1.959083 \\ -73.99448 \\ -188.4752 \\ 0 \end{pmatrix}$$

Then to find the stability of the dynamic system, eigenvalues and pole locations will be sought in the imaginary domain plane. By using the determinant formula the values of the roots of matrices A are obtained as follows

Table 3-4: Eigen values of matrices A on the longitudinal dimension

Symbol	Value
λ_1	-11.31719 - 22.33163i
λ_2	-11.31719 + 22.33163i
λ_3	-0.00089 - 0.19840i
λ_4	-0.00089 + 0.19840i

Because the eigenvalues of matrices A are negative or less than zero, based on Theorem 1 (George, 2015) that the dynamic system composed of decreasing the motion of the LSU 05-NG aircraft is stable. In addition to analyzing the stability can be seen in Figure 3-2. In Figure 3-2, it appears that all characteristic roots are located to the left of the imaginary axis. This means that the LSU 05-NG is dynamically stable on the longitudinal dimension. On the other hand, it is necessary to do a phugoid mode analysis. Phugoid mode is a mode where a deviation occurs so that sinusoidal motion occurs at low frequencies. This needs to be analyzed also to determine the stability of the aircraft when there is interference. The

phugoid mode analysis results are based on calculations using the following formula

$$\lambda_{phugoid} = -\frac{Z_u X_q - X_u Z_q}{2Z_q} \pm \sqrt{\left(\left(\frac{Z_u X_q - X_u Z_q}{2Z_q}\right)^2 + \frac{gZ_u}{Z_q}\right)} \quad (3\text{-}1)$$

Based on the data in Table 3-2 and Eq. (3-1) the following characteristics for phugoid mode are obtained.

Table 3-5: Value of phugoid mode output characteristics

Characteristic	Value
$\lambda_{phugoid}$	-0.001358 ±0.16323i
Undamped Natural Frequency	0.163236Hz
Damped Natural Frequency	0.16323Hz
Damping Ratio	0.008319
Time Periode	37.86068737

In addition to the phugoid mode, a short period analysis is also performed. Where this short period is the oscillation motion in a shorter time than the phugoid mode. The analysis results for the short period are given in Table 3-6.

It can be seen in Figure 3-3 and Figure 3-4 the simulation results for phugoid mode and short periods of motion equations on the longitudinal dimension. Based on Figure 3-3 and Figure 3-4 there are differences. For Figure 3-3, because the damping ratio is very small, it takes a long time to return to a stable state. Whereas in Figure 3-6, because the damping ratio is quite large, the time to stabilize is quite fast.

Table 3-6: Value of short periode mode output characteristics

Characteristic	Value
λ_{short}	-1.45372 ±8.73554i
Undamped Natural Frequency	8.855674 Hz
Damped Natural Frequency	8.73554 Hz
Damping Ratio	0.164157
Time period	0.707454834

Based on the analysis of the phugoid mode and short period, because the negative value is negative and based on the location of the pole as shown in Figure 3-2, the dynamic system composed of decreasing equations of motion at LSU 05 –NG is stable.

The next step is to analyze the controllability of the LSU 05-NG dynamic system using the Kalman rank condition. As the definition in the previous chapter, it will be proven that the linear system is said to be controlled if for any arbitrary condition $x(0)$ there is an unlimited number of $u(t)$ to transfer the state of $x(0)$ to any final state $x(t_1)$ in interval $t_0 \leq t \leq t_1$.

The solution of the system in Eq. (3-2) is as follows

$$x(t) = e^{At}x(0) + \int_0^t e^{A(t-\gamma)}Bu(\gamma)d\gamma \qquad (3-2)$$

where A and B are linearized matrices for longitudinal motion. Assuming the dynamic system in Eq. (2-2) is a controlled system, there is a controller $u(t)$ so that any $x(0)$ can be transferred to $x(t_1)$. By choosing $t = t_1$ Eq. (3-2) becomes

$$x(t_1) = e^{At_1}x(0) + \int_0^{t_1} e^{A(t_1-\gamma)}Bu(\gamma)d\gamma \qquad (3-3)$$

To guarantee the existence of the controller $u(t)$ wich transfers $x(0)$ to $x(t_1)$ within a finite time a non-singular matrix is defined

$$W(0,t_1) = \int_0^{t_1} e^{-A\gamma}BB^T e^{-A^T\gamma}d\gamma \qquad (3-4)$$

where B^T is the transpose of B matrices. Define the $u(t)$ is controller matrices as follows

$$u(t) = -B^T e^{-A^T t}W^{-1}(0,t_1) \qquad (3-5)$$
$$[x(0) - e^{-At_1}x_1]$$

where $W^{-1}(0,t_1)$ is invers matrices $W(0,t_1)$.

By substituting Eq. (3-5) into Eq. (3-3), $x(t_1) = x_1$ is obtained. Its means that there is a controller $u(t)$ so the dynamics system can be controlled. After that the rank condition of the matrices $[B \; AB \; \cdots \; A^{n-1}B]$ will be evaluated. Because the size matrice A is 4×4 then the value $n = 4$ the control matice for the dynamic system in Eq. (2-2) is given ac follows

$$[B \; AB \; A^2B \; A^3B] \qquad (3-6)$$

Based on matrices A and B generated in longitudinal motion, then Eq. (3-6) becomes

$$M_{AB} = 10^6 \begin{bmatrix} 0 & 0 & -0.0012 & 0.0537 \\ -0.0001 & -0.0122 & 0.3216 & 0.3423 \\ -0.0002 & 0.0027 & 0.0577 & -2.9793 \\ 0 & -0.0002 & 0.0027 & 0.0577 \end{bmatrix}$$

Because the determinant of matrices $M_{AB} \neq 0$, so matrices M_{AB} has *rank* equal to 4. Based on Theorem 2, the dynamic system that is composed of a linear equation of linear motion has controlled properties.

Figure 3-2: Pole position on the longitudinal dimension
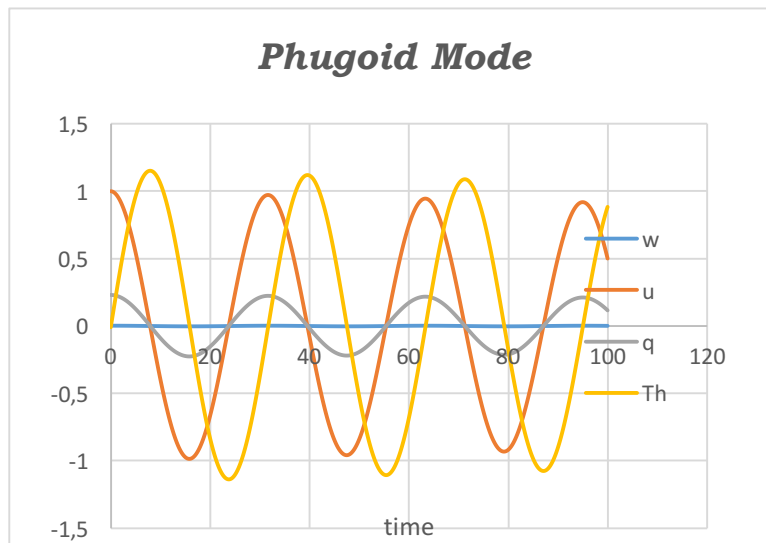
Figure 3-3: Longitudinal dimension simulation results in phugoid mode
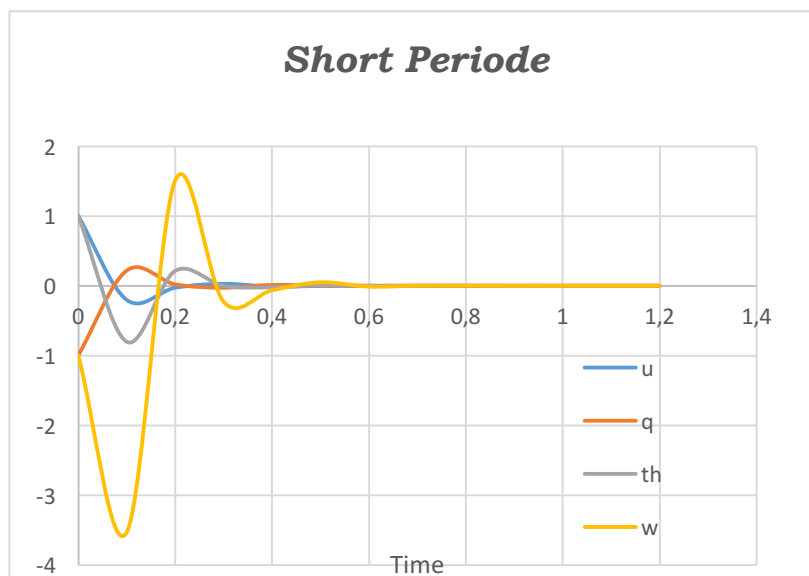
Figure 3-4: Longitudinal dimension simulation results in a short period

3.2 Analysis of Stability and Control in Lateral Dimension

Analysis of stability and controllability in the lateral dimension is done by calculating the values of the matrix elements A and B in the Eq. (2-15). Based on the data in Table 3-3: Derivative stability of lateral motion, the linear matrix A and B are obtained as follows

$$A = \begin{pmatrix} -0.539251 & 0.0874892 & -75.3672 & 9.81 \\ -0.0240078 & -32.2421 & 3.18616 & 0 \\ 1.01546 & -3.68163 & -1.99666 & 0 \\ 0 & 1 & 0 & 0 \end{pmatrix}$$

$$B = \begin{pmatrix} -20.83547 \\ -16.8183 \\ 37.95013 \\ 0 \end{pmatrix}$$

By using eigenvalue method of matrices A, obtained the characteristic values of matrice A are as follows

Tabel 3-4: Eigen value of matrices A in lateral dimension

Symbol	Value
λ_1	-31.88672+0.00000i
λ_2	-1.45186-8.76579i
λ_3	-1.45186+8.76579i
λ_4	0.01242+0.00000i

There are 3 modes if analyzed based on the root characteristics of matrix A, namely dutch roll, spiral, and roll subsidence. Three modes can be seen in Figure 3-5. Based on Table 3-7 and Figure 3-5 the spiral mode is positive and the pole is located to the right of the imaginary axis. This indicates that in spiral mode the plane's motion is unstable. However, for dutch roll and roll subsidence, it is stable. If the longitudinal motion is analyzed for two modes, namely the short period and phugoid mode, then the lateral movement also analyzes the dutch roll mode. Dutch roll is motion instability caused by disturbance resulting in a combination of yawing and rolling motion. Simulation results for lateral motion in dutch roll mode are given in Figure 3-6.

Based on Figure 3-6, the yaw rate (r) has a peak value of 5.322272 at 0.15 seconds and returns to the settling time at 7.43 seconds. Roll rate (p) has a peak value at 0.2 seconds of 0.495407 degrees / s and returns stable at 6 seconds of the graph to zero. The angle of roll on the graph starts from -0.06867 in the initial seconds and has a peak value of 0.042045 degrees at the second to 0.39 and continues to oscillate until stable again at 4.49 seconds.
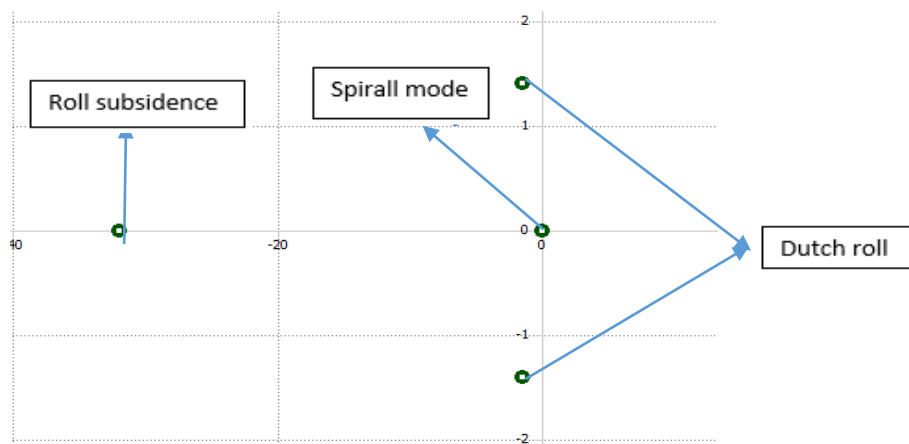
Figure 3-5: Graph of a mode of lateral motion
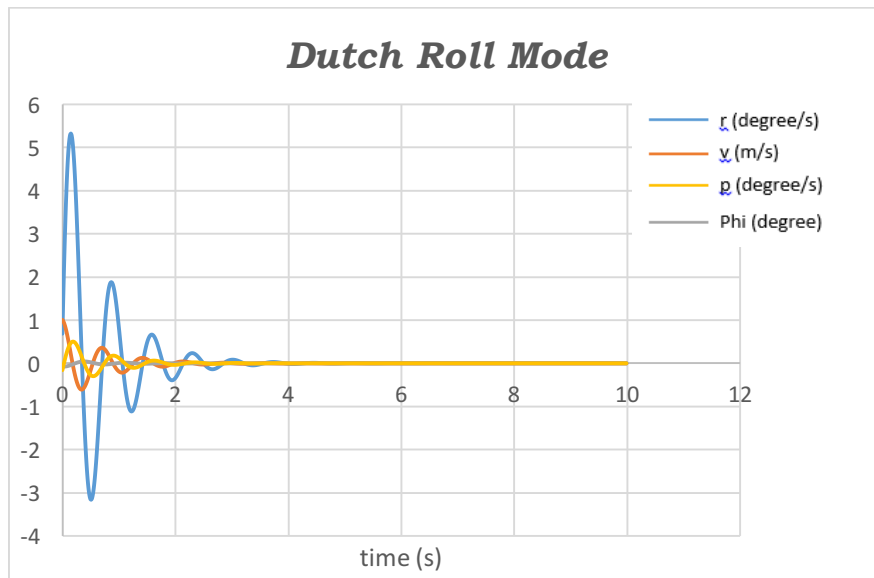
Figure 3-6: Simulation results of lateral motion mode dutch roll

Next, the controllability of the dynamic system on the lateraldimension will be analyzed. The steps for analysis of controllability in the lateral dimension are the same as the analysis of controllability in the longitudinal dimension. The first thing to do is to prove the existence of the controller $u(t)$ so that any $x(0)$ can be transferred into $x(t_1)$. Therefore defined $u(t)$ as a controller as in Eq. (3-5). Based on the analysis done previously on the longitudinal dimension, the controller $u(t)$ can be guaranteed so that any $x(0)$ can be transferred to $x(t_1)$. When it can be guaranteed that there is a controller $u(t)$ will be analyzed matrice $N_{AB} = [B\ AB\ A^2B\ A^3B]$.

With the input matrices A and B on the lateral dimension obtained

$$N_{AB} = 10^5 \begin{bmatrix} -0.0002 & -0.0285 & 0.0407 & 3.9947 \\ -0.0002 & 0.0066 & -0.2144 & 6.7443 \\ 0.0004 & -0.0004 & -0.0527 & 0.9359 \\ 0 & -0.0002 & 0.0066 & -0.2144 \end{bmatrix}$$

Determinant of matrices N_{AB} not equal to zero, it's meaning that matrices N_{AB} has inverse and rank. Based on an identification of the rank of matrices N_{AB} the number of rank of matrices N_{AB} is 4. Where the rank of matrices N_{AB} is equal

to $n = 4$. Because the rank of matrices N_{AB} is equal to n, then matrice N_{AB} can be controlled in other words, dynamic systems of the lateral dimension are controlled. Simulations performed both on the longitudinal and lateral dimensions, are simulated by calculating the load carried by the LSU 05-NG when carrying out the mission. Based on simulations using XFLR5, when carrying out missions carrying 30 kg loads, the LSU 05-NG remains stable

4 Conclusion

Analysis of the stability and control of the dynamic system in longitudinal and lateral motion shows that the dynamic system in the longitudinal dimension is stable and can be controlled by using eigenvalue method and Kalman Rank Condition Method. This is because matrix A has a negative characteristic value and the location of the pole in the s-plane is to the left of the imaginary axis. On the other hand, because the control matrix M_{AB} has the same rank as n, the dynamic system in longitudinal motion can be controlled or controlled. Whereas in the lateral dimension, three eigenvalues or

negative characteristics are stable in the subsidence roll and dutch roll. However, in spiral mode, it is not stable due to positive eigenvalue. The N_{AB} control matrix has the same rank as n, so it can be concluded that the dynamic system in the lateral dimension is controlled.

Acknowledgment

Contributorship Statements

AS developed the simulation; designed method, analyzed the results, and prepared the manuscript.

References

Adiprawita, W., Ahmad, A.S. & Semibiring, J. 2008. Hardware In The Loop Simulator in UAV Rapid Development Life Cycle. *Engineering*, (November 2013): 6.

Ahmed, A.E., Hafez, A., Ouda, A.N., Ahmed, H.E.H. & Abd-Elkader, H.M. 2015. Modeling of a small unmanned aerial vehicle. *Adv Robot Autom*, 4(126): 2.

Akyazi, O., Ali Usta, M. & Sefa Akpinar, A. 2013. A Self-Tuning Fuzzy Logic Controller for Aircraft Roll Control System. *International Journal of Control Science and Engineering*, 2(6): 181–188.

Boschetti, P.J. & Cárdenas, E.M. 2012. Ground effect on the longitudinal stability of an unmanned airplane. *50th AIAA Aerospace Sciences Meeting Including the New Horizons Forum and Aerospace Exposition*, (January 2012).

Boschetti, P.J., Cárdenas, E.M. & Amerio, A. 2010. Stability of an unmanned airplane using a low-order panel method. *AIAA Atmospheric Flight Mechanics Conference 2010*, (May).

Cardenas, E.M., Boschetti, P.J. & Amerio, A. 2004. Stability and Flying

Qualities of an Unmanned Airplane Using the VortexLattice Method. 11856(April).

Davis, J.M., Gravagne, I.A., Jackson, B.J. & Marks, R.J. 2009. Controllability, observability, realizability, and stability of dynamic linear systems. *Electronic Journal of Differential Equations*, 2009(January 2009): 1–32.

George, R.K. 2015. Controllability , Observability , Stability and Stabilizability of Linear Systems. hal.1–27.

Luckner, R. 2007. Inhaltsverzeichnis. *Flugmechanik I Grundlagen und stationäre Flugzustände*, 300.

Nelson, R.C. 1989. *Flight Stability and Automatic Control*. Second ed. USA: McGraw-Hill, Inc.

Parmar, J. & Acharya, V. 2015. Selection and Analysis of the Landing Gear for Unmanned Aerial Vehicle for Sae Aero Design Series. *International Journal of Mechanical Engineering and Technology*, 6(2): 976–6340.

Purwanto, E.B. 2012. Pemodelan Sistem dan Analisis Kestabilan Dinamik Pesawat UAV. *Jurnal Teknologi Dirgantara*, 1: 1–12.

Rizaldi, A. 2019. *DESIGN REQUIREMENTS & OBJECTIVES OF LSU-05 NG*. Bogor: Pusat Teknologi Penerbangan.

Subiono 2013. *Sistem Linear dan Kontrol Optimal. 1*. Surabaya: Jurusan Matematika Institut Teknologi Sepuluh Nopember.

Sugandi, T.S., Nathan, Subrata, S.K., Arifianto, O. & Moelyadi, M.A. 2018. Prediction of static stability in tandem wing unmanned aerial vehicle. *Journal of Physics: Conference Series*, 1130(1).

Tian, L., Guan, Y. & Wang, L. 2019. Controllability and observability of multi-agent systems with general linear dynamics under switching

topologies. *International Journal of Control*, 0(0): 1–13. Tersedia di https://doi.org/00207179.2019.16 49465.

Ulus, S. & Ikbal, E. 2019. Lateral and Longitudinal Dynamics Control of a Fixed Wing UAV by using PID Controller. (January).

Yechout, T.R. 2003. *Introduction to Aircraft Flight Mechanics: Performance, Static Stability, Dynamic Stability, and Classical Feedback Control.* Virginia: American Institute of Aeronautics and Astronautics, Inc.

Younus, A. & Ur Rahman, G. 2014. Controllability, observability, and stability of a volterra integro-dynamic system on time scales. *Journal of Dynamical and Control Systems*, 20(3): 383–4402.

NUMERICAL INVESTIGATION ON THE FUSELAGE AIRFRAME OF LSU 05 NG

M. Hafid, Abian Nurrohmad[1], Redha Akbar Ramadhan
Aeronautics Technology Center, Indonesian National Institute of Aeronautics and Space (LAPAN)
[1]e-mail: m.hafid@lapan.go.id

ABSTRACT

In this paper, a numerical investigation on the fuselage structure of LSU 05 NG was carried out. This fuselage is designed to carry the payload up to 25 kg. Statical numerical analysis using the finite element method has been done by using Simulia Abaqus. The fuselage structure that has been designed which consists of frame, longeron, and skin that can also be called a semi-monocoque structure. This airframe uses combination of balsa and GFRP type of composite as the material. There are three load cases,i.e. take-off condition, cruise condition, and landing condition. Tsai-hill failure criteria is used to investigate the strength of the composite structure due to the load that is applied. The maximum stress from this calculation is 49.24 MPa on the ground condition (take-off and landing) while the maximum principle stress on the cruise condition is 52.76 MPa. The maximum Tsai-hill criterion is 0.95 at the cruise condition. With such simulation results, it can be said that the fuselage structure is still safe when operated and can also be optimized for several components so that the weight of the aircraft can be reduced.

1 Introduction

LSU 05 NG is an unmanned aircraft developed by Pustekbang LAPAN. It is the new generation of LSU 05 with a wider fuselage to carry more payloads. The fuselage is reinforced with frame and longeron along in its skin structure which is called the semi-monocoque structure.

The aircraft developed from LSU 05 UAV (Unmanned Aircraft Vehicle) is a part of the Maritime Surveillance System Project. It has improved payload performance by optimizing the airfoil and the geometry of the internal structure. LSU 05 NG is designed to carry various missions. The main mission for LSU 05 NG is maritime surveillance with additional missions such as air logistics, search mission, and aerial photography. Every mission has its loading profile.

There are so many previous research about design and numerical simulation which has been done to build some unmanned aircraft. Chen and Lu have done the numerical simulation method of UAV fuselage compression under centrifugal load based on the discrete element analysis method. The purpose of this method is to calculate the centrifugal load stress spectrum of the surface of the UAV fuselage. By doing this method, the accuracy of the anti-compression numerical test of the UAV becomes higher (Chen & Lu). Ariyanto, et al has designed a low-cost fixed-wing unmanned aerial vehicle that can fly

autonomously. This research is using the weighting factor to determine the best configuration of each design parameter (Ariyanto et al).

Chung et al also presents their report about design, manufacturing, and flight testing an experimental flying wing UAV. The design of the airframe is based on matching plot, weight estimation approach, and conventional aircraft design procedure (Chung et al). Velasco et al implementing UAV Design using five requirements such as maximum span, budget ceiling, payload and mission, weight, and cruise speed. The design meets the measurable design requirements even though it is using adjustments since the requirements is less specific and therefore is hard to assess (Velasco et al). Design and analysis of UAV fuselage is performed by using finite element analysis (Sighanart et al) which shows the maximum stress while load is applied (Dassault Systemes).

Raja et al has described the rivetted splice joint at the fuselage structure. Their calculation is performed by using cabin pressurization in aircraft fuselage. They use the global finite element using static analysis to get the benchmark results from the splice joint panel. This structure is a safe limit at this load case (Raja et al). Hadjez and Necib use the Patran-Nastran software to study the stress analysis on the aircraft fuselage with and without porthole. This work is to study the stress concentration in the aircraft fuselage due to the presence of porthole (Hadjez & Necib).

Material selection has a crucial role in the analysis of UAV Fuselage. To achieve the strength and lightweight structure, the composite material has been proven as an excellent material for lightweight structures (Abdurohman & Marta). The composite is ductile enough

so that it can be used as a UAV fuselage material (Isna et al).
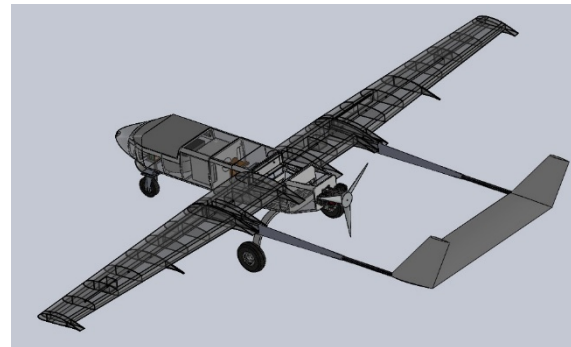
Figure 1-1: Detail Design of LSU-05 NG

In this research, there are three loading configurations on LSU-05NG's fuselage. The loading is simulated as static load as the result of combination of various loading such as wing and empennage loading. The loading configurations consists of take-off condition, cruise condition, and landing condition. The prediction of structure strength will be conducted by numerical simulation. Numerical simulation will be done with commercial finite element software Abaqus. The result of simulation will be evaluated by the Von Mises and Tsai-Hill failure criteria hence the strength of structure can be determined.

2   Methodology

The method used in this research is to start by design the fuselage of UAV using CAD (Computer Aided Design) software. In this case, the software used is Solidwork 2017. After the design is complete, the next step is exporting the drawing model in to the finite element software and set up the finite element model. The finite element model consists of main component that divided into small partitions that called finite elements. The boundary conditions and material databases need to be inputted into the model, so the simulation could

yield results to be analyzed. The workflow of this research is shown in Figure 2-1.
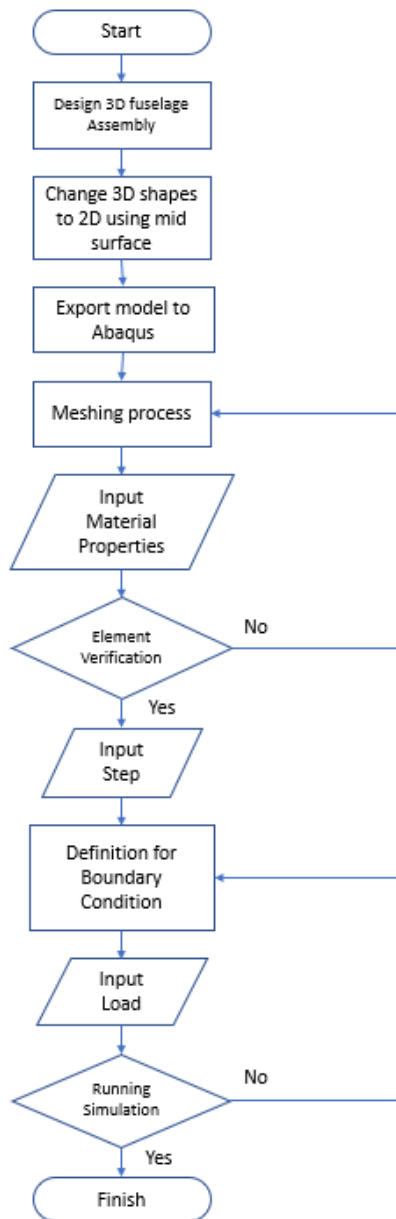
Figure 2-1: Workflow of Research

The detail design of the UAV fuselage airframe has been done by using Solidwork 2017. The detail drawing can be seen on Figure 2-2. Commonly the fuselage of aircraft consists of frame, skin, longeron, and bulkhead. The frame is dedicated to give the shape of the fuselage. The longeron together with the frame carry the

bending load and torsion in the fuselage due to its own weight and the weight of payload inside. The bulkhead is the reinforced frame that dedicates to carry heavier payload. Usually the bulkhead is placed in the joint between wing and fuselage and fuselage with landing gear. The skin structure is effective to carry tension load and is dedicated to be the shield of system in the fuselage during the mission of this aircraft.
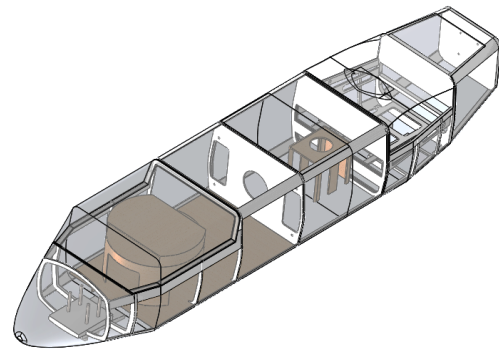
Figure 2-2: Fuselage 3D Detail Drawing

After the 3D model is complete, the next step is to build the finite element model. In this case, the structure can be modelled as shell element, to simplify the simulation process while maintaining the consistency of the model. The simplification has been done with CAD software Solidwork 2017 by simplifying solid parts into surface. The surface model is dedicated to build the finite element model using shell element instead of solid element. The benefit of shell element in this case is the running time is faster and the results is still pretty accurate.
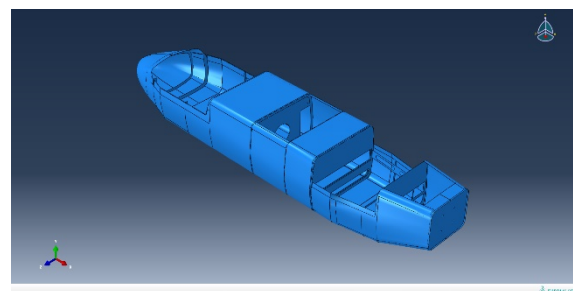
Figure 2-3: Fuselage Surface Model

The skin structure is simplified from a 3D model into a surface model by generating from its middle surface. The skin of this fuselage using composite as material properties. In this skin there are three openings which function for the entry and exit of the payloads and fuel tank and attachments with wing. The detail surface model of the fuselage skin can be seen in Figure 2-4 below.
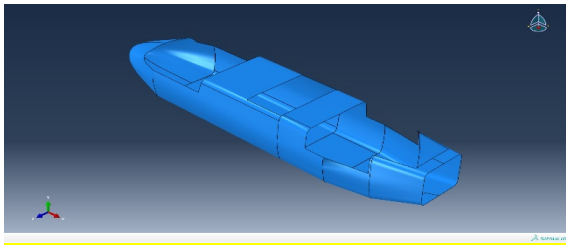
Figure 2-4: Fuselage Skin Model

The frame bulkhead and the longeron is also converted into the surface model. The frame bulkhead and the longeron also use composite for material properties. The detail surface model of the bulkhead, frame and longeron can be seen in Figure 2-5.
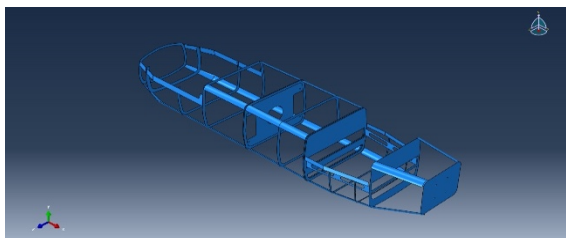
Figure 2-5: Fuselage Frame and Longeron Model

One of the important process on structural stress analysis is meshing process. This process dividing a part into several element. The element acts as finite element where the reaction and stress acts at each corner of the elements. The quality of the mesh will determine the simulation. Finer mesh will yield more accurate results than coarse mesh but with increased computation time. The element that is

used in this model is quad shell element type. This element have a square shape. The quad element is used with plane stress assumption. This assumption can be used accurately for thin relative structure. The benefit of using quad shell element instead of solid element is faster in the computational time. The shell element assumption can not used if the concern is in the trough thickness structure. The finite elemet model with quad dominated shell element can be seen in Figure 2-6.
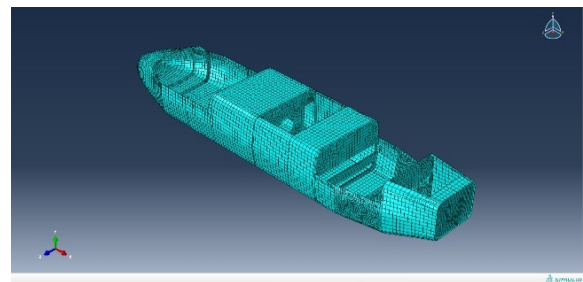
Figure 26: Meshed Geometry

The skin structure of fuselage is using composite material. A composite material is often used because it has several advantages including being lighter and possessing high strength. Designed material for LSU 05 NG's fuselage structure is using E-Glass EW185/Epoxy composite, with 4 ply. The properties of the composite is shown below in table 2-1. The main reason to use E-glass in fuselage structure is about its good interaction with avionic component. It is because the main avionic device like control unit, battery, antenna are located in the fuselage.

The values from table 2-1 are obtained from tensile testing of composite materials using 4 layers of E-Glass fiber ±45° which has a density of 2.2 g/ cm^3 the results of the test are greatly affected by material, method, specimen conditions, preparation, and also the percentage of reinforcing material. (Abdul-Hamead et al).

Table 2-1: Material Properties

Properties	Value
E1	8090 MPa
E2	8090 MPa
υ_{12}	0.1
G12	1270 MPa
G13	1270 MPa
G23	1270 MPa
$\sigma_{max\_tension\_1}$	261 MPa
$\sigma_{max\_tension\_2}$	261 MPa
$\sigma_{max\_comp\_1}$	63.66 MPa
$\sigma_{max\_comp\_2}$	63.66 MPa
σ_{max12}	17.3 MPa

To assess the damage in the composite structures, Tsai-Hill failure criterion will be used. Tsai-Hill criterion predicts the failure of anisotropic materials by comparing the value of working stresses with maximum stresses of the material. The equation used in Tsai-Hill criterion is shown below,

$$\left(\frac{\sigma_{11}}{X_{11}}\right)^2 - \left(\frac{\sigma_{11}\sigma_{22}}{X_{11}^2}\right) + \left(\frac{\sigma_{22}}{X_{22}}\right)^2 + \left(\frac{\sigma_{12}}{X_{12}}\right)^2 \leq 1 \qquad (2\text{-}1)$$

In equation above, σ and τ refers to working stresses on material. X refers to maximum stresses of material. Subscripts in front of X indicates the direction of maximum stress. The material will fail when the result of equation exceeds 1.

Table 2-2: Concentrated Loads

Loads	Value
Engine Weight	44.64 N
Payload Weight	119.76 N
Wing Weight	174 N
Empennage Weight	81.96 N
Fuel Tank (Full Tank)	164.42
Engine Thrust	360 N
Fuselage & Landing Gear Weight	133.22 N

In this research, there are six loads in form of concentrated loads. This load is subjected to represents the real load that happens in the fuselage structure when the fuselage at the ground condition or the flight condition. The loads and their values are shown below in table 2-2.

In the process of analyzing the load that applied in fuselage, the load is considered as a concentrated force. Concentrated force is the load that will be located specifically at a particular location since weight/force and location of the load is known. Many of load are simplified to six loads that have been tabulated by table 2-2. Boundary conditions are defined as fixes on landing gear attachments, center fuselage connections with nose, and wing attachment. The fuselage boundary conditions are given in table 2-3.

Table 2-3: Fuselage's Boundary Condition

BC#	BC 1	BC 2	BC 3
U1	0	0	0
U2	0	0	0
U3	0	0	0
UR1	0	0	1
UR2	0	0	0
UR3	0	0	0

The load and boundary condition application is given by Figure 2-7.
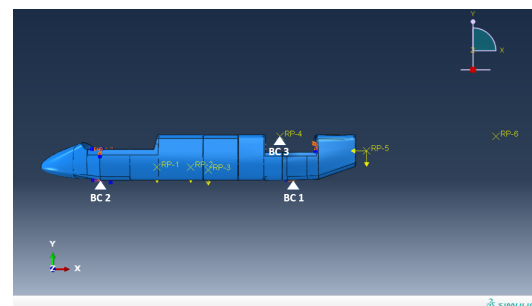
Figure 2-7: Definition for boundary condition and loads

The static load on LSU 05 NG will be simulated with three load case. These three load case represents critical loading scenario on fuselage. Take-off and landing condition is part of ground load. This condition is critical for fuselage structure because the ground reaction at the landing gear station. While the flight condition is critical in the joint between fuselage and wing structure. The configurations is shown in table 2-4.

Table 2-4: Fuselage Static Loading Configuration

Loading Configura-tion	Scenario	Loadings	Boundary Conditions
#1	Take-Off Condition	Engine, Payload, Wing, Fuel Tank, Empennage, and Engine Thrust	BC 1, BC 2
#2	Cruise Condition (Load Factor 2G)	Engine, Payload, Fuel tank, Fuselage and Landing gear, and Engine Thrust	BC 3
#3	Landing Condition	Engine, Payload, Wing, Fuselage and Landing Gear, Empennage, Engine Thrust (50%), and fuel tank	BC 1, BC 2

(50%)

In Abaqus, when 2D components are imported from solidwork it consists of parts that have not been connected to another. So that constraint process is needed to enable modeling kinematic relationship between components chosen is tie constraint because it can be used to make translational and rotational motion and all other degrees of freedom equal for a pair of surfaces. In working with a tie constraints, one surface or region node in the constrint is defined as the master and the other surface or region node is determined as a slave. Nodes are tied only where the surfaces are close to one another. The process of selecting surfaces as master and slave can deterine the result of numerical computation. Each node can only be used as a slave once and if more than one then simulation will run an error.
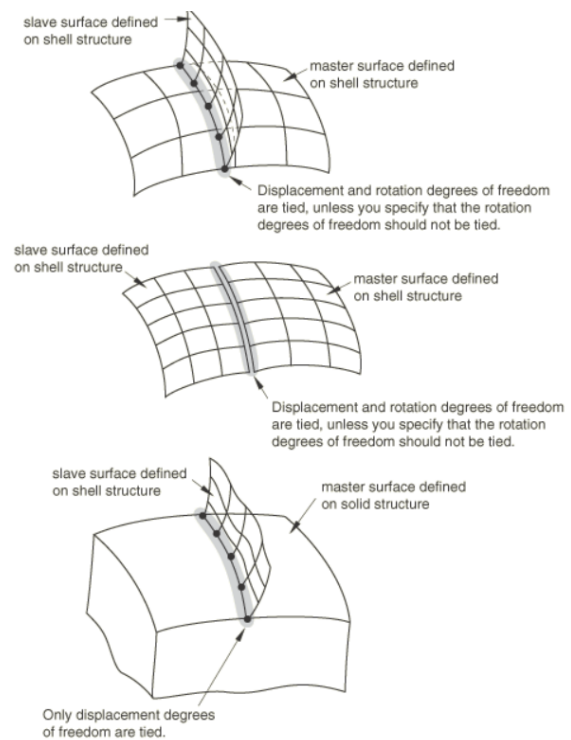
Figure 2-8: Surface-based Tie Algorithm (https://abaqus-docs.mit.edu)

Tie constrain is suitable while two components are surfaces. Displacements and rotation degrees of freedom are tied, unless the designer specify that the rotation degrees of freedom should not be tied. But if master surface defined on solid structure, only displacement degrees of freedom are tied. For interaction between load and fuselage, constraint coupling is used because it is possible to limit some of the nodes in the fuselage to the reference node. The reference node here is the point where load is applied.
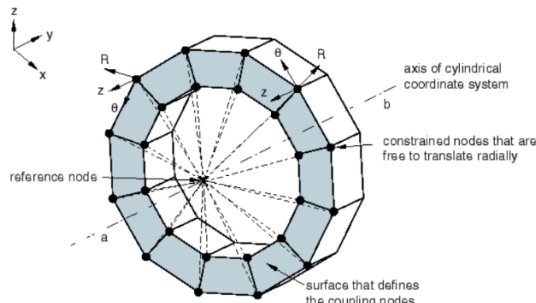
Figure 2-9: Kinematic Coupling Constraint (https: // abaqus-docs.mit.edu)

The coupling constraint is useful when coupling nodes on fuselage structure is constrained to the rigid body motion of single node. This coupling constraint effectively used in application of load or boundary conditions to a model.

3   Result and Analysis

To design composite fuselage, a stress analysis is performed finite element using Abaqus Software. Abaqus simulation allows to analyze the strength of composite material that used to fuselage structure. Property manager allows to set required number of layers, thickness, orientations and layer materials. This tool shows laminate coordinate system and direction of each individual layers. In considered case

numbers of layers was set to 4. Thickness of composite layers amounted 0.125 mm on skin so that total thickness of skin is 0.5 mm. the frame bulkhead is made thicker with 1.25 mm so that total thickness of frame bulkhead is 5 mm. The results of stress analysis on the LSU 05 NG fuselage can be seen from Figure 3-1 to Figure 3-6. The stress analysis is presents in maximum principle stress to evaluate which stress is maximum in each direction. The Tsai-Hill failure criterion was used to check whether the structure is fail or not in all direction. The structure can be claimed to be safe and has no failure is the value of Tsai-Hill criteria is below 1. The stress value is presented to give some illustration about the stress distribution in the fuselage. From the stress distribution can be seen the location of maximum or critical condition that occured in the fuselage structure.
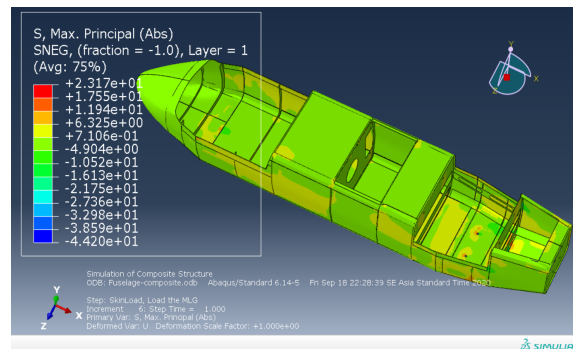
Figure 3-1: Max. Principal Stress for Configuration 1
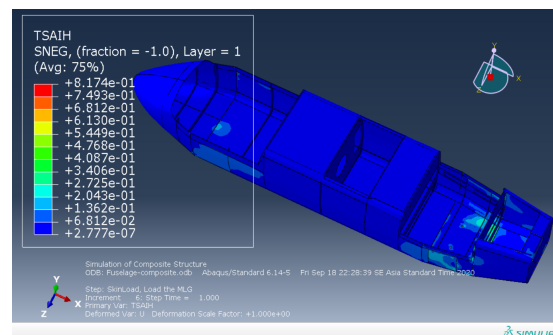
Figure 3-2: Tsai-Hill Criterion Result for Configuration 1

Figure 3-1 shows the stress distribution on the fuselage at take-off condition. The stress distribution that presented is maximum principle stress. The maximum tension stress is 23.17 MPa while the maximum compression stress is 44.2 MPa. The Tsai-Hill value can be seen on Figure 3-2. The maximum Tsai-Hill value is 0.81 at the main landing gear bulkhead.
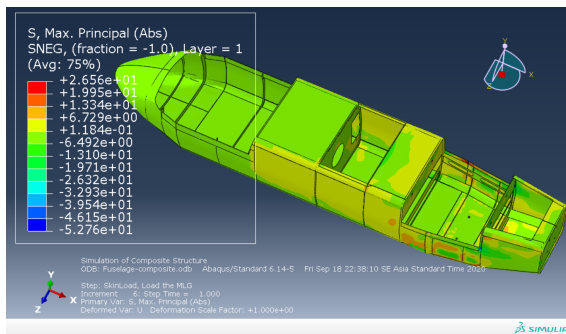
Figure 3-3: Max. Principal Stress for Configuration 2
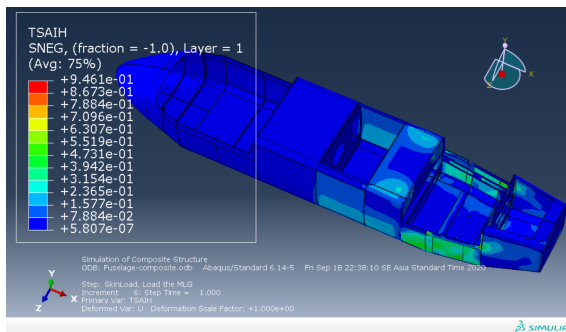
Figure 3-4: Tsai-Hill Criterion Result for Configuration 2

Figure 3-3 shows the stress distribution on the fuselage at cruise condition. The load that applied at this condition is assume by 2G load factor due to its maneuver. The stress distribution that presented is maximum principle stress. The maximum tension stress is 26.5 MPa while the maximum compression stress is 52.76 MPa in the negative sign. To investigate its failure the Tsai-Hill failure criterion is used. Figure 3-4 shows the Tsai-Hill distribution along the fuselage. The maximum Tsai-Hill value is 0.946 at the

100

wing joint, so it is the critical point that failure might happen.
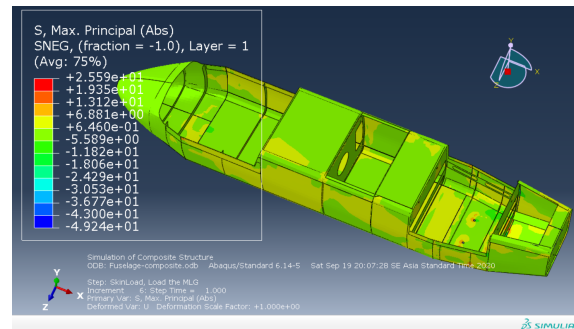
Figure 3-5: Max. Principal Stress for Configuration 3

Figure 3-5 shows the stress distribution on the fuselage at landing condition. The stress distribution that presented is maximum principle stress. The maximum tension stress is 25.59 MPa while the maximum compression stress is 49.24 MPa. The Tsai-Hill value can be seen on Figure 3-6. The maximum Tsai-Hill value is 0.92 at the main landing gear bulkhead. It can be concluded that landing condition is more critical in terms of structure rather than take-off condition. The skin structure near the landing gear bulkhead might fail due to the stress flow from the landing gear impact.
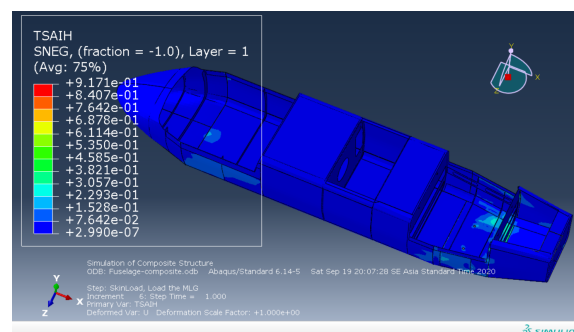
Figure 3-6: Tsai-Hill Criterion Result for Configuration 2

The maximum values of stress from all scenario are tabulated into table 3.1. the overall results is dominated with blue color that indicated the minimum stress is occured in the majority of the

structure. It is one point that can be the reason to do the optimization to minimize the weight of the fuselage in the next research. The maximum stress occured in the main landing gear attachment or on the boundary condition since this area is critical.

Table 3-1: Maximum Values for Von Mises Stress and Tsai-Hill Criterion

Loading Configurat-ion #	Max. Princi-pal Stress (Tens-ion) [MPa]	Max. Princi-pal Stress (Compr-ession) [MPa]	Maximum Tsai Hill Criterion
#1	23.17	44.20	0.82
#2	26.56	52.76	0.95
#3	25.59	49.24	0.92

The maximum principal stress on fuselage is 52.76 MPa (compression), which occurs at cruising configuration. The value of Tsai-Hill Criterion is 0.95, less than 1. The working stress value is lower than maximum stresses of the material. It can be concluded that fuselage of LSU-05 NG is capable to endure loading at its operations. The result of numerical analysis can be used as a reference for next iteration design so that the fuselage structure is obtained that satisfies the requirements specified in the LSU 05 NG Project, such as weight reduction.

Development of fuselage for unmanned aerial vehicle is a multistage task with includes: geometrical calculations, structural design, materials selection, numerical analysis, and elaboration of technology. Numerical investigation plays an important role because it can predict the structural strength of a fuselage when the load

applied. it still needs validation with an experimental investigation so the design results of the LSU 05 NG's fuselage are completely able to do flight tests.

4 Conclusions

From the results of simulation and analysis, it can be concluded that,

a. E-Glass WR185/Epoxy 4 ply composite can be used as material for fuselage structures to endure loadings in critical conditions.

b. Maximum principal stress occurred at loading configuration #2, with value 52.76 MPa (compression).

c. Maximum Tsai-Hill criterion is 0.95. The value is less than 1, so the structure is considered safe at the loading configuration.

d. The fuselage can be optimized to minimizing concentrated stress at boundary condition

e. Several frame bulkheads can be optimized to reduce the weight of the LSU-05 NG's aircraft.

Reinforcement at any critical area is needed to make sure the airframe is not fail while in its operation. The thickness can be increase by add-up some plies at the skin or bulkhead. It's will be better by design sandwhich structure or combine the laminate using balsa to increase its moment inertia so the maximum stress can be reduced.

This Paper has presented a composite structure used in LSU 05 NG's fuselage and configure the load applied on fuselage. It has been found that Abaqus/Explicit is able to predict failure by tsai-hill criterion and von mises stress. Further, experimental investigation is needed to gain confidence about the strength of fuselage structure.

Contributorship Statements

MH and AN conceived of the presented idea. MH, AN, and RA compiled post-processing method. MH performed numerical simulations, data analysis, and interpretation. AN and RA contributed to the final version of the manuscript.

References

ABAQUS/Explicit: Advanced Topics, (2005). *Lecture 7: Constraints and Connections*, https://www.researchgate.net/profile/Mehdi_Ebadi_Jamkhaneh/post/How_we_apply_tie_material_between_two_layers_of_different_material_components_in_abacus_software/attachment/5a408fae4cde266d587d8007/AS%3A575328980566016%401514180526271/download/l7-connections.pdf

Abdul-Hamead. A.A, Kasim. T, Mohammed. A. A, (2014). *Mechanical Properties for Polyester resin Reinforce with Fe Weave Wire*. International Journal of Application or Innovation in Engineering & Management (IJAIEM) ISSN: 2319-4847 Vol. 3, Issue 7

Abdurohman. K, Marta. A, (2016). *An Experimental Study of Polyester Composite Tensile Properties Reinforced Undirectional Carbon Fiber Manufactured by Vacuum Infusion for LSU Materials*. Jurnal Teknologi Dirgantara Vol. 14 No. 1 Juni 2019 :61-72

Ariyanto. M, Setiawan J. D, Prabowo. T, Haryanto. I, Munadi, (2018). *Design of a Low-Cost Fixed Wing UAV*. IJCAET & ISAMPE 2017. MATEC Web of Conferences 159, 02045 (2018)

Chen. Y, Lu. X, (2018). *Numerical simulation of unmanned aerial vehicle under centrifugal load and optimization of milling ang planning*. AIP Conference Proceedings 1967, 040062 (2018)

Chung. P. H, Ma. D. M, Shiau. J. K, 2019. *Design, Manufacturing, and Flight Testing of an Experimental Flying Wing UAV*. Applied Sciences

Dassault Systemes, (2010). *Introduction to Abaqus*. Abaqus User Documentations.

Grodzki. W, Lukaszewicz. A, (2015). *Design and Manufacture of Unmanned Aerial Vehicles (UAV) Wing Structure using composite materials*. Mat.-wiss. U. Werkstofftch, 46, No. 3

Hadjez. F. And Necib. B, (20150. *Stress Analysis of an Aircraft Fuselage with and without Portholes using CAD/CAE Process*. Journal of Aeronautics & Aerospace Engineering Volume. 4 Issue 1

Hibbeler. R, (2011). *Mechanics of Materials*. Pearson Prentice Hall.

Isna. L. R, Abdurohman. K, Ula. N. M, Wijaya. Y. G, (2019). *Tensile properties E-Glass ±45° Fiber with Matriks Polyesther Composite as Structure of LSU*. Iptek Penerbangan dan Antariksa: Progres Litbangyasa Roket, Satelit dan Penerbangan 2018

Raja. D. B. P, et.al, (2018). *Stress analysis of Al2014-T6 riveted splice joint fuselage structure using finite element analysis*. IOP Conf. Series: Materials Science and Engineering 455 (2018) 012138

Singhanart. T, Srimontok. C, Pisitpan. N, Chitimaworaphan. S, Mongkhonchaiwiwat. W, (2012). *Design and Analysis of UAV Fuselage*. Applied Mechanics and Materials ISSN: 1662-7482 Vol. 225, pp 305-309

Velasco. M. F, Stampfli. E, Fardoun. H, Balboa. M. D*, (2016). *Mechanical Design Project: Conceptual and Preliminary Design of an Unmanned Aerial Vehicle*. Universidad Europea de Madrid.

A FINITE ELEMENT ANALYSIS OF CRITICAL BUCKLING LOAD OF COMPOSITE PLATE AFTER LOW VELOCITY IMPACT

Redha Akbar Ramadhan[1], M. Giri Suada[2], Hendri Syamsudin[2]

[1]Aeronautics Technology Center, Institute of Aeronautics and Space of Indonesia

[2]Faculty of Mechanical and Aerospace Engineering, Bandung Institute of Technology

[1]e-mail: redha.akbar@lapan.go.id

ABSTRACT

Composite is a material formed from two or more materials that macroscopically alloy into one material. Nowadays, composite has been generally applied as lightweight structure of aircraft. This is due to the fact that composites have high strength-to-weight ratio. It means the composites have the capability to take on various loads, despite their lightweight property. Laminate composite is one type of composites that has been generally used in aircraft industries. This type of composite is susceptible to low-velocity impact induced damage. This type of damage can happen in manufacture, operation, or even in maintenance. Low-velocity impact could cause delamination. Delamination happens when the plies of laminated composites separate at the interface of the plies. This type of damage is categorized as barely visible damage, means that the damage could not be detected with visual inspection. Special method and tool would be needed to detect the damage. Delamination will decrease the strength of the laminated composite. Delamination can be predicted with numerical simulation analysis. With increasing capability of computer, it is possible to predict the delamination and buckling of laminated composite plate. This research presents the comparisons of buckling analysis results on laminated plate composite and damaged laminated plate composite. By the result of LVI simulation, it is shown that low velocity impact of 19.3 Joule causing 6398 mm^2 C-Scan delamination area inside the laminated composite. The delamination causes structural instability that will affect buckling resistance of the plate. The result of analysis shows that the existence of delamination inside laminate composite will lower its critical buckling load up to 90% of undamaged laminate's critical buckling load.

Keywords: *composite, laminate, delamination, buckling.*

1 Introduction

Composite has been widely used as material of lightweight structures in aerospace industries. Composite refers to the materials that consist of two or more different materials that alloy macroscopically. By macroscopically, it means the properties of each materials can still be seen and is distinguishable from one another. Generally, composite consists of fiber and matrix. Fiber acts as the reinforcement and the main strength provider of composites. Matrix acts as protection of the fibers and substance that glues the fibers in composite. Composite has been used as a substitute of metals in several parts in aircraft. It is due to composite's high strength to weight ratio which means the composite has strength that almost equal to metal's strength, with far lighter weight than metal's.

Like all lightweight structures, laminated composite structures are susceptible to buckling failure. Buckling is a form of structural instability that causes change on geometry of the structure. Buckling is usually caused by compression load but not limited to compression load only. In some cases, tension load and shear load can induce buckling phenomenon too.

Buckling can be affected by existence of imperfection in composite. One of the imperfection in composite is delamination which is caused by low velocity impact (LVI). LVI is defined as impact with speed of impactor at 1 to 10 m/s, and the response of structure is categorized as quasi-static (Richardson & Wisheart, 1996). LVI can happen at manufacture, operation, or maintenance of structure. The damage caused by LVI, in form of delamination, is categorized as barely visible damage. Delamination cannot be detected by visual inspection. It needs special method and tool to assess the damage. The existence of delamination lowers the strength of structure which includes buckling resistance and leads to easily-buckle structure.

Buckling on composite is still an interesting research topic. Many researches have been done to study buckling on composite. Juhász and Szekrényes (2015) has simulated buckling on composite with delamination and straight crack front. The damaged composite exposed to uniaxial compression load. The results shows that the delaminated plies buckles as plate, not as beam/column.

Prabhakaran et al. (2016) was analyzed the response of laminated composite exposed to tension, compression, and buckling load. The geometry of laminated composite was varied, and the simulations were done in

ANSYS 15.0. It was noted that the critical buckling load was reduced with increased length-to-thickness ratio of laminated composite.

Erdem et al. (2018) experimented and simulated buckling on laminated composite. The research had been done to analyze the behavior on pre-buckling and post-buckling of laminated composite with hole. It was noted that the stress concentration happened in hole edges, while the stress was small near free edges. The critical buckling load reduced with increased its hole diameter.

This research provides an analysis of buckling modes in undamaged laminate composite compared to modes in delaminated composite. The delamination is formed by LVI phenomenon, and the output of LVI will be used directly as input in buckling simulation. The composite that will be analyzed in this research is unidirectional composite HEXPLY AS4/8552, with ply stacking configuration $[-45^0/0^0/45^0/90^0]$s, exposed to LVI load with 19.3 Joule impact energy. The buckling modes will be compared one another, so the effect of LVI induced delamination on buckling failure in laminated composite can be concluded. The objectives of this research by simulation are to assess the damage in the form of delamination inside the laminated composite after low velocity impact, and determine the reduction of critical buckling load of laminate composite, compared to critical buckling load of undamaged composite, by the result of FEM simulation.

2 Methodology
2.1. Simulation Data
Material properties for HEXPLY AS4/8552 was taken from NCAMP Wichita lab test. Damage evolution

properties was provided by Gonzalez et. al. (2012) in their research about low velocity impact on composite. The properties will be inputted as material for continuum shell element with Hashin-Rotem model. Properties for composite's model are shown in Table 2-1.

2.2. Model

There are two stages of simulation for this research. The first simulation is LVI model. LVI model designed with reference to ASTM D7136 for measuring damage resistance of composite exposed to impact damage.
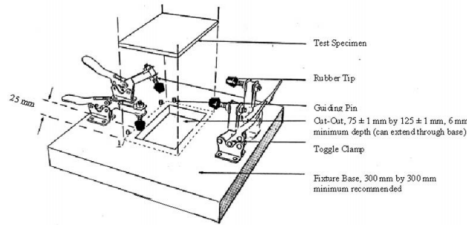
Figure 2-1: Impact damage testing on composite configuration

from ASTM D7136 (ASTM D7136, 2012)

The laminate composite model has 150 mm length and 100 mm width, with 5.8 mm thickness. The baseplate will follow the laminate's dimension, with 125x75 mm^2 rectangle shaped cutout in the middle. The baseplate, impactor, and rubber pins will be modeled as analytical rigid body. A 5 kilogram mass will be applied in the center of gravity of the impactor. The impact energy for this research is 19.3 Joule which translates to 2.779 m/s impactor speed.

The laminaes is modelled with continuum shells element, and the interfaces between the laminaes is modelled with cohesive element. There are 7 laminaes and 6 interfaces in the composite model. Mesh size for the model is 1.25 × 1.25 mm^2, considering the computation time and accuracy of simulation results. LVI model can be seen in Figure 2-2 and Figure 2-3.

Table 2-1: HEXPLY AS4/8552 Material Properties

	HexplyAS4/8552	Value	Unit
Hashin Damage	Xt (Fiber tension strength)	2063.05	MPa
	Xc (Fiber compress strength)	1484.37	MPa
	Yt (Transverse tension str)	63.91	MPa
	Yc (Transverse compress str)	267.86	MPa
	Tau12 (In-plane shear str)	91.56	MPa
	Tau23 (Transverse shear str)	133.93	MPa
Damage Evolution	**Fracture toughness (Gc)**		
	GcLT (Longitudinal tensile)	81.5	N/mm
	GcLC (Longitudinal compress)	106.3	N/mm
	GcTT (Transversal tensile)	0.28	N/mm
	GcTC (Transversal compress)	0.79	N/mm
Elastic	E1 (Fiber direction stiffness)	131610	MPa
	E2 (Transverse fiber stiffness)	9238.98	MPa
	Niu12 (In-plane Poisson's ratio)	0.302	
	G12 (In-plane shear stiffness)	4826.33	MPa
	G23 (Transverse shear stiffness)	3548	MPa
	G13 (Longitudinal shear stiffness)	4826.33	MPa
Density		1.59E-09	tonne/mm^3
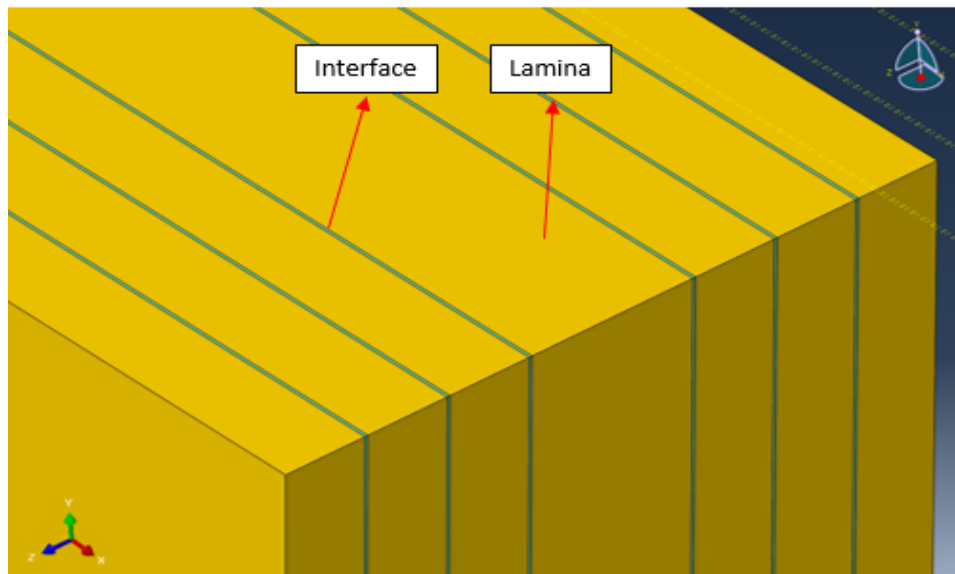
Figure 2-2: Laminaes and Interfaces in model shown by yellow elements and turquoise elements respectively
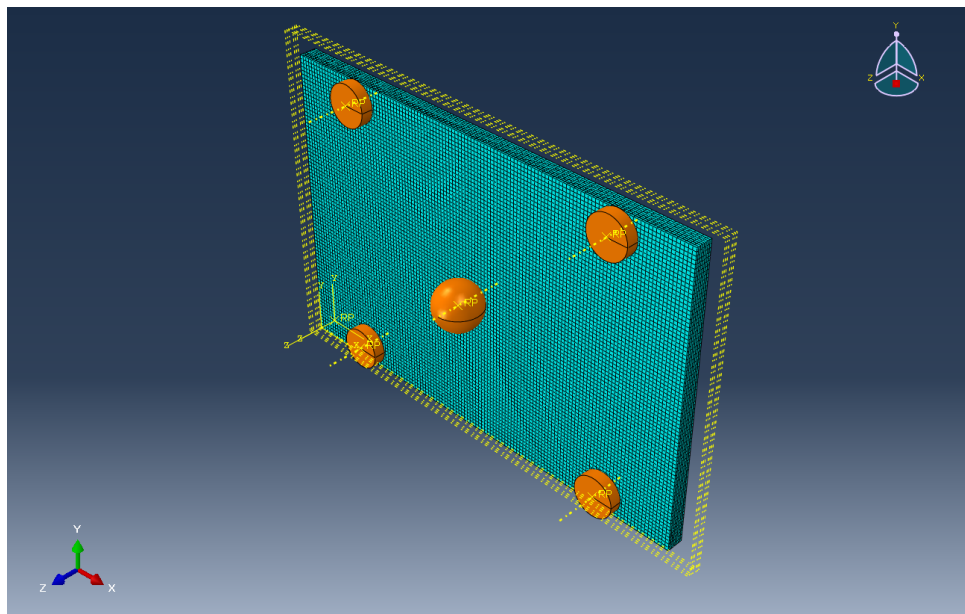
Figure 2-3: Model for low velocity impact on laminated composite

The laminaes will be modeled as continuum shell elements. It follows the Hashin-Rotem damage criterion as failure criterion for laminaes. The equations for Hashin-Rotem criterion is shown below,

Fiber Tension

$$(\sigma_{11} \geq 0) : F_f^t = \left(\frac{\sigma_{11}}{X^T}\right)^2 + \alpha \left(\frac{\tau_{12}}{S^L}\right)^2$$

(2-1)

Fiber Compression

$$(\sigma_{11} < 0) : F_f^c = \left(\frac{\sigma_{11}}{X^C}\right)^2$$

(2-2)

Matrix Tension

$$(\sigma_{22} \geq 0) : F_m^t = \left(\frac{\sigma_{22}}{Y^T}\right)^2 + \left(\frac{\tau_{12}}{S^L}\right)^2$$

(2-3)

Matrix Compression

$$(\sigma_{22} < 0) : F_m^c = \left(\frac{\sigma_{22}}{2S^T}\right)^2 + \left[\left(\frac{Y^c}{2S^T}\right)^2 - 1\right]\frac{\sigma_{22}}{Y^c} + \left(\frac{\tau_{12}}{S^L}\right)^2 \qquad (2\text{-}4)$$

In equations above X^T and X^c stands for tensile and compression strength of laminae in longitudinal direction. Y^T and Y^C stands for tensile and compression strength of laminae in transversal direction. S^L and S^T stands for longitudinal and transversal shear strength, while α represents shear stress coefficient and σ and τ as stress tensor. In this research, the value of α is zero, meaning it is assumed that the shear stress has no effect on fiber tension failure.

The interfaces of laminaes will be modelled as cohesive zone model. Cohesive zone model virtually models the traction-separation behavior of cohesive elements. There are two modes of separation in cohesive zone model, the peeling mode and sliding mode.
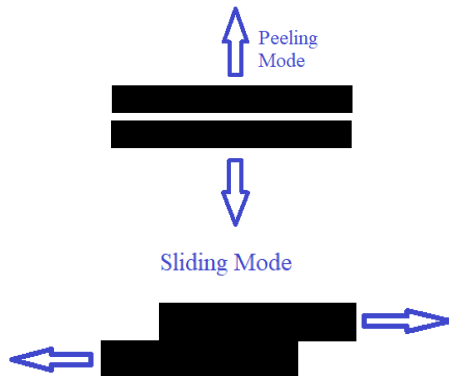
Figure 2-4: Two modes of separation in CZM

The CZM models the relation of traction and separation (Shi, 2008). The expressions for this model are,

Traction-Separation

$$\{t\} = [k]\{\varepsilon\} \qquad (2\text{-}5)$$

Softening / Stiffness Reduction

$$k_i^{fail} = k_i(1 - d_i) \qquad (2\text{-}6)$$

From the Eq. (2-5), ε stands for strain vectors of separation, t stands for traction vectors, and k represents stiffness matrix of cohesive zone. Before failing, the relation between traction and separation can be considered as linear relation. After the cohesive zone fails, softening will happen in cohesive zone, as shown in Eq. (2-6). The softening will causing reduction of cohesive material stiffness. This softening depends on the value of fracture energy, damage evolution factor, and damage variable *d*. if the damage factor *d* has reached 1, the cohesive zone will lost its stiffness, and can be considered as material failure. By those equations, the damage in cohesive zone can be modeled in simulation.

CZM modelling is used in this research, considering the capability of this model to capture the delamination at the interfaces of laminaes. By calculating the fiber and matrix stresses in lamina with Hashin-Rotem damage criterion and its relation to the traction-separation effect in cohesive layers, delamination profile can be predicted. This method assumes only the interlaminar shear stress and interlaminar normal stress that takes account on delamination process (Seno, 2016).

The delamination result of LVI is used as an input for buckling simulation. The simulation is performed to assess the delaminated composite behavior which is exposed to buckling load. The compression force of 1 Newton is applied to the plate. Here, the simply supported boundary condition applies to the plate edges. The model for buckling simulation is shown in Figure 2-5.

The outputs of buckling simulation of the laminate composite are the eigenvalues and the corresponding mode shape of buckling. The mode shape shows the possibility of deformation in

structure. The eigenvalues determine the value of critical buckling load. The equation to determine the value of critical buckling load is shown below,

Critical buckling load

$$P_{cr} = F \; x \; \lambda$$

(2-7)

Where P_{cr} represents the critical buckling load, F as the applied load in simulation, and λ as the eigenvalue from the simulation result.
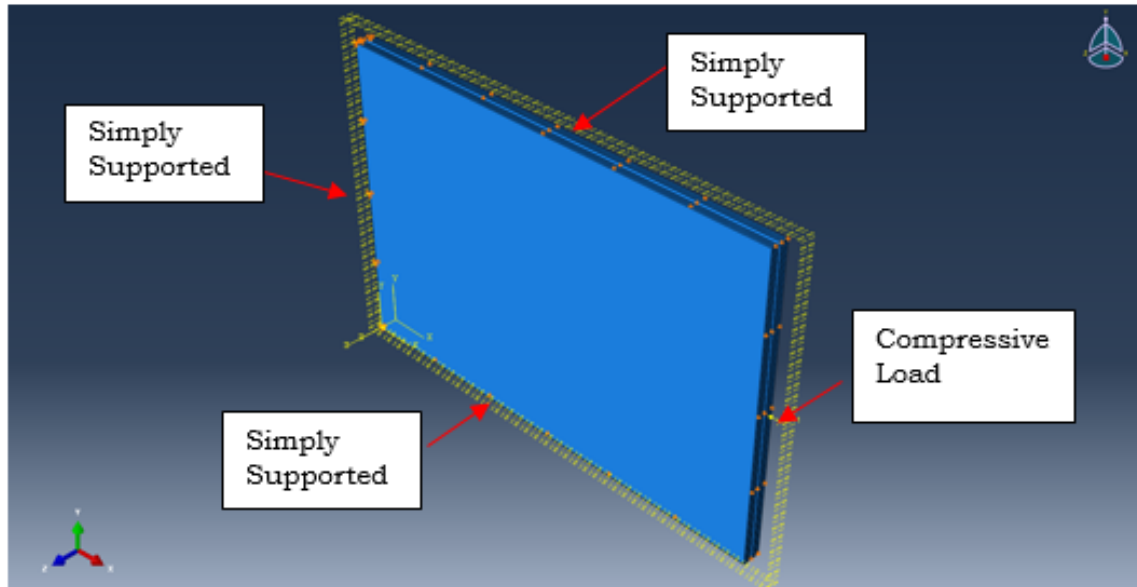
Figure 2-5: Model for buckling simulation

3 Result and Analysis
3.1 LVI Simulation Results

To validate the result of low velocity impact simulation, the energy parameters will be observed. The graph for energy parameter can be seen in Figure 3-1. The total energy ETOTAL must be relatively constant in every time step. The artificial energies such as ALLAE-Artificial Energy parameter, and ALLVD-Viscous Dissipation parameter must be smaller compared to ETOTAL. This means that in every time step, the artificial energies created by the elements in the model are tolerable. In this simulation, the ETOTAL has a constant value over time and the artificial energy parameters are small compared to total energy, as seen in graph. The result of LVI simulation can be considered valid for the given model and material property.

The result of LVI simulation is delamination profile of the plate after

110

impact. By the result of simulation, the delamination can be shown per interface or as C-Scan type display. The delamination profile in C-Scan type is shown in Figure 3-2. This research focuses only in the effect of delamination to buckling resistance reduction, so the damage in the laminae will not be shown.

The red area indicates the value of damage variable *d* has reached 1.0 and the interface has lost its stiffness, as stated in Eq. (2-6). This means the red area indicates the delaminated interface. Greenish boundary indicates the scalar damage is still below 1.0, and the material has experienced softening, but not yet fail. Blue area means the interface is still intact, and no delamination occurred in this area.

The damage of laminae is governed by the Hashin-Rotem criterion (Eq. (2-1)~(2-4)). It is noted that the value of stress tensors in a laminae is different

from other laminae, depends on its orientation. This causing a difference of deformation tendencies in a laminae with another, so the damage shape in every laminae is different from the others, and follows its fiber orientation.

There is a tendency for delamination in every interface to follow a peanut-like shape. This is because the delamination shape of the interfaces follows the damage in laminae below (Abrate, 1998). As stated before, every laminae has its damage shape, and the difference in deformation tendency will induce interlaminar stress between laminaes. The crack propagation as the effect of impact and interlaminar stresses will

Delamination	Value	Unit
C-Scan	6398	mm^2
Total	8194	mm^2

induce the delamination in interface, and it will follow the same stress path with laminae below, creating a peanut-like shape. The size of area depends on the value of interlaminar shear stress, interlaminar normal stress, and the difference in ply orientation.

From the delamination output, total area and C-Scan area of delamination can be known. The delamination area from the result of LVI simulation is shown in Table 3-1.

Table 3-1: Delamination Area

C-Scan area refers to area of projected delamination, meanwhile the total area refers to summation of delaminated area of every interfaces. In experiment of LVI, C-Scan area is preferable for output because of its extraction method. The total area will be more difficult to extract and need a special method and tool to extract. From the result of simulation, largest delamination profile was found in interfaces near neutral axis. The shear stress is the largest near the neutral axis. This stress plays a big role in delamination process. Large value of shear stress near neutral axis, plus interlaminar normal stress from impact will create large-sized delamination in the interfaces near neutral axis.
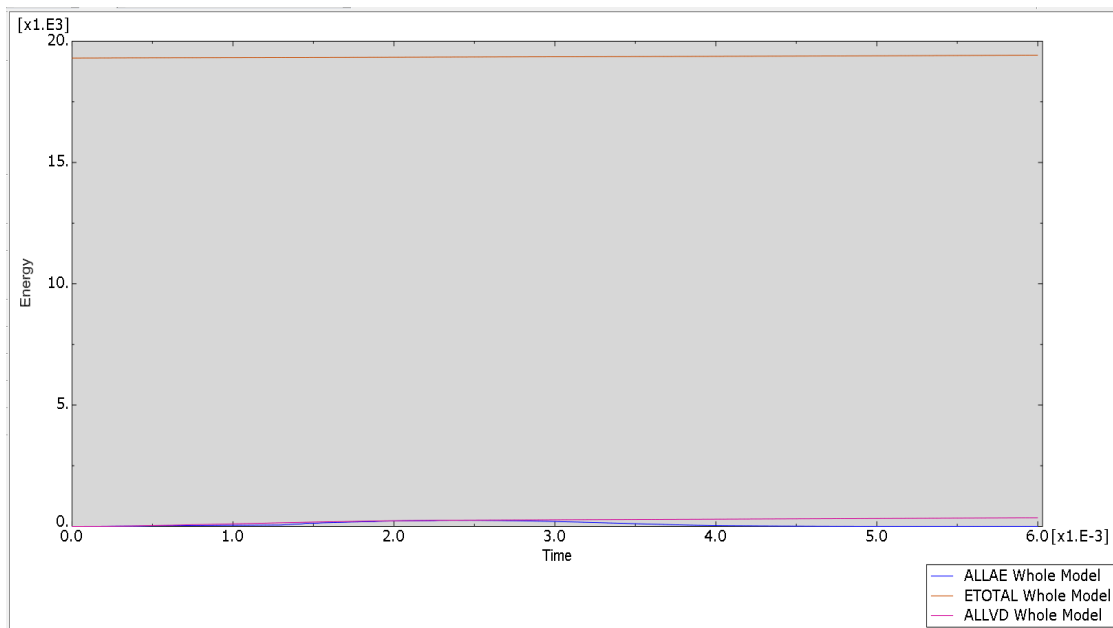
Figure 3-1: Energy history graph
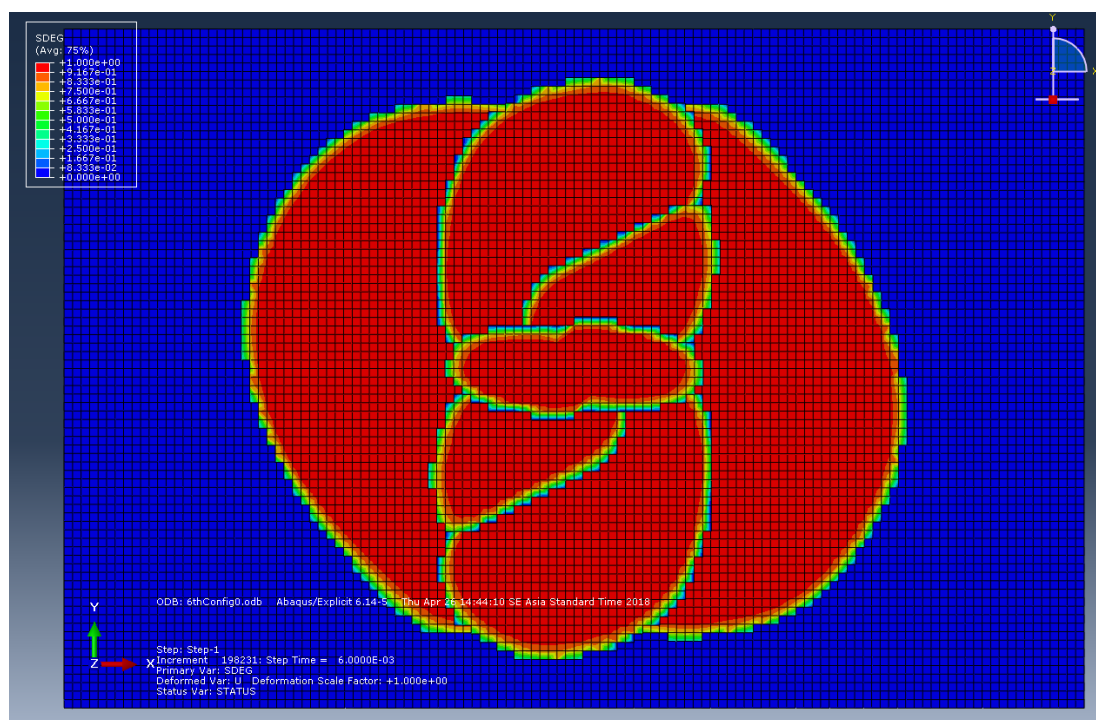
Figure 3-2: C-Scan of delamination

3.2 Buckling Simulation Results

The result from LVI will become input for buckling simulation. There are two simulations for buckling analysis. The first one is buckling on undamaged plate, and the second is buckling on delaminated plate, by the result of LVI simulation. As stated before, the preload for this simulation is compression load of 1 Newton.

The outputs of the simulation are eigenvalues and eigenvectors of plate.

The eigenvalues can be used to determine the value of critical buckling load in every mode by multiplying the eigenvalues with preload, as stated in Eq. (2-7). The positive eigenvalues and critical buckling load for the first three modes and their corresponding critical buckling load can be seen in Table 3-2. The graph showing the difference of P_{cr} visually for every mode is shown in Figure 3-3.

Table 3-2: Eigenvalues and critical buckling

Mode	Delaminated		Undamaged	
	Eigenvalue	Critical Buckling Load	Eigenvalue	Critical Buckling Load
1	24618	C: 24618 N	259956	C: 259956 N
2	28413	C: 28413 N	361768	C: 361768 N
3	39835	C: 39835 N	453540	C: 453540 N

*C refers to compression load
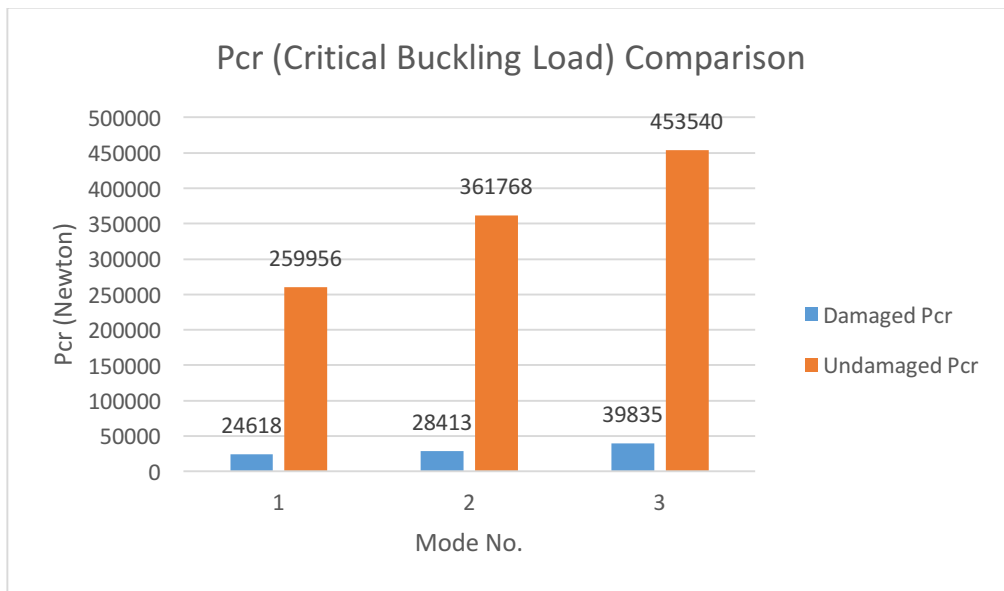
Figure 3-3: Critical buckling load comparison graph

Table 3-3: Isometric and top view of plate buckling profiles

Mode	Undamaged	Damaged
1		
2		
3		

From the result of simulation, we can see that the critical buckling load is reduced in delaminated composite compared to undamaged composite. The corresponding critical buckling of mode 1 for delaminated and undamaged model are 24,618 N and 259,956 N, for both are compressive load. There is more than 90% reduction on critical buckling load in delaminated composite mode 1, compared to critical buckling of undamaged composite mode 1.

Table 3.3 is showing the result of corresponding buckling shape of every

mode. It is observed that the buckling shape for undamaged composite is more visible than the damaged one. In first glance, it looks like there is no deformation in the damaged composite. But, the deformation is actually happening inside the composite, especially in the delaminated interfaces.

The example of the buckling profile in interface can be seen in Figure 3-4. The comparison of deformation in interface between damaged and undamaged composite can be seen in Figure 3-5.
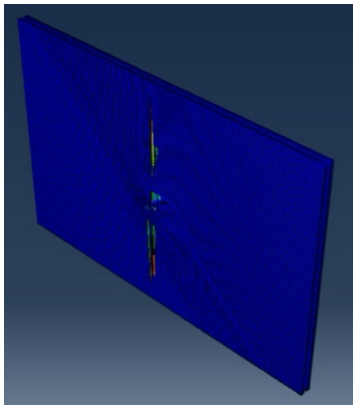
Figure 3-4: Buckling profile in delaminated interfaces for mode 1
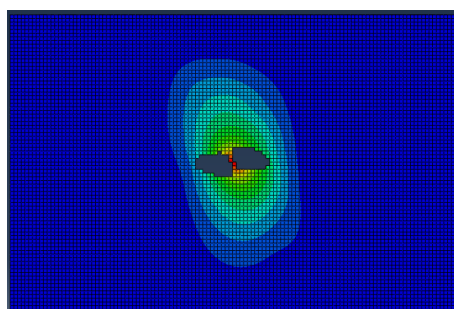
(a)
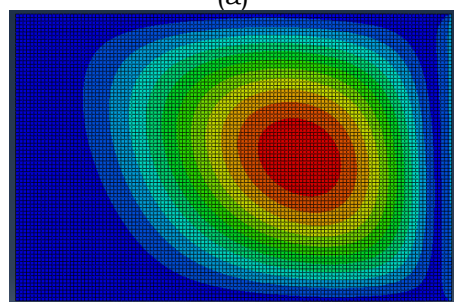
(b)

Figure 3-5: Buckling profile in interfaces for mode 1 ((a) damaged composite and (b) undamaged composite)

In undamaged composite, the buckling shape of interface will follow the shape of whole plate. It is because there is no imperfection inside the composite, and so the laminaes and interfaces deform as one plate. While in damaged composite, the existence of imperfection makes the interfaces deform on their own, thus the stability of plate is reduced. The delamination was seen to cause instability in every interfaces. Even the slightest deformation can make the composite unstable. This causes significant reduction of critical buckling load in damaged composite.

The existence of imperfection such as delamination or void inside composite can be a source of structural instability that will lead to easily deformed structure when exposed to a certain type of load. The imperfection induces inhomogeneity inside the composite, so the interfaces and laminaes tends to deform on its. Meanwhile, the result of buckling simulation on undamaged composite shows high critical buckling load result, because of the lack of imperfection inside the structure. The unstability in undamaged composite with boundary condition similar to this research simulation will happen only when exposed to high compressive load.

4   Conclusions

This research shows that the LVI phenomenon and buckling on composite can be simulated and analyzed with finite element method. From the results of simulation and analysis, we can conclude that, LVI phenomenon can cause damage inside the laminated composite in form of delamination. In

this research, the total deformation inside composite is 8,194 mm², while the C-Scan delamination shows 6,398 mm² result area. The critical buckling load will significantly reduced with the existence of imperfection inside laminated composite - in this research it is delamination. In this research, 6398 mm² C-Scan delamination area can cause reduction of critical buckling load up to 90% of undamaged composite critical buckling value. It is because the delamination will causing structural unstability inside the composite. The instability, in form of deformation, is observed in the interfaces of delaminated composite. The undamaged composite shows high value result for critical buckling load, while the damaged composite will have its buckling resistance reduced.

Contributorship Statements

RAR developed the model for simulation, analyzed the result, and write the manuscript. MGS and HS acted as supervisor, method designer, and tools provider.

References

Abrate S., (1998). *Impact on Composite Structures.* Cambridge University Press, ISBN: 139780521473897.

Arani, A.G., Maghamikia, Sh., Mohammadimehr, M., and Arefmanesh, A., (2010). *Buckling analysis of laminated composite rectangular plates reinforced by SWNCTs using analytical and finite element methods,* Journal of Mechanical Science and Technology Vol. 25 Issue 3, 809-820.

Bhingare, N.H., *et al.*, (2017). *Stress Analysis of Hybrid Laminated Composite Plate by using Finite Element Method in MATLAB,* International Journal for Scientific Research and Development Vol. 5 Issue 10, 595-598.

Bipin, P.B., *et al.*, (2016). *Buckling Analysis of Laminated Carbon Fiber Composite Beam using Ansys.* International Journal of Engineering Research and Technology Vol.5 Issue 7, 399 – 404.

Erdem, S., Kaman, M.O., Gur, M., (2018). *Post-buckling behavior of carbon fiber epoxy composite plates,* Journal of Mechanical Science and Technology Vol. 33 Issue 4, 1723-1730.

Gonzalez, E.V., *et al.*, (2011). *Effects of ply clustering in laminated composite plates under low-velocity impact loading,* Composite Science and technology Vol. 71, 805 – 817.

Hadi, B.K., 2012. *Mekanika Struktur Komposit,* Lecture Notes, ITB Press.

Jeyaprakash, P., Prabhakaran, V., Devaraju, A., (2018). *Experimental and Numerical Analysis of Carbon Epoxy Fibre Composite under Buckling Load,* Materials Today: Proceedings 5, 14526-14530.

Juhász, Z., Szekrényes, A., (2015). *Progressive buckling of a simply supported delaminated othotropic rectangular composite plate,* International Journal of Solids and Structures.

Niu, M. C. (2010). *Composite Airframe Structures,* Hong Kong Conmilit Press, Ltd., ISBN: 9789627128069.

Prabhakaran, V., *et al.,* (2016). *Finite Element Analysis of Composite Structures Under Different Types of Loads,* International Journal of Engineering Science and Computing Vol. 6 Issue 8, 2631-2635.

Ramadhan, R. A., (2018). *Analisis Pengaruh Sudut Orientasi Lamina Terhadap Profil Delaminasi pada Kasus Low Velocity Impact di Komposit Laminat dengan Metode Elemen Hingga,* Bachelor Final Project Bandung Institute of Technology.

Reddy, K.M., *et al.,* (2013). *Buckling Anlysis of Laminated Composite Plates Using Finite Element Method,* International Journal of Engineering Sciences & Research Technoology, Vol. 2 Issue 11, 3281-3286.

Rees, D.W.A., (2009). *Mechanics of Optimal Structural Design: Minimum Weight Structures.* John Wiley & Sons, Ltd., ISBN: 9780470746233.

Richardson, M.O.W., Wisheart, M.J., (1996). *Review of low-velocity impact properties of composite materials.* Review Paper, Elsevier.

Seno, A.H. (2016). *Comparison Between Cohesive Zone and 3D Brittle Fracture Models for Simulating Composite Laminate Delamination in Low Velocity Impact,* Master Thesis Bandung Institute of Technology.

EFFECT OF ISOMER COMPOSITION OF HYDROXYL TERMINATED POLYBUTADIENE (HTPB) IN LOW SHEAR FLOW BEHAVIOR

Afni Restasari[1], Luthfia Hajar Abdillah, Retno Ardianingsih, Rika Suwana Budi
National Institute of Aeronautics and Space, Indonesia
[1]e-mail: afni.restasari@lapan.go.id

ABSTRACT

HTPB is an ultimate component of matrix builder for high-filled composite materials. Flow behavior of HTPB in low shear is crucial in casting the composite. Considering the characteristics of hydrocarbon, this work aims to investigate the effect of microstructures composition of HTPB on its flow behavior. In this work, HTPBs with different compositions of 1,4-*cis*, 1,2-*vinyl* and 1,4-*trans* microstructures were used. Fourier-Transform Infra-Red spectroscopy (FT-IR) was used to determine the composition. It was calculated as a ratio of peak area at710, 910 and 970 cm^{-1} for 1,4-*cis*, 1,2-*vinyl*, 1,4-*trans* isomers respectively. Viscosity was measured using a rotational viscometer at various low shear rates. It is found that HTPB with high 1,2-*vinyl*/1,4-*trans* isomers shows shear thickening behaviour, distinguished significantly from Newtonian flow of the others. It is suggested that mechanism of shear thickening involves a certain configuration of 1,2-*vinyl* and 1,4-*trans* isomers that builds different degrees of flow resistance from one to other shear layers. The configuration and flow resistance change among layers as shear rate increases.

Keywords: *Microstructures, Viscosity, Hydroxyl Terminated Polybutadiene, Flow behaviour, Shear thickening.*

1 Introduction

Composite solid propellant is a kind of rocket fuel. It is made of solid and liquid content. Solid contents are energetic particles, such as Ammonium perchlorate and aluminum. While liquid content is a polymer. The polymer has responsibility in processing propellant slurry as well as in building a strong network to adsorb solid contents. It gives impact on mechanical and physical properties of solid propellant (Hartaya, *et al.,* 2017).

To improve specific impulse of propellant, liquid content that has high capability for loading solid is preferable. For this reason, elastomer Hydroxyl Terminated Polybutadiene (HTPB)-based polyurethane is commonly used as propellant binder (Dey, *et al.,* 2015).
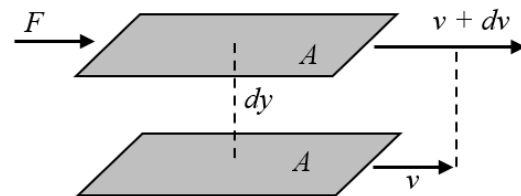
Figure 1-1: Illustration of viscosity of Newtonian fluid (Source: Onogi, 1982).

As a high-filled composite material, the processability of propellant becomes a significant issue. Propellant process involves mixing, casting and curing. An optimum process results in well-dispersed particles in propellant. It is important to prevent formation of void, pores, crazes and cracks. It is because the damage has a potential to induce failures in a motor rocket (Remakanthan, *et al.,* 2015). Parameters of this

processability include viscosity, pot-life and flow behavior (Dombe, *et al.,* 2008), , (Tomasz, *et al.,* 2018). However, investigation about the origin of the flow behavior is still limited.

Flow behavior is concerned about viscosity. Viscosity is a resistance of fluid to flow. It is illustrated in Figure 1-1 where two liquid surfaces move in parallel. The medium is a flowing viscous liquid. Surfaces move with force F, area A and distance dy. An ideal viscous liquid is liquid that flows when any force, other than hydrostatic pressure, acts. The deformation of the liquid does not recover even if the force is removed. Assuming that the flow velocity is large, $dv/dy = D$ is the velocity gradient and $F/A = \sigma$ is shear stress. D is equal to shear rate, γ. For Newtonian fluid, viscosity, η, is governed by using Eq. (1-1) (Onogi, 1982).

$$\sigma/D = \sigma/\gamma = \eta \qquad (1\text{-}1)$$

$$\eta = k. \ \gamma^{n-1} \qquad (1\text{-}2)$$

For Newtonian fluid, viscosity is independent of shear rate. While, for shear thinning or quasi-viscous flow, viscosity decreases with increasing shear rate. For shear thickening, structural viscosity increases with increasing shear rate. Both types of fluid follow Power Law model in Eq. (1-2) where k is consistency index and n is flow behavior index. Shear thinning is indicated by $n > 1$. Shear thickening is indicated by $n < 1$ (Onogi, 1982).

Propellant slurry is reported to have flow behavior that depends on the kind of liquid content. Glycidyl azide polymer (GAP)-based propellant shows almost Newtonian flow (Manu, 2009). While HTPB-based propellant shows shear thinning (Abdillah, *et al.,* 2020), (Ardianingsih & Kumoro, 2019), (Restasari, *et al.,* 2018). It has been

118

reported that the ideal value of n for HTPB-based propellant is 0.8 – 1 for vacuum top casting and 0.6 - 1 for pressure casting (Dombe, *et al.,* 2008). To obtain those values, controlling the flow index of HTPB is crucial. The control needs a sufficient understanding about the origin of HTPB flow behaviour
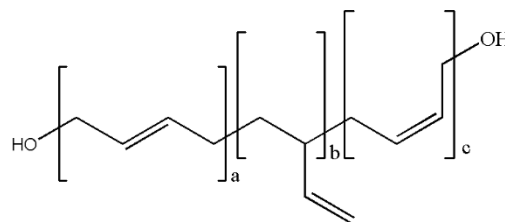
Figure 1-2: Microstructures of HTPB with 1,4-*trans* (a), 1,4-*cis* (b) and 1,2-*vinyl* (c) isomers (Source: Dey et al., 2015).
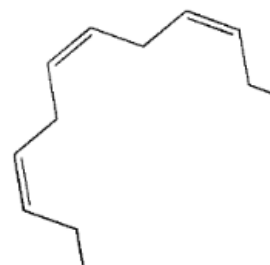
(a) Spring-like structure of 1,4-*cis* isomer
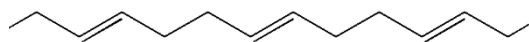
(b) Rod-like structure of 1,4-*trans* isomer

Figure 1-3:Assumption of 1,4-*cis* and 1,4-*trans* isomers of HTPB (Source: Dey, Sikder, & Athar, 2017).

HTPB consists of hydroxyl groups and hydrocarbon chain. In HTPB-based polyurethane binder, hydroxyl groups of HTPB act as hard segment builder. While a long hydrocarbon chain is soft segment

builder (Dey, *et al.,* 2015), (Rosita, 2016), (Wibowo, 2015).

Soft segment of an elastomer is reported to affect glass transition temperature (T_g) that strongly affects mechanical properties (Kida, *et al.,* 2020). For HTPB, it consists of 1,4-*cis*, 1,4-*trans* and 1,2-*vinyl* isomers described in Figure 1-2. It is reported that the percentage of 1,4-*cis* isomer affects the elasticity (Zhang, *et al.*, 2019), 1,4-*trans* isomer build the tensile strength and 1,2-*vinyl* isomer has role in governing viscosity of propellant. Effects of 1,4-*cis* and 1,4-*trans* isomers are assumed to be originated from its spring-like and rod-like shape respectively (Dey, *et al.*, 2015, 2017). It is described in Figure 1-3. The 1,2-*vinyl* isomer effect is from its anchor-like pendant structure. The structure has stereoregularity including atactic, isotactic and syndiotactic, described in Fig. 1-4 (Dey, *et al.*, 2015, 2017).

Viscosity is related to fluid resistance. It is correlated not only with the structure of isomers but also friction of isomers. The friction is measured as monomeric friction coefficient, ξ_0. With assumption that isomers in HTPB is similar with polybutadiene, it is reported that value of ξ_0 for 1,4-*cis* and 1,4-*trans* isomers are same. It is log ξ_0 = -6.75 dynes-sec/cm at 25 ℃ and different from 1,2-*vinyl* isomer. The value is ξ_0 = -4.11 dynes-sec/cm (Ferry, 1980). With the difference value of ξ_0, viscosity of HTPB can be assumed as viscosity of polymer mixture and approached by Rouse theory.
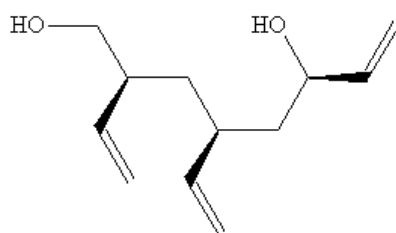
(a) Isotactic
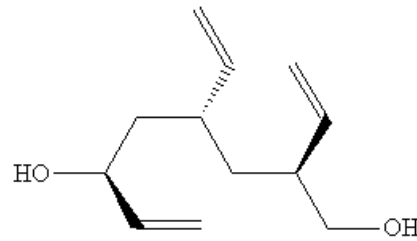
(b) Syndiotactic
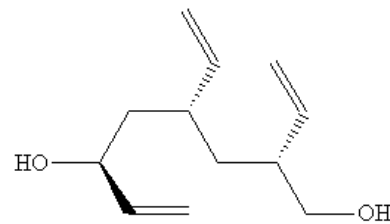
(c) Atactic

Figure 1-4: Stereoregularity of 1,2-*vinyl* isomer of HTPB (Source: Dey, *et al.*, 2015).

Based on Rouse theory, viscosity of polymer mixture is a sum of viscosity of the components multiplied by its free volume and friction factor. Friction factor is friction coefficient of mixture divided by friction coefficient of component. The approach is strengthening by difference value of free volume, v, which is space in a solid or a liquid that is not occupied by polymer molecules. Value of log v of polybutadiene at 25 ℃ and G' = 108 dyne/cm² for 1,4-*cis* and 1,4-*trans* isomers are same, 6.1. While for 1,2-*vinyl* isomer, it is 3.9 (Ferry, 1980).

With an approach towards Rouse theory, it is hypothesized that composition of 1,4-*cis*, 1,4-*trans* and 1,2-*vinyl* isomers has an important role in governing flow behaviour of HTPB. Therefore, this research aims to investigate the effect of microstructures composition of HTPB on flow behavior of HTPB.

2 Methodology

2.1. Sample Preparation

In this study, three types of HTPBs were used, named HTPB A, B and C. The specifications include average molecular weight of 2300 – 3500 g/mole, hydroxyl value of 0.81 – 1.0 mmole/g, polydispersity of 1 - 2.5 and hydroxyl number of 47.1 mm KOH/g. HTPB A and B were produced by Dalian Chlorate, Ltd, while HTPB C was produced by Hanwha. HTPB A samples was taken from a fresh opened package, while HTPB B had been stored for 2 years.

2.2. Experimental

To investigate flow behavior, viscosity of each HTPB was measured accurately at room temperature using Brookfield Viscometer with rotational spindle. The rotational speed of 0.17, 0.2 and 0.33 rps were applied to represent low shear regions. Low shear region was chosen to represent shear rate region of mixing and casting that is conducted in range of 0.1 – 10 rps (Green, 2004). Flow index that represents flow behavior was determined by fitting graph of η vs γ to Eq. (1-2). While zero shear viscosity or ZSV (η_0) that represents structure of fluid was determined by fitting graph of log η vs log ($\gamma+1$) to Eq. (2-1) (Goh & Wan Nik, 2018).

$$\log \eta \; = \; n \, log \, (\gamma + 1) \; + \; log \, \eta 0 \qquad (2\text{-}1)$$

In order to identify microstructure contents, each HTPB was carefully subjected to Fourier-Transform Infrared Spectroscopy (FT-IR) (Shimadzu IR PRESTIGE-21) 3 times. The wavelength range covered 650 – 1010 cm^{-1}. The spectra of peak of 710, 910 and 970 cm^{-1} were defined accurately for 1,4-*cis*, 1,2-*vinyl* and 1,4-*trans* isomers, respectively. The compositions were determined as the ratio of peak area (Wibowo, *et al.,* 2019).

3 Result and Analysis

Figure 3-1 shows the plotting of viscosity of HTPB A, B and C in function of shear rate. It can be stated clearly that the behaviour of HTPB A is extremely different from HTPB B and C. HTPB A has a strong shear dependent. Its viscosity is 3 times increased in increasing shear rate from 0,17 - 0.3 rps. While, the flow of HTPB B and C are almost independent of shear. To measure the strength of shear dependence, determined flow indexes are presented in Table 3-1. In addition, Figure 3-1 also shows different viscosity at starting point of 0.17 rps. It indicates different zero shear viscosity that is analysed in Figure 3-2 and Table 3-2.
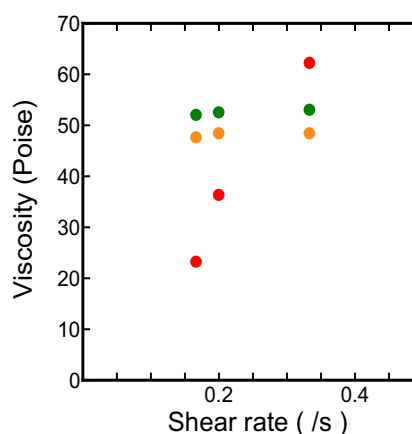
Figure 3-1: Viscosity (η) of HTPB A (red circle), B (green circle) and C (orange triangle) in function of shear rate (γ).

According to Table 3-1, the shear dependence of HTPB A is confirmed to be a shear thickening behavior with flow index of 2.343. This shear thickening is reported as the property of shock absorber polymer (Malvern Instruments Worldwide, 2016). The property is identical with HTPB. The behavior is also reported for paint, sand-rich material, kernel oil and coconut oil (Adewale, *et al.,* 2017), (Green, 2004), (Jeong, 2019). Those liquids have hydrocarbon chains similar with HTPB. HTPB B and C are

confirmed to have almost Newtonian behavior with flow index of 1.0255 and 1.0188, respectively. An almost Newtonian HTPB has been also reported with flow index of 1.0474 (Restasari, *et al.*, 2018).

Table 3-1: Flow index of HTPB

No	HTPB	Flow index	R^2
1	A	2.343	0.9549
2	B	1.0255	0.9289
3	C	1.0188	0.4947
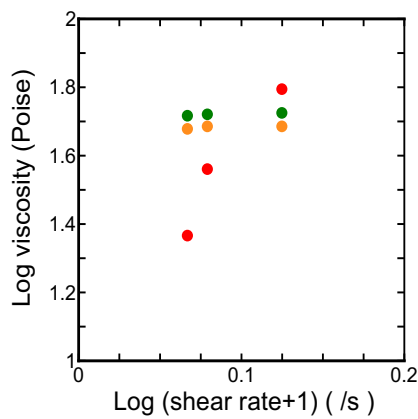
Figure 3-2: Logarithmic function of generalized viscosity model of HTPB A (red circle), B (green circle) and C (orange triangle).

Table 3-2: Zero shear viscosity of HTPB

No	HTPB	Zero shear viscosity (Poise)	R^2
1	A	9.16	0.9294
2	B	51.12	0.8981
3	C	47.23	0.4398

To analyze zero shear viscosity (ZSV), generalized viscosity model (Eq. (2-1)) is used. The plots are described in Figure 3-2 and determined values of ZSV are presented in Table 3-2. It shows various values of ZSV. The lowest is possessed by HTPB A while the highest is possessed by HTPB B. As ZSV has a positive correlation with molecular weight of polymer (Ferry, 1980), it indicates that the lowest average molecular weight is possessed by HTPB A and the highest average molecular weight is possessed by HTPB B. Considering the origin of the samples, storage period is reasonable for the difference. HTPB is reported to have an increase in molecular weight during storage (Wibowo, *et al.,* 2020).

Results of FTIR spectra are shown in Figure 3-3. For all kinds of HTPB, bending wagging vibration of the CH groups of 1,4-*cis* isomer is shown by a small peak at 710 cm^{-1}. Out-of-plane wagging vibrations of the CH$_2$ groups, located near 1,2-*vinyl* isomer, is shown by an obvious peak at 910 cm^{-1}. 1,2-*vinyl* isomer is also detected by peak at 990 cm^{-1}. The wavelengths are the same as previous reports (Li, *et al.,* 2019), (Wibowo, *et al.,* 2020). While, for out-of-plane wagging vibrations of CH groups near 1,4-*trans* isomer, the peak is shown broad and clear at 960 cm^{-1} and slightly different from the previous report. This difference is related to different chemical environments (Sone, 2016), (Wibowo, *et al.,* 2020).
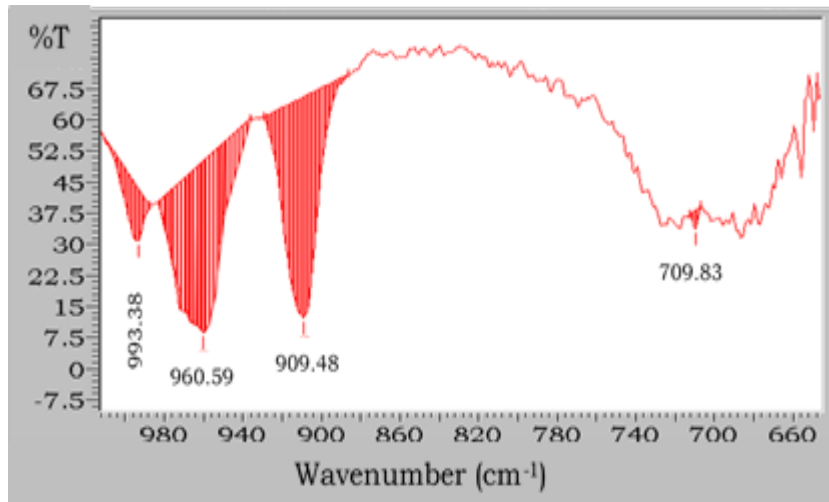
(a)
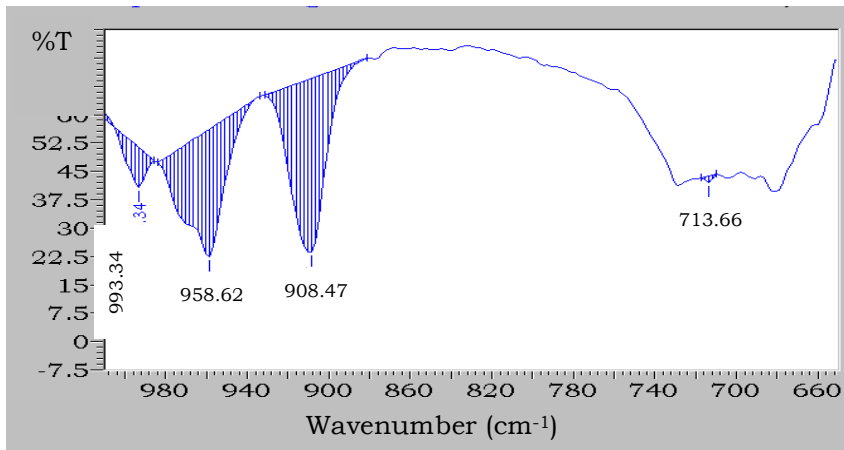
(b)
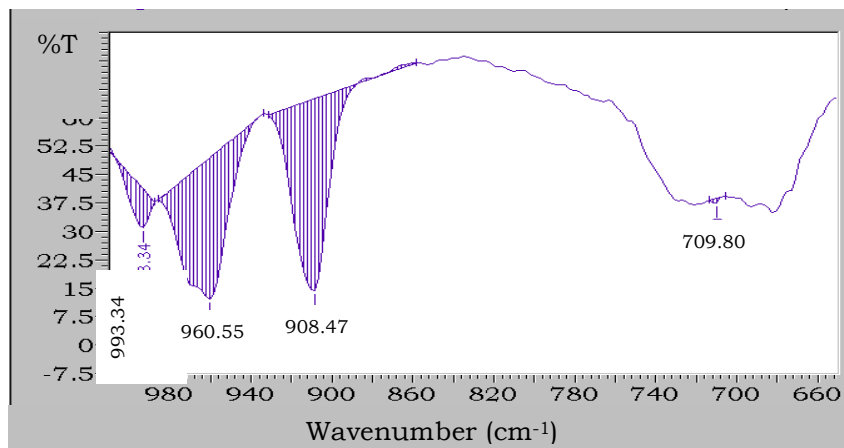
(c)

Figure 3-3:FT-IR Spectra for microstructures of (a) HTPB A, (b) HTPB B and (c) HTPB C.

Table 3-3: Microstructures Compositions of HTPB

HTPB	Microstructures Contents (%)		
	1,4-*cis*	1,2-*vinyl*	1,4-*trans*
A	0.1299	0.5254	0.3447
B	0.2374	0.4119	0.3507
C	0.0529	0.4019	0.5453

Microstructures contents are shown in Table 3-3. It is shown that 1,2-*vinyl* isomer is more dominant in HTPB A. However, for B and C, 1,2-*vinyl* isomers are similar. In previous report, HTPB with high 1,2-*vinyl* isomer content has high viscosity. However, in this research, viscosity of HTPB is more sensitive towards molecular weight than 1,2-*vinyl* isomer content (Dey, *et al.,* 2017), (Ferry, 1980), (Restasari, *et al,* 2015), (Wibowo, *et al.,* 2020). Considering different storage period, it has been reported that aged HTPB has less 1,2-*vinyl* isomer content (Akbaş, *et al.*, 1994).

Regarding flow behavior, in Table 3-1, HTPB B and C have similar *n.* While in

Figure 3-4, 1,2-*vinyl*/1,4-*trans* isomers of HTPB B and C is similar. While, *n* and 1,2-*vinyl*/1,4-*trans* isomers of HTPB A is the highest of all. Therefore, it is suggested that flow behavior comes from 1,2-*vinyl*/1,4-*trans* isomers. It is supported by different values of coefficient friction and free volume between 1,2-*vinyl* and 1,4-*trans* isomers that allow different behavior for different composition of 1,2-*vinyl*/1,4-*trans* isomers (Ferry, 1980).
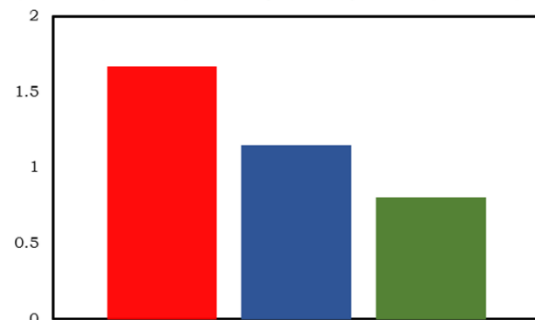
Figure 3-4: Ratio of 1,2-*vinyl*/1,4-*trans* isomers of HTPB A (red), B (blue), C (green).

(a)   (b)   (c)
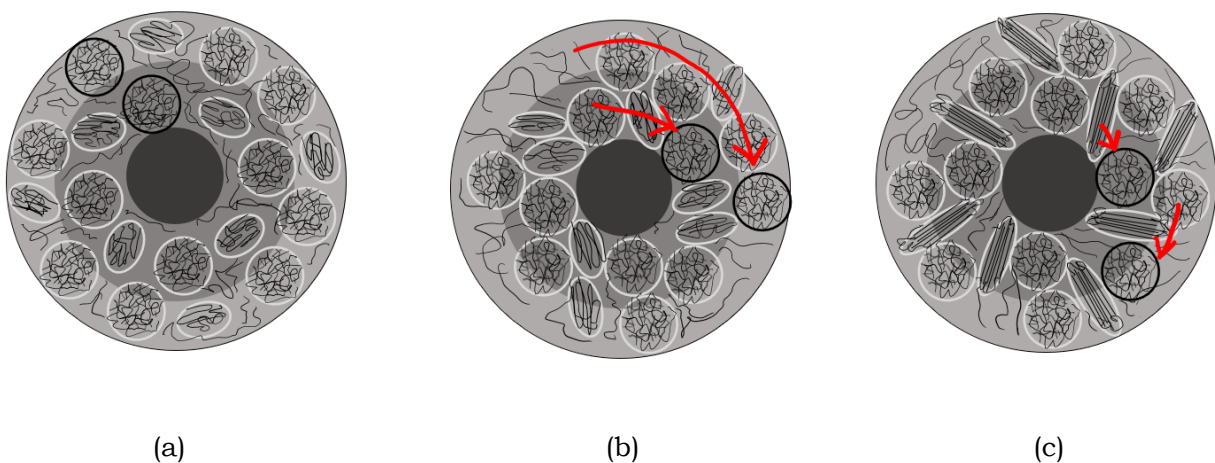
Figure 3-5. Illustration of Group A (1,2-*vinyl*-rich chain groups), sphere, and Group B (1,4-*trans*-rich chain groups), ellipsoid shape, in zero shear (a), under low shear rate (b) and high shear rate (c) of rotational shear.

123

In order to explain correlation between microstructures and flow behavior, illustration about motion of HTPB chain during rotational shear in viscosity measurement is given in Figure 3-5. It is shown that 1,2-*vinyl*-rich chain groups (Group A) and 1,4-*trans*-rich chain groups (Group B) flow under rotational shear with increasing shear rate. A wall slip is suggested to be occurred and divides area into 2 regions as also reported by Jeong *et al* (Jeong, 2019). Two regions are dark grey (Area 1) and light grey (Area 2). Area 1 is higher shear rate area, near spindle While Area 2 is the lower shear rate area, far from spindle.

In Figure 3-5, Group A and B are described by two different shapes. Group A is sphere because the pendant structure of 1,2-*vinyl* isomer is entangled and entraps to each other. It is assumed to build a big spherical knot. While Group B is ellipsoid. It describes relaxation of rod-like 1,4-*trans* chains. Moreover, it is assumed that Group A is heavier than Group B because Group A has higher friction coefficient. That friction allows Group A to hold more chain than Group B (Dey, *et al.,* 2017). In figure 3-5, two geometrical shapes, 1 of Group A and 1 of Group B, have bold lines as markers for motion.

As shear rate increases, shown in Fig. 3-5b, the geometrical shape of Group B can change. Shape of Group B changes to be more ellipsoid oriented towards flow direction. This orientation is affected by several factors. First, low friction and high free volume of 1,4-*trans* isomer make it easier to be oriented. Second, the structure of 1,4-*trans* isomer allows a neat arrangement of several 1,4-*trans* isomers combined together. Third, high stability of 1,4-*trans* isomer structure with heat of hydrogenation of 4 kJ/mole,

less than 1,4-*cis* and 1,2-*vinyl* isomers, makes 1,4-*trans* tend to maintain its rod-like structure. Fourth, the stiffness of 1,4-*trans* isomer makes it difficult to be relaxed, once oriented. This stiffness is proven by the value of Young Modulus. At 4 K, Young modulus of 1,4-*trans*-polybutadiene is 9.4×10^{10} dyne/cm^2, while 1,4-*cis*-polybutadiene is 8.7×10^{10} dyne/cm^2. Fifth, difficulties to be relaxed is supported with low temperature conditions (Ferry, 1980), (Li & Matsuba, 2017), (Prine, 2018), (Sridhar & Vernerey, 2018).

Different from Group B, Group A is illustrated to maintain its shape. However, in increase of shear rate, centrifuge force increase and it draws Group A to the center of rotation. As a consequence, Group A moves from Area 2 to Area 1. Thus, Area 1 becomes more crowded and has more resistance to flow. Group A is also possible to block flow in Area 2, for example, when a sphere in Area 1 meets a sphere in Area 2.

Centrifuge force also draws an ellipsoid Group B. The motion governs a slope with a certain angle of which 1 edge is in Area 1 and another edge is in Area 2. The edge that is in Area 2 inhibits flow in Area 2. However, there are still enough areas of free flow in Area 2 than Area 1.

As shear rate is more increased, described in Figure 3-5c, centrifuge force is stronger. This force induces three phenomena. First, Group A is stronger drawn to the center so that flow resistance in Area 1 is more governed. Second, because the tendency of Group A to be crowded in Area 1, it forces ellipsoid Group B to increase its slope and build a configuration that more inhibits flow in Area 2. Third, stronger centrifuge force strengthens all five factors mentioned that makes Group B more oriented. This high oriented structure increases the

stiffness of Group B. Stiffness can be represented as Young Modulus. It is reported that effective Young Modulus increases in the onset of shear thickening (Berret, *et al.*, 2001).

Based on the above illustration, microstructures of HTPB affects shear thickening through 3-steps mechanism. First, 1,2-*vinyl* and 1,4-*trans* isomers govern a certain configuration. Second, as shear rate increases, the configuration governs different flow resistances from one flow layer to the others. Third, as shear rate increases, both configuration and flow resistance of each layer changes. Although there is a report that extended chains in increasing shear rate flow, such as 1,4-*trans* in this case, reduce the viscosity (Dunstan, 2019), the causes of flow behaviour of HTPB are dominated by configuration of microstructures. Regarding Newtonian flow of HTPB B and C that have more 1,4-*trans* isomer content, its lower ratio of 1,2-*vinyl*/1,4-*trans* isomers governs a compact configuration in each shear layer. As shear rate increases, the configuration hardly allows any changes in flow resistance for each layer and in configuration itself.

4 Conclusions

In this work, investigation about effect of microstructures composition of HTPBs on its flow behaviour at low shear is conducted. The viscosity of three kinds of HTPBs with different compositions at various shear rates were measured by using rotational viscometer. It is found that HTPB with high 1,2-*vinyl*/1,4-*trans* isomers ratio performs shear thickening. With consideration of its physical properties, qualitative models of flow of those microstructures under increasing shear rate are illustrated. It is strongly suggested that 1,2-*vinyl* and 1,4-*trans* isomers govern certain configuration that induces different degree of flow

resistances among shear layers. These interlayer flow resistances are changes with increasing shear rate.

This work strengthens the importance in considering HTPB microstructures in order to obtain desired flow behavior whether of HTPB itself or its particle composite slurry. Moreover, about storage period, molecular weight and microstructures composition of HTPB are sensitive towards storage condition. Therefore, an improvement in storage condition of HTPB is advised.

Acknowledgements

Contributorship Statements

AR is the main contributor. LHA and RA checked data analysis. RSB and AR discussed the qualitative model.

References

Abdillah, L. A., Restasari, A., Hartaya, K., & Budiman, Y. (2020). The Selection of Composite Solid Propellant Process Condition Based on Flow Characteristics of Propellant Slurry The Selection of Composite Solid Propellant Process Condition Based on Flow Characteristics of Propellant. *AIP Conference Proceedings 2226, 040010.*

Adewale, F. J., Lucky, A. P., Oluwabunmi, A. P., & Boluwaji, E. F. (2017). Selecting the Most Appropriate Model for Rheological Characterization of Synthetic Based Drilling Mud. *International Journal of Applied Engineering Research, 12*(18), 7614–7629.

Akbaş, A., Aksoy, S., & Hasirci, N. (1994). Effects of thermal ageing on the properties and lifetime prediction of

hydroxyl-terminated polybutadiene. *Polymer*, *35*(12), 2568–2572.

Ardianingsih, R., & Kumoro, A. C. (2019). Analisis Viskositas Slurry Propelan Untuk Akurasi Karakterisasi Rheologi Berbasis Perekat Hidroxy Terminated Polybutadiene Dengan Plasticizer Dioctyl Adipate. *Teknik*, *40*(3), 154.

Berret, J.-F., Séréro, Y., Winkelman, B., Calvet, D., Collet, A., & Viguier, M. (2001). Nonlinear Rheology of Telechelic Polymer Networks. *Journal of Rheology*, *45*(2), 477–492.

Dey, A., Athar, J., Sikder, A. K., & Chattopadhyay, S. (2015). Effect of Microstructure on HTPB Based Polyurethane (HTPB-PU). *Journal of Materials Science and Engineering B*, *5*(3–4), 145–151.

Dey, A., Sikder, A. K., & Athar, J. (2017). Micro-structural Effect on Hydroxyl Terminated Poly Butadiene (HTPB) Prepolymer and HTPB Based Composite Propellant. *Journal of Molecular Nanotechnology and Nanomedicine*, *1*(1), 104.

Dombe, G., Jain, M., Singh, P. P., Radhakrishnan, K. K., & Bhattacharya, B. (2008). Pressure Casting of Composite Propellant. *Indian Journal of Chemical Technology*, *15*, 420–423.

Dunstan, D. E. (2019). The Viscosity-Radius Relationship for Concentrated Polymer Solutions. *Scientific Reports*, *9*(543), 1–9.

Ferry, J. D. (1980). *Viscoelastic Properties of Polymers* (3rd ed.). Canada: John Willey and Sons Ltd.

Goh, E. G., & Wan Nik, W. B. (2018). A Generalized Model for Viscosity as a Function of Shear Rate. *ARPN Journal of Engineering and Applied Sciences*, *13*(9), 3219–3223.

Green, P. (2004). Shear Viscosity , Rheology. *European Coating Journal*, (05), 48.

Hartaya, K., Budiman, Y., Restasari, A., Budi, R. S., Rohman, F., Wicaksono, B., … Prayoga, R. D. (2017). Analisis Komposisi Propelan Padat 320 Secara Komparasi, Prediksi, Uji Homogenitas dan Upaya Penyempurnaan. In R. A. Agustina & A. Marta (Eds.), *SIPTEKGAN XXI* (pp. 323–330). Tangerang: Pusat Teknologi Penerbangan, LAPAN.

Jeong, S. (2019). Shear Rate-Dependent Rheological Properties of Mine Tailings: Determination of Dynamic and Static Yield Stresses. *Applied Sciences*, *9*(4744).

Kida, T., Hamasaki, K., Hiejima, Y., Maeda, S., & Nitta, K. H. (2020). Microscopic origin of elastic and plastic deformation in poly(ether-block-amide) elastomers under various conditions. *Nihon Reoroji Gakkaishi*, *48*(3), 153–160.

Li, K., & Matsuba, G. (2017). Effects of Relaxation Time and Zero Shear Viscosity on Structural Evolution of Linear Low-density Polyethylene in Shear Flow. *Journal of Applied Polymer Science*, 1–9.

Li, P., Liu, K., Fu, Z., Yu, Y., Wang, Z., & Hua, J. (2019). Preparation of butadiene-isoprene copolymer with high 1,2-*vinyl* contents by Al(OPhCH3)(i-Bu)2/MoO2Cl2.TNPP. *Polymers*, *11*(3).

Malvern Instruments Worldwide. (2016). *Malvern Instruments White Paper - A Basic Introduction to Rheology Shear Flow*. 1–20. Retrieved from https://www.malvernpanalytical.com /en/learn/knowledge-center/whitepapers/WP160620BasicI ntroRheology.html

Manu, S. K. (2009). *Glycidyl Azide Polymer (GAP) as a High Energy Polymeric Binder for Composite Solid Propellant Applications*. Mahatma Gandhi University.

Onogi, S. (1982). *Rheology for Chemist.* Kyoto: Kagaku Doujin co. ltd.

Prine, N. (2018). *Characterization and Selection of Hydroxyl- Terminated Polybutadiene Polymers for High-Strain Applications by.* University of Southern Mississippi.

Remakanthan, S., Kk, M., Gunasekaran, R., Thomas, C., & Thomas, C. R. (2015). Analysis of Defects In Solid Rocket Motors Using X-Ray Radiography. *The E-Journal of Nondestructive Testing, 20*(6).

Restasari, A, Budi, R. S., & Hartaya, K. (2018). Pseudoplasticity of Propellant Slurry with Varied Aluminium Content for Castability Development. *Journal of Physics: Conference Series, 1005*(1).

Restasari, Afni, Abdillah, L. H., Budi, R. S., & Hartaya, K. (2018). Pengaruh Dioctyl Adipate Terhadap Sifat Rheologi HTPB Terplastisasi. *Jurnal Teknologi Dirgantara, 16*(2), 139–149.

Restasari, Afni, Ardianingsih, R., & Abdillah, L. H. (2015). The Effects of Hidroxy Terminated Polybutadiene (HTPB)`s Mass on The Magnitude of 1,2-*vinyl*`s Effects in Increasing Composite Solid Propellant Binder`s Rate of Increasing of Viscosity and Hardness. *Jurnal Teknologi Dirgantara, 13*(1), 61–70.

Rosita, G. (2016). Perubahan Karakteristik Pembentukan Poliuretan Berbasis HTPB dan TDI Berdasarkan Komposisi Reaksi. *Jurnal Teknologi Dirgantara, 14*(2), 159–170.

Sone, T. (2016). Industrial synthetic method of the rubbers. 1. Butadiene rubber. *Int. Polym. Sci. Tech, 43*, 49–54.

Sridhar, S. L., & Vernerey, F. J. (2018). The Chain Distribution Tensor: Linking Nonlinear Rheology and Chain Anisotropy in 1,4-*trans*ient Polymers. *Polymers, 10*(8), 1–17.

Tomasz, G., Katarzyna, G.-S., Karolina, J., & Lukasz, K. (2018). Rheological and Thermal Properties of Mixtures of Hydroxyl-Terminated Polybutadiene and Plasticizer (Rapid communication). *Polimery, 63*(1), 53–63.

Wibowo, H. B. (2015). Pengaruh Gugus Hidroksil Sekunder Terhadap Sifat Mekanik Poliuretan Berbasis HTPB (Hydroxy Terminated Polybutadiene). *Jurnal Teknologi Dirgantara, 13*(2), 103–112.

Wibowo, H. B., Dharmawan, W. C., Ratih, S., & Murti, S. (2020). Rapid Analysis of HTPB (Hydroxyl Terminated Polybutadiene) Properties with Infrared Spectroscopy and Gel Chromatography. *AIP Conference Proceedings 2226, 040012*(April).

Wibowo, H. B., Dharmawan, W. C., Wibowo, R. S. M., & Yulianto, A. (2019). Kinetic Study of HTPB (Hydroxy Terminated Polybutadiene) Synthesis Using Infrared Spectroscopy. *Indonesian Journal of Chemistry.*

Zhang, Q., Shu, Y., Liu, N., Lu, X., Shu, Y., Wang, X., … Xu, M. (2019). Hydroxyl Terminated Polybutadiene: Chemical Modification and Application of These Modifiers in Propellants and Explosives. *Central European Journal of Energetic Materials, 16*(2), 153–193.

.

COMPARATIVE STUDY OF WING LIFT DISTRIBUTION ANALYSIS USING NUMERICAL METHOD

Angga Septiyana[1], Kurnia Hidayat, Ardian Rizaldi, Yusuf Giri Wijaya
Aeronautics Technology Center, LAPAN
[1]e-mail: angga.septiyana@lapan.go.id

ABSTRACT

This research focuses on calculating the force distribution on the wings of the LSU 05-NG aircraft by several numerical methods. Analysis of the force distribution on the wing is important because the wing has a very important role in producing sufficient lift for the aircraft. The numerical methods used to calculate the lift force distribution on the wings are Computational Flow Dynamics (CFD), Lifting Line Theory, Vortex Lattice Method, and 3D Panel Method. The numerical methods used will be compared with each other to determine the accuracy and time required to calculate wing lift distribution. Because CFDs produce more accurate estimates, CFD is used as the main comparison for the other three numerical methods. Based on calculations performed, the 3D Panel Method has an accuracy that is close to CFD with a shorter time. 3D Panel Method requires 400 while CFD 1210 seconds with results that are not much different. While LLT and VLM have poor accuracy, however, a shorter time is needed. Therefore to analyze the distribution of lift force on the wing it is enough to use the 3D Panel Method due to accurate results and shorter computing time.

Keywords: *Wing Lift Distribution, CFD, 3D Panel Methode, LLT, VLM, Numerical Methode.*

1 Introduction

Wings have a very important role in producing sufficient lift force for airplanes. The lift force produced by these wings is the main lift force of an aircraft. Failure on the wing will make the aircraft lose lift and crash.

The estimation of the load on the wing will be determined by the wings component. Thus, failure happening on the wing could be rectified. One of the loads work on the wing is aerodynamic load.

The results of the analysis of lift force distribution along the wingspan can be used to predict aerodynamic loads in wing structures (Silitonga & Moelyadi, 2018). The method of estimating lift force distribution was first introduced by Prandtl in 1918. Prandtl introduced the first practical theory to estimate aerodynamic characteristics of finite wings (Anderson Jr, 2001). This theory is known as Lifting-line Theory (LLT). However, this theory still assumes that the coefficient of lift force linear to changes in the effective angle of attack, whereas after reaching the stall point the curve of lift force curve becomes nonlinear. (Anderson Jr, 2001) introduced an extensive model of the classical LLT developed by Prandtl to accommodate nonlinear areas on the curve of lift force coefficient to the effective angle of attack.

Lifting-line Theory model only applies to elliptic or straight wings, while for wing shapes that have a low aspect ratio, wings with swept angles, and a delta wing, this LLT model cannot be used.

Therefore, the Vortex Lattice Method (VLM) was developed by Margason in 1985. Vortex Lattice Method assumes the wing is a surface consisting of small elements in the form of horseshoe vortex or ring vortex (Bertin & Cummings, 2009).

Lifting-line Theory and VLM models are widely used by researchers to estimate the aerodynamic characteristics of aircraft wings. The basic LLT model developed by Prandt'l was modified by H.B. Helmhold in 1942 to accommodate the LLT model on a straight wing with a low aspect ratio (Anderson Jr, 2001). Meanwhile, (Küchemann, 1953) developed LLT in the case of wings with swept angles. The mathematical model of LLT was also developed (Sivells & Neelly, 1947), (Multhopp, 1955), and (Weber, Kirby, & Kettle, 1956). Recent research using the LLT method is related to the optimization of wing or aircraft design, such as research by (Fonseca, Pinheiro, & Arcos, 2018) and (Carvalho & Brito, 2017).

Vortex Lattice Method has been widely implemented in various software tools for conducting aerodynamic analysis in the early stages of aircraft design. The software includes Tornado (Melin, 2000), AVL (Buzdiak, 2015), and XFLR5 (Deperrois, 2013). (Gryte et al., 2018) conducted aerodynamic modeling of unmanned aircraft using wind tunnel data and numerical calculation data using the VLM method. Numerical data is obtained through XFLR5 software. (Loya, Maqsood, & Muhammad Duraid, 2018) analyzed the aerodynamic parameters of unmanned aircraft using XFLR5 with the VLM method whose results were compared with DATCOM and Computational Fluid Dynamics (CFD).

The more sophisticated technology makes fluid flow problems can be solved by numerical computation. CFD analysis allows us to get more accurate results but requires a longer computational time than previous methods. Comparisons between methods for estimating aerodynamic parameters have been made by (Loya et al., 2018), (Ugargol & Ugargol, 2017) and (Spall, Phillips, & Pincock, 2012). In addition, several studies have been conducted comparing CFD analysis with wind tunnel tests. (Choi, Yu, & Kwon, 2014) conducted a study on the comparison between CFD and wind tunnel experiments to analyze tall buildings. The results shown from the comparison are not much different although there are several different for certain cases. Fouad et al., (2018) also conducted a study on the comparison of CFD techniques with the results of wind tunnel data. The results obtained by the CFD give very accurate and good results. The resulting Kakatatan depends on the number of grids during the calculation process. These two studies show that CFD can be used as a base for comparing previous methods.

This research will discuss a comparative study of the performance of the LLT, VLM, Panel, and CFD methods in estimating lift force distribution in terms of accuracy and computational time. The purpose of this research is to lift the wing force distribution as a basis for experimental testing of the existing load on the wing. The output data from this study are used as a base for the experimental test

2 Methodology

The phenomenon of flying objects is inseparable from the presence of airflow on the object by to reduce force. This force is called the aerodynamic force. This aerodynamic force basically comes from the pressure and shear stress that occurs on the surface of the object as shown in Figure 2-1.
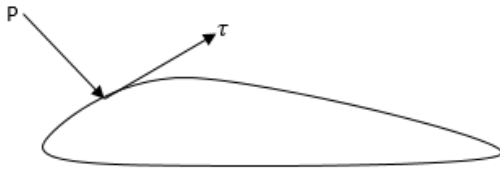
Figure 2-1: Pressure and shear stress

The pressure on each of these small surfaces accumulates resulting in the resultant forces and moments. Two types of force and moment components are determined based on the direction of the force that is the force in the direction of the object and the direction of the wind. This type of force component is illustrated in Figure 2-2.
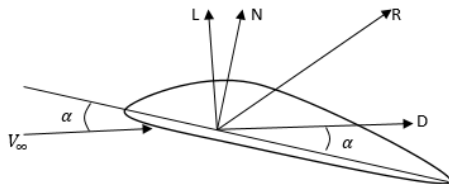
Figure 2-2: Resultant and component force

Where L is the lift force, that is the force component which is perpendicular to the wind direction (V_∞), while D is the drag force, that is the force component which is in the direction of V_∞. N is the normal force that is the force component which is perpendicular to c, while A is the axial force that is the force component which is in the direction of c. The angle of attack α is defined as the angle between the direction of the wind and c so that α can also be defined as the angle between L and N as well as D and A. Therefore, the following equation can be formed:

$$L = N\cos(\alpha) - A\sin(\alpha) \qquad (2\text{-}1)$$

$$D = N\sin(\alpha) + A\cos(\alpha) \qquad (2\text{-}2)$$

In the discipline of aerodynamics, some dimensionless forces and moments are often known as aerodynamic coefficients. For example ρ_∞ and V_∞ are the density and velocity of air in an open flow (freestream), then dynamic pressure can be defined as:

$$q_\infty = \frac{1}{2}\rho_\infty V_\infty{}^2 \qquad (2\text{-}3)$$

Dynamic pressure has the same units as pressure (Newton and similar units). For example, S is the area of an object reference and l is the object reference length, then the aerodynamic coefficient is defined as follows:

$$C_L = \frac{L}{q_\infty S} \qquad (2\text{-}4)$$

$$C_D = \frac{D}{q_\infty S} \qquad (2\text{-}5)$$

$$C_M = \frac{M}{q_\infty S l} \qquad (2\text{-}6)$$

2.2 Problem Definition

The process of making an airplane, especially on the wing, needs to be analyzed the distribution of forces that exist along the wing. This is done to make the structure of the aircraft wing so that it is strong with the weight of the aircraft. Because the load received by the wing is large, it is necessary to analyze the force distribution on the wing.

2.3 Method
2.3.1 Computational Fluid Dynamics

Computational Fluid Dynamics (CFD) is a numerical simulation tool for analyzing and designing fluid flow systems, heat transfer, and other fluid phenomena. In this study, CFD simulations are used to analyze the airflow that occurs in the area of the aircraft with the same actual flying conditions.

The basic concept of CFD is derived from physical phenomena that occur in the fluid. This phenomenon is described in a mathematical model called the governing equation. The general equation

commonly used to represent fluid flow behavior is the Navier-Stokes equation (Panagiotou, Kaparos, Salpingidou, & Yakinthos, 2016). For the assumption of incompressible flow, the Navier-Stokes equation is expressed as

$$\rho\left(\frac{\partial v}{\partial t} + (v\nabla)v\right) = -\nabla p + \mu\nabla^2 v + \rho F \qquad (2\text{-}7)$$

In general, CFD analysis is carried out in three major stages, namely:

1) Pre-processing
2) Solving
3) Post- Processing

In pre-processing there is a process of determining the turbulent model. This turbulent model is used to model fluid flows that move randomly and are unstable. In this study to solve this problem using the Shear Stress Transport model provided by ANSYS-CFX. The Shear Stress Transport model works by solving the models based on turbulence/frequency (k-ω) on walls and k-ε in fluid flow (Ansys, 2004). K-epsilon is a turbulent equation model with two equations to solve the turbulent kinetic energy k and the dissipation power ε. Whereas k-ω is an alternative equation to replace the k-epsilon equation. Similarly, the k-epsilon equation, the k-ω equation model is used to solve the turbulent kinetic energy k and the specific dissipation power ω. The advantage of k-ω compared to k-ε is that this equation increases the boundary layer performance due to pressure gradients.

2.3.2 Vortex Lattice Method.

Vortex Lattice Method is a numerical method used to analyze fluid dynamics. In principle, this VLM models a surface on an aircraft into an infinite number of vortices to analyze or calculate the pressure distribution on an aircraft, in this case, VLM can also be used to calculate the force distribution on an

aircraft. In this method, it is assumed that fluid flow is incompressible, inviscid and irrotational and the influence of thickness on force is neglected.

Based on the assumptions above, flow that is incompressible and irrotational, according to (Anderson Jr, 2001) can be synthesized by adding a similar elemntary flow of energy. The intended elemntary flow can be a point or a vortex line.

There are four important theories that are used to illustrate this effect and to model an air flow around the wing (Budziak, 2015). The four theories are

a. Biot-Savart Law
b. Kutta-Joukovsky theorem
c. Hermann von Helmholtz theory
d. Prandtl lifting-line theory

According to Biot-Savart's law the vortex line induces a certain velocity field, at any point P there is a distance r from a filament causing that speed to be induced by the vortex. This concept is illustrated in the picture
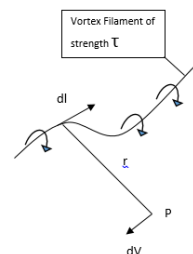
Figure 2-3: Ilustration of Biot – Savart Law

Based on the illustration in Figure 2-3, the form of a mathematical model of Biot-Savart law as follows:

$$dV = \frac{\tau}{4\pi}\frac{(dl \times r)}{|r|^3}$$

atau

$$V = \frac{\tau}{4\pi}\int\frac{(dl \times r)}{|r|^3} \qquad (2\text{-}8)$$

Where
 dl : infinite small filament partitions
 r : distance from point P to the point in the filament

τ : Vortex strength

V : Induced Speed

According to the Kutta-Joukowski theorem, certain moving vortex with the strength of the speed which is bound in the flow velocity V_∞ will produce lift force, in other words

$$L = \rho V_\infty \tau \qquad (2\text{-}9)$$

with

ρ : air density

V_∞ : Freestream speed

L : Lift Force (Lift)

Hermann von Helmholtz's theory illustrates the principle of a vortex filament must be from a closed path (eg vortex ring) and circulation along the vortex filament is constant.

Prandtl lifting-line theory describes vortex rings as horseshoe vortex. This is because the vortex ring can be changed into four vortex filaments that are definitely closed.

2.3.3 The 3D Panel Methode

The 3D Panel method in XFLR5 software is applied to analyze in 3D form by considering wing thickness. Different from VLM that only considers the mean camber line. Moreover 3D Panel method is also used to analyze the pressure distribution on the upper and lower surface of the wing. In principle, this method models the existing disturbance on the wing surface with a number of doublets and sources which is distributed above and below the wing surface (Deperrois, 2013). This method uses doublets and sources on a flat and linear panel. In detail, mathematical model for the 3D Panel method there is in reference.

2.4 VLM Model and 3D Panel Model

Numerical simulation using VLM and Panel Method to calculate the distribution of lift force on the wing as an initial prediction for the process of calculating the load analysis on the structure. In this calculation used XFLR5 software. XFLR5 is software used to analyze aerodynamic parameters in airfoil, wings and fuselage, also can be used to analyze full configuration.

Modeling using the first XFLR5 software requires airfoil coordinates which is the basis for making wings. Then with that input, wing model with XFLR5 was made and determine the number of elements on the wing. Figure 2-4 below is the result of wing modeling with XFLR5 software using VLM and Horseshoe Vortex analysis
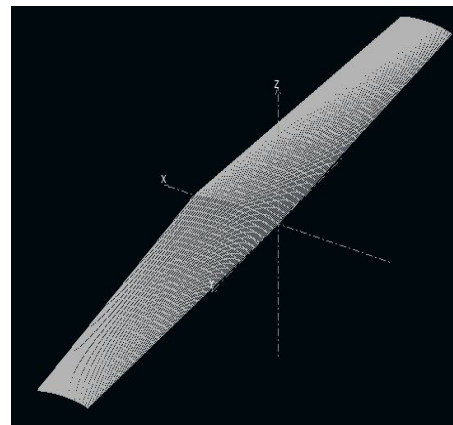
Figure 2-4: Image of wings with VLM and Horseshoe Vortex with XFLR5

While for the wing image using the 3D Panel Method on XFLR5 the image is obtained as follows
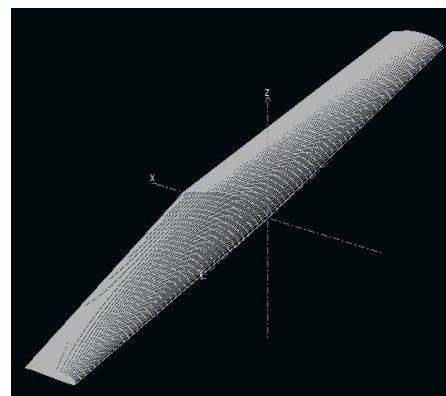
Figure 2-5: Image of wings with the 3D Panel Method with XFLR5
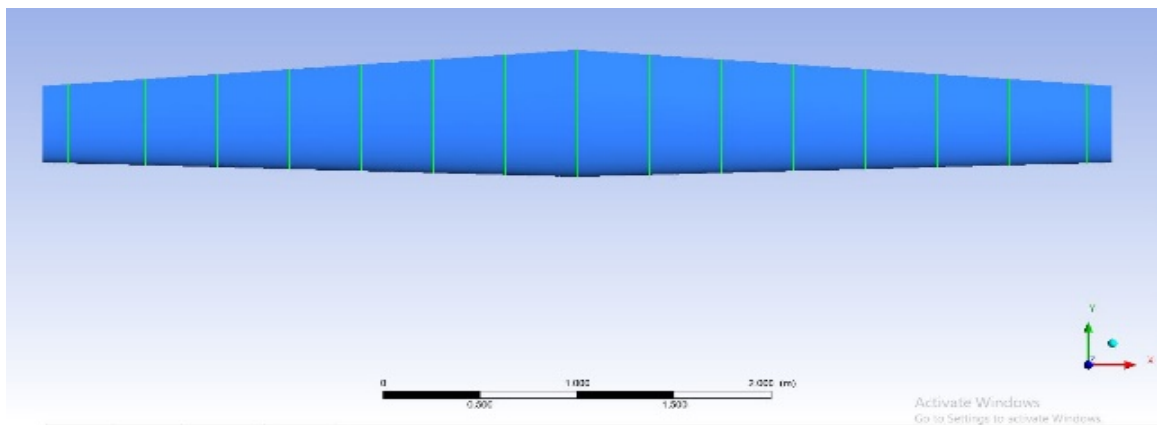
Figure 2-6: The Position of observation of Wing Lift Distribution on the wing

Then the resulting images were analyzed by VLM, Horseshoe Vortex and 3D Panel methods.

2.5 CFD Model

Lift force distribution calculations are performed on the cruise configuration. There are a total of 15 points to be observed based on the need for wiffletree testing. These points can be seen in Table 2-1.

Table 2-1: The position of observation of lift force distribution

No	Position observation
1.	-2.62
2.	-2.22
3.	-1.85
4.	-1.48
5.	-1.11
6.	-0.74
7.	-0.37
8.	0.00
9.	0.37
10.	0.74
11.	1.11
12.	1.48
13.	1.85
14.	2.22
15.	2.62

The position of observation can also be seen in Figure 2-6, where the numbering sequence starts sequentially from left to right. The yellow line in Figure 2-6 is the airfoil-shaped wing intersection where the lift value is calculated

3. Result and Analysis

This simulation is done on cruise configuration. The parameters used in both configurations can be seen in following.

Table 3-1: Parameters Input

Parameter	Symbol	Value
Configuration	-	Cruise
Velocity	v	30 m/s
Air density	ρ	1.09224 kg/m^3
Wing area	S	3.2175 m^2
MAC	-	0.597 m
Span	b	5.5 m

The simulation process using CFD on the cruise configuration the number of mesh used was 4099054 elements. Aerodynamic force analysis which includes lift coefficient, drag coefficient, CL vs CD coefficient and efficiency (L / D) using CFD is shown in Figure 3-1.
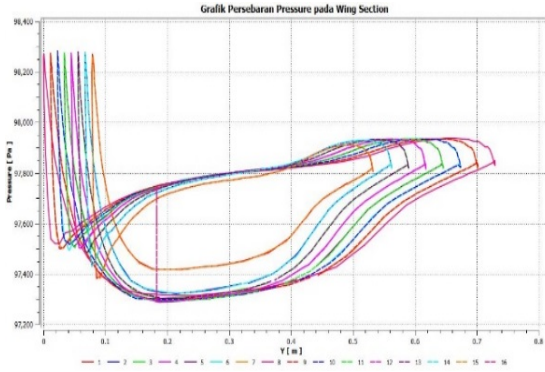
Figure 3-1: Pressure graph vs Y axis in 15 different positions

Figure 3-2: Lift value graph in Wing Position

Can be seen in Figure 3-1 that there are only 8 different graphs. This means that there are two graphs that have the same pressure distribution. The method used in the interp1 command in Matlab is the Spline method. A partition of n = 100 is used. From the calculation results, the lift distribution value obtained at 15 points as in Table 3-2 follows.

Table 3-2: Value of lift respect to position of wing section

Position X (m)	L' (N/m)
-2.62	88.5899
-2.22	139.9946
-1.85	163.1239
-1.48	180.4520
-1.11	195.0827
-0.74	206.7499
-0.37	217.7947
0.00	221.4290
0.37	216.2650
0.74	207.1259
1.11	195.1621
1.48	180.7269
1.85	163.5302
2.22	140.1262
2.62	88.8286

Figure 3-2 bellow displays a lift graph to the position of the wing section.

Based on research conducted by (Choi et al., 2014) and (Fouad, Mahmoud, & Nasr, 2018) the results generated from CFD simulations for the analysis of lift distribution are accurate results. So that it can be used as a reference for comparing LLT, 3D Panel, Horseshoe Vortex and VLM methods

Analysis of aerodynamic forces using VLM and 3D Panels was carried out on 6000 and 12150 panels, respectively. The large number of panels shows increasingly similar to the original wing shape. On the other hand, the large number of panels affects the simulation time.

There are differences of amount in analysis with VLM and 3D Panel. This difference can be seen in Figure 3-1 and 3-2. This is because VLM only analyzes the mean camber line while 3D Panel analyzes many three-dimensional panels on the wing.

Analysis of force distribution with VLM and 3D Panel on XFLR5 software only produces raw data. Then the data is processed into data that represents the distribution of forces along the wing. The results of the data processing are made in graphical form as follows. This shows that VLM is the result of the development of the Horseshoe Vortex method.
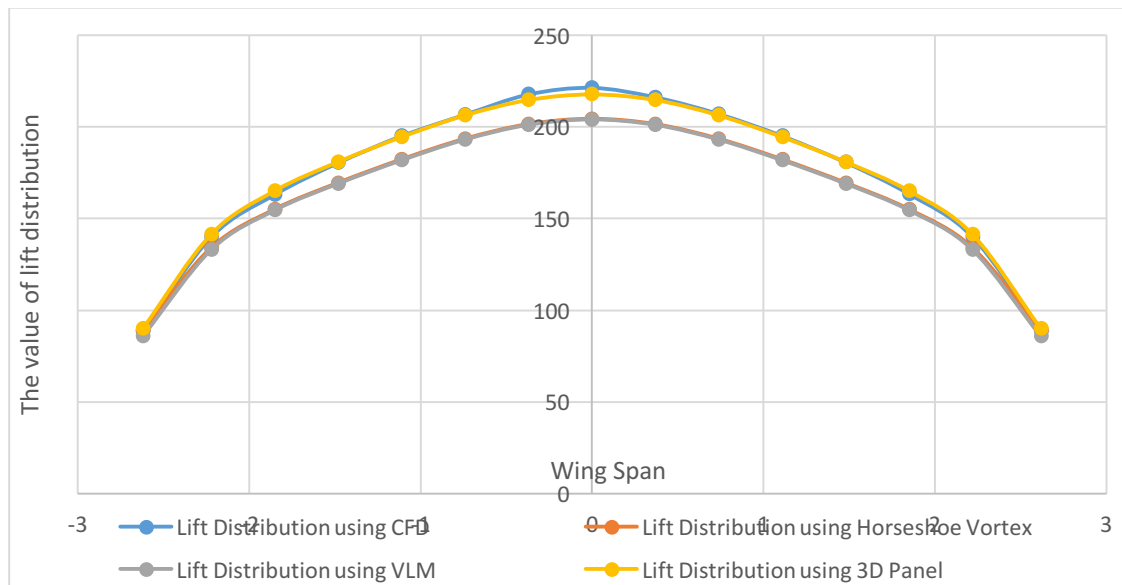
Figure 3-3 : Lift distribution with 4 different methods

However, the comparison of results between VLM and 3D Panel is maximum of 13 N, a large enough difference.

3.1. Comparison Results of VLM, Horseshoe Vortex, 3D Panel and CFD

The analysis results obtained by using CFD, VLM, 3D Panel and Horseshoe Vortex made a comparison of the values of the force distribution at 15 observation points. Comparison of the results of the four methods is presented in Figure 3-3. The distribution of lift values at the observation position at the point mentioned in Table 3-4 shows the difference in lift values at each point not too far away. Based on Figure 3-3 to approach the results of the lift force distribution calculation with CFD is the 3D Panel method. The difference in distribution values at each observation point is very small. As for the VLM and Horseshoe Vortex methods, the difference in lift distribution at each observation point is relatively close to CFD. The biggest difference between CFD and VLM and Horseshoe Vortex lies in the root chord wing. To find out the value at each

point of observation can be seen in Table 3-4.

However, in terms of time to do one simulation with variance of the angle of attack each method is presented in Table 3-3.

Table 3-3: Time required for each method

Method	Time
3D Panel	400 second
VLM	65 second
Horseshoe Vortex	66 second
CFD	1210 second

As already mentioned that the simulation is done on cruise conditions means that it is only simulated when the angle of attack is zero. Based on Table 3-3 it appears that the VLM method is a fast method to do simulations with the time required is 65 seconds. While CFD requires quite a lot of time which is 1210 seconds. For the VLM method, Horseshoe Vortex and 3D Panel can simulate for several angles of attack with a fairly fast time, not much different from simulations for one angle of attack.

Table 3-4: Lift Force Distribution Value with Four Methods at 15 observation points

Observation position	METHOD			
	3D Panel	VLM	Horseshoe Vortex	CFD
-2.62	89.92180075	85.73947843	89.05205992	88.59
-2.22	141.5271871	133.0338307	134.0970227	139.99
-1.85	165.2175825	154.5349692	155.0616294	163.12
-1.48	181.0207952	169.0349681	169.5274925	180.45
-1.11	194.5916861	181.7632156	1822917797	195.08
-0.74	206.4318603	193.0378102	193.5467664	206.75
-0.37	214.812132	201.077463	201.5339771	217.79
0	217.86	204.01	204.44	221.43
0.37	214.8121321	201.077463	201.5339771	217.79
0.74	206.4318604	193.0378102	193.5467665	206.75
1.11	194.5916863	181.7632157	182.2917798	195.08
1.48	181.0207954	169.0349682	169.5274926	180.45
1.85	165.2175828	154.5349694	155.0616295	163.12
2.22	141.5271874	133.033831	134.0970229	139.99
2.62	89.92180115	85.73947906	89.05206017	88.59

Whereas CFD within 1210 seconds is only for one angle of attack. Difference of 810 seconds with the 3D Panel method. The difference in the results of the 3D Panel method analysis with VLM and Horseshoe Vortex is due to the geometry formed using the 3D Panel method which is very similar to the CFD. Therefore the 3D Panel method can analyze the distribution of pressure on the upper and lower surface of the wing.

Referring to Table 3-4, it appears that the difference between the results of the CFD and 3D Panel is not too far away. Only in the root chord the difference is only 4N adrift. With a small enough difference, for the analysis of the lift force distribution on the wing for prediction of static wing testing.

Based on research conducted by (Choi et al., 2014) and (Fouad et al., 2018), that CFD can approach experimental results. Therefore, with a shorter and faster time, to do the analysis of the force distribution on the the aircraft wings is enough to do with the 3D Panel method.

4   Conclusions

In this research, the lift force distribution analysis on the wings of LSU 05-NG has been carried out with four methods namely CFD, VLM, Horseshoe Vortex and 3D Panel. This analysis process begins with making wing geometry with the FX 76-MP 160 airfoil. Then the analysis is carried out based on the results and time required for analysis. Based on the results of research, it was found that VLM as an efficient method in terms of time. However, VLM provides inaccurate results to approach the CFD. The 3D Panel method takes 400 seconds, giving very good results to approach the analysis results of the lift force distribution with CFD. With a relatively fast time, 3D Panel is an effective and efficient method to approach the analysis results with CFD.

Contributorship Statements

AS analyzed the result and developed the VLM, Horseshoe Vortex and 3D Panel Method simulations; KH designed CFD simulations method, AR and YGW prepared the manuscript

References

Anderson Jr, J. (2001). Fundamentals of Aerodynamics. In *Fundamentals of aerodynamics*. https://doi.org/10.1036/00723733 50

Bertin, J. J., & Cummings, R. M. (2009). *Aerodynamics for Engineers* (5th ed.). New Jersey: Pearson Prentice-Hall.

Budziak, K. (2015). *Aerodynamic Analysis with Athena Vortex Lattice.* 1–72.

Buzdiak, K. (2015). *Aerodynamic Analysis with Athena Vortex Lattice (AVL).* Hamburg: Hamburg University of Applied Sciences.

Carvalho, A. R. D., & Brito, P. P. de C. (2017). Nonlinear Lifting Line Implementation and Validation for Aerodynamic and Stability Analysis. *The XXXVIII Iberian Latin-American Congress on Computational Methods in Engineering.* Florianpolis.

Choi, C., Yu, W., & Kwon, D. (2014). *Comparison Between the CFD and Wind Tunnel Experiment for Tall Building with Various Corner Shapes Comparison between the CFD and Wind Tunnel Experiment for Tall Building with Various Corner Shapes.* (May).

Deperrois, A. (2013). XFLR5 Analysis of foils and wings operating at low Reynolds numbers. *Date Accessed: 12.01.2016.* https://doi.org/10.1007/978-1-62703-788-4

Fonseca, W. D. P., Pinheiro, E. M., &

Arcos, I. S. V. (2018). Aerodynamics Investigation of Finite Wings by Lifting-line Models using the Track Method. *Congresso Tecnico Cientifico Da Engenharia e Da Agronomia - CONTECC'2018.* Maceio.

Fouad, N. S., Mahmoud, G. H., & Nasr, N. E. (2018). Comparative study of international codes wind loads and CFD results for low rise buildings. *Alexandria Engineering Journal, 57*(4), 3623–3639. https://doi.org/10.1016/j.aej.2017.11.023

Gryte, K., Hann, R., Alam, M., Rohac, J., Johansen, T. A., & Fossen, T. I. (2018). Aerodynamic Modeling of the Skywalker X8 Fixed-Wing Unmanned Aerial Vehicle. *2018 International Conference on Unmanned Aircraft Systems, ICUAS 2018.* https://doi.org/10.1109/ICUAS.2018.8453370

Küchemann, D. (1953). The Distribution of Lift over the Surface of Swept Wings. *Aeronautical Quarterly, 4*(3), 261–278. https://doi.org/10.1017/S0001925900000937

Loya, A., Maqsood, K., & Muhammad Duraid. (2018). Quantification of Aerodynamic Variables using Analytical Technique and Computational Fluid Dynamics. *International Journal of Mechanical and Mechatronics Engineering, 12*(10), 991–997.

Melin, T. (2000). A vortex lattice MATLAB implementation for linear aerodynamic wing applications. *Master Thesis*, (Master Thesis). https://doi.org/10.13140/RG.2.2.24472.49923

Multhopp, H. (1955). *Methods for Calculating the Lift Distribution of Wings (Subsonic Lifting-Surface*

Theory).

Panagiotou, P., Kaparos, P., Salpingidou, C., & Yakinthos, K. (2016). Aerodynamic design of a MALE UAV. *Aerospace Science and Technology.* https://doi.org/10.1016/j.ast.2015.12.033

Silitonga, F. Y., & Moelyadi, M. A. (2018). Comparative Study of Wing Lift Distribution Analysis for High Altitude Long Endurance (HALE) Unmaned Aerial Vehicle. *Journal of Physics: Conference Series*, *1005*(1). https://doi.org/10.1088/1742-6596/1005/1/012036

Sivells, J. C., & Neelly, R. H. (1947). *Method for Calculating Wing Characteristics by Lifting-line Theory using Nonlinear Section Lift Data.*

Spall, R. E., Phillips, W. F., & Pincock, B. B. (2012). Comparison of Inviscid Flow Methods for Lift and Drag Calculations Over Thin-Sail Geometries. *Volume 1: Symposia, Parts A and B*, 1235. https://doi.org/10.1115/FEDSM2012-72045

Ugargol, R. B., & Ugargol, A. B. (2017). Design and Analysis of Winglet for Low Subsonic Speeds. *International Journal of Advances in Scientific Research and Engineering*, *3*(1), 1–6.

Weber, J., Kirby, D. A., & Kettle, D. J. (1956). *An Extension of Multhopp's Method of Calculating the Spanwise Loading of Wing-Fuselage Combinations.*

DEPARTURE TRAJECTORY OPTIMIZATION FOR NOISE ABATEMENT PROCEDURE IN SOEKARNO-HATTA INTERNATIONAL AIRPORT

Vincentius N.S. Suryo[1], Benedikt Grüter[2], Johannes Diepolder[3], Neno Ruseno[4], and Florian Holzapfel[5]

[1,4]Aviation Engineering Department, International University Liaison Indonesia

[1,2,3,5]Institute of Flight System Dynamics, Technische Universität München

[4]E-mail: neno.ruseno@iuli.ac.id

ABSTRACT

Air traffic noise emission has been a growing concern for communities living within the vicinity of airports due to a massive increase in air traffic volume in recent years. This work focuses on the noise annoyance problem by optimizing one of the RNAV trajectories, which aims to minimize the noise footprint of a flying aircraft in a low altitude trajectory. Optimal control theory is applied to minimize the number of awakenings caused by a departing aircraft while constraining the relative increase of fuel consumption with regard to a fuel-minimal trajectory. The aircraft simulation model is based on the BADA 3 database, while the noise is modeled according to the ANP database, both published by EUROCONTROL. The methodology is demonstrated for the Soekarno-Hatta International Airport (CGK) in Jakarta; the result shows the comparison between fuel-minimal trajectories and noise-minimal trajectories for seven aircraft types representing the fleet mix at CGK. The number of awakenings of the noise-minimal trajectories is reduced by 30.33%, with an additional of 5% fuel consumption for the seven aircraft types when compared to the fuel-minimal trajectory.

1 Introduction

Due to the continuous growth of air traffic, noise annoyance has become an increasing concern, especially in the vicinity of airports. Despite many advancements in technology to significantly reduce noise emissions, the level of noise disturbances has remained unchanged or even increased due to the increase in the number of movements (landing or takeoff). Research from the Aviation Environment Federation (AEF) has shown that extensive exposure to noise can cause health problems such as cardiovascular diseases, sleep disturbance and is even has an impact of learning on children (AEF, 2016).

This work focuses on the Noise Abatement Procedures (NAP), which manipulate flight paths of an aircraft, whether in the lateral flight path or vertical flight path. The procedure applied to the Soekarno-Hatta International Airport (CGK) using one of the Standard Instrument Departure (SID) procedures waypoints existing in the airport.

For this case study, fuel and noise optimal trajectories are obtained by applying Optimal Control Theory (OCT). OCT has been used previously in the context of noise abatement by Xavier Prats (Prats, et al., 2010) to optimize noise for the Girona Airport in Spain.

Similar works are the developments of advanced operational procedures framework to analyze noise impacts by Thomas (Thomas & Hansman, 2019), strategy to design NAP by implementing nonlinear multi-objective optimal control problem by Prats (Prats, et al., 2010), performance bounding of continuous descent arrival procedures in terms of operating costs by Park (Park & Clarke, 2015), optimization tool for departure noise abatement procedure by using reference flight path by Wijnen (Wijnen & Visser, 2003), design of aircraft terminal routes for noise abatement by employing a multi-objective evolutionary algorithm based on decomposition by Ho-Huu (Ho-Huu, et al., 2018), and determination of noise-minimal departure trajectories by Richter (Richter, et al., 2014). This paper extends previous work applicability, where it uses similar methodologies to be applied for one airport, contributing to noise emission reduction.

2 Methodology

The research focuses on applying OCT for a CGK SID departure trajectory. The following subsections present the Optimal Control Problem (OCP) formulation, the noise disturbance cost function, the scenario definition, and the aircraft simulation model.

2.1. Optimal Control Theory

The OCP is formulated as a Bolza-type objective function J consisting both of the Mayer Term (θ) and Lagrange Term $(\mathcal{L})$. The Bolza-type problem is formulated as follows (Prats, et al., 2006):

$$\min \quad J = \theta\left(\boldsymbol{x}(t_0), \boldsymbol{x}(t_f)\right) + \int_{t_0}^{t_f} \mathcal{L}(\boldsymbol{x}, \boldsymbol{u})dt \qquad (2\text{-}1)$$

subject to:

Dynamic Constraints

$$\dot{\boldsymbol{x}} = f(\boldsymbol{x}, \boldsymbol{u}) \qquad (2\text{-}2)$$

Event Constraints

$$\phi_{min} \leq \phi\left(\boldsymbol{x}(t_0), t_0, \boldsymbol{x}(t_f)\right) \leq \phi_{max} \qquad (2\text{-}3)$$

Path Constraints

$$\boldsymbol{h}_{min} \leq \boldsymbol{h}(\boldsymbol{x}, \boldsymbol{u}) \leq \boldsymbol{h}_{max} \qquad (2\text{-}4)$$

where $\boldsymbol{x}(t) \in \mathbb{R}^m$ is the state vector, $\boldsymbol{u}(t) \in \mathbb{R}^n$ is the control vector, t_0 is the initial time, and t_f is the final time, which is set to be free. The fuel-minimum trajectories problem is formulated as a Mayer-type problem with:

$$\theta\left(\boldsymbol{x}(t_0), \boldsymbol{x}(t_f)\right) = -m(t_f) \qquad (2\text{-}5)$$

where $m(t_f)$ is the mass of the aircraft at the end of the optimization. While the noise-minimum trajectory is formulated as Lagrange-type problem with:

$$\int_{t_0}^{t_f} \mathcal{L}(\boldsymbol{x}, \boldsymbol{u})dt = N_{awak} \qquad (2\text{-}6)$$

where N_{awak} is the number of awakenings, to be explained in subsection 2.2. The optimization process uses a combined objective function consisting of fuel and noise. Therefore, the resulting trajectory should converge to a point where neither objective can be improved without worsening the other, better known as Pareto optimality condition (Chatterjee, 2011). The epsilon-constraint $(\epsilon-constraint)$ method is chosen to obtain points fulfilling the Pareto optimality condition, based on (Haimes, et al., 1971), where:

Problem A $\quad\quad \min\left[-m(t_f), N_{awak}\right]$

subject to $\quad\quad g(x,u) \leq 0$

is replaced by

Problem B (ϵ) $\quad \min N_{awak}$

subject to $\quad\quad \Delta r_{fuel} \leq \epsilon$

$\quad\quad\quad\quad\quad\quad g(x,u) \leq 0$

where $g(x,u) \leq 0$ collects all constraints of the optimal control problem and Δr_{fuel} represents the relative additional fuel consumption, computed in subsection 2.2. Applying this method, we can choose any value of ϵ to be employed as an additional constraint for fuel consumption when solving the noise minimization problem, explained in subsection 2.2.

The method chosen to solve the Bolza problem is the trapezoidal collocation method. The trapezoidal collocation works by converting a continuous-time OCP into a nonlinear program using trapezoidal quadrature to replace the continuous solution to the differential equation by a discrete approximation (Kelly, 2017). Furthermore, the optimal control toolbox called FALCON.m was used in this study (Rieck, et al., n.d.).

2.2. Objective Function

The Sound Exposure Level (SEL) objective function must be defined before the scenario definition. The research conducted by Figlar (Miller & Gardner, 2008) yields a differentiable model for the sound pressure level L_A:

$$L_A = c_0 + c_1 T_{corr} + c_2 \log(d) + c_3 \log(d)^2 \quad (2\text{-}7)$$

The coefficients c_0, c_1, c_2 and c_3 are specific to the aircraft type and can be estimated using the Aircraft Noise and Performance (ANP) database published

by EUROCONTROL (EUROCONTROL, 2020). T_{corr} is the corrected net thrust of the engine, and d is the distance between a noise receiver and an aircraft. The sound pressure level is integrated over the period in which the aircraft travels to the specific location yielding SEL:

$$SEL = \int_{t_0}^{t_f} 10^{0.1 \cdot L_A(t)} \, dt \quad (2\text{-}8)$$

The resulting SEL is used to estimate the expected probability of a person awakening due to noise exposure (P_{awak}) in a particular location, which can be calculated by using the ANSI Curve Sleep Standard for single events (Miller & Gardner, 2008):

$$P_{awak} = \frac{1}{1+e^{-z}} \quad (2\text{-}9)$$

Where

$$Z = \beta_0 + \beta_L \cdot SEL + \beta_T \cdot T_{retire} + \beta_S \cdot S_{sensitivity} \quad (2\text{-}10)$$

And

$\beta_0, \beta_L, \beta_T, \beta_S$ = constant
T_{retire} = Time since retiring, minutes
$S_{sensitivity}$ = Sensitivity for population segment

For this case study, the percentage of awakenings is computed as a function of SEL only, therefore, T_{retire} and $S_{sensitivity}$ is assumed to be zero. In this case, the constants value of β_0 and β_L are -6.8884 and 0.0444, respectively. Further explanation can be found in (Miller & Gardner, 2008). The resulting P_{awak} are used to calculate the number of awakenings (N_{awak}) in each location by multiplying the value with the number of inhabitants $w_{R,i}$:

$$N_{awak} = \sum_{i=1}^{n} P_{awak,i} \cdot w_{R,i} \quad (2\text{-}11)$$

where the index i represents the number of each receiver, and n is the total number of receivers. The other objective function to be optimized is the final mass of the aircraft $m(t_f)$. We want to maximize $m(t_f)$ so that the fuel consumption defined by the difference between initial and final mass is minimized. As explained in subsection 2.1, the epsilon-constraint method is employed to restrict the relative additional fuel consumption when minimizing noise. The epsilon-constraint value can be determined by:

$$\Delta r_{fuel} = \frac{m(t_0)-m(t_f)}{m(t_0)-m^*(t_f)} - 1 \leq \epsilon \qquad (2\text{-}12)$$

where the nominator represents the noise-minimal trajectory's fuel consumption, and the denominator represents the fuel-minimal trajectory's fuel consumption. This work uses different values of ϵ: 0.0, 0.025, 0.05, and 0.075, to determine the trend of the number of awakenings N_{awak} in correspondence with different relative additional fuel consumption.

2.3. Aircraft Model Description

This subsection discusses the aircraft types chosen for this research as well as the reason behind the decision. There are seven types of aircraft which is considered in the optimization, consisting of four narrow-body jet airliner B737-800NG (B738), B737-500CL (B735), B737-900NG (B739), A320-200 (A320), two wide-body jet airliner A330-200 (A332) and B777-300 (B773), and one regional jet CRJ-900 (CRJ9). According to the Blue Swan daily (The Blue Swan Daily, 2018), the seven types are the most frequent aircraft types flying into and out of the Soekarno-Hatta International Airport, making up over 90% of movements at

the airport in domestic and international flights, which is shown in Figure 2-1.
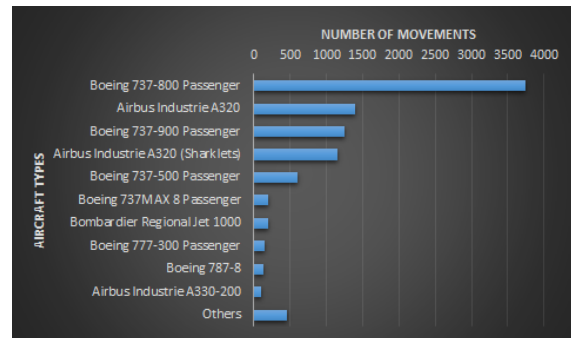
Figure 2-1: Aircraft Movement in CGK in 2018 (The Blue Swan Daily, 2018)

The aircraft model is built according to the Base of Aircraft Data Family 3 (BADA3) published by EUROCONTROL (Nuic, et al., 2010). Its performance characteristics are taken from the Aircraft Performance Database (APD), also published by EUROCONTROL (EUROCONTROL Experimental Centre, n.d.).

2.4. Scenario Definition

The southeast bound departure procedure of runway 25R is the basis of the optimization scenario in this research. Figure 2-2 shows the CA1D Standard Instrument Departure (SID) procedure. The procedure has an initial climb on the runway heading up to 8,000 feet and turns right directly to waypoint NABIL after reaching 500 feet upon lift-off. From this point, the aircraft turns right after NABIL to 113-degree radial heading towards NANTO, maintaining its altitude at 8,000 feet. It continues this heading until 'CA' NDB while climbing continuously up to 18,000 feet at MUTIA and 24,000 feet at 'CA' NDB (Jeppesen Sanderson Inc., 2018).
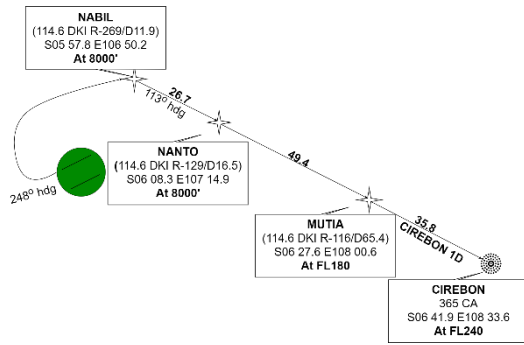
Figure 2-2: CA1D SID Departure
(Jeppesen Sanderson Inc.,
2018)

The Optimization process in the departure trajectory is focusing on the initial climb starting from the runway threshold when the aircraft takeoff at the speed of v_2, until the waypoint NABIL at 8,000 feet or 2,440 m high from the sea level. The reason behind this scenario is because, after the waypoint NABIL in CA1D SID, the aircraft has reached a sufficient altitude that the noise produced has little effect on the populated area below it. The origin point of this scenario is the threshold of runway 25R, and subsequently, all the reference positions of populated areas, as well as the position of NABIL waypoint, are measured relative to this origin point. The coordinates of runway 25R and waypoint NABIL, NANTO, MUTIA, and CA NDB are given in Table 2-1.

We compute the relative distance of each waypoint to the runway 25R by using the geodetic conversion formula in the North-East-Down (NED) frame. The relative distance of the last waypoint is to be used as the final boundary condition of the departure trajectory, which in this case, is NABIL waypoint.

The locations which are considered as receivers are the western, central, and eastern parts of the city of Jakarta, Cengkareng region, and some parts of South Tangerang City. These areas are located within 20 kilometers of CGK, where aircraft flies below 8,000 feet with almost full thrust power, resulting in very high noise in the area. The location area is shown in Figure 2-3.

Table 2-1: Waypoints Coordinates
(Directorate General of Civil
Aviation Indonesia, 2019)

Waypoints	Latitude	Longitude
RWY 25R	[S06 06 32.27]	[E106 40 08.62]
NABIL	[S05 57 47.96]	[E106 50 13.48]
NANTO	[S06 08 17.14]	[E107 14 54.04]
MUTIA	[S06 27 34.25]	[E108 00 33.53]
CA NDB	[S06 41 52.73]	[E108 33 35.13]

Figure 2-3: Receivers for Noise
Abatement
(Source: Google Earth,
©2020 Google, ©2020
Maxar Technologies)

The receivers' location is gridded per kilometer-square, and each kilometer-square is filled with a particular population number which is extracted from the "Gridded Population of the World (GPW), v4" published by the Socioeconomic Data and Applications Center (SEDAC) at Columbia University (Columbia University, n.d.). The latitude and longitude limits of the receivers' area are shown in Table 2-2.

Table 2-2: Latitude and Longitude for
the Receiver's Area Limit.

Limit Position	Latitude Limit [D M S]	Longitude Limit [D M S]
Lower Left	[S06 13 05.88]	[E106 30 24.84]
Lower Right	[S06 13 05.88]	[E106 54 12.96]
Upper Left	[S05 51 48.24]	[E106 30 24.84]
Upper Right	[S05 51 48.24]	[E106 54 12.96]

The resulting gridded populated area with its population number is shown in Figure 2-4, where the color map represents the population density in one kilometer-square area.
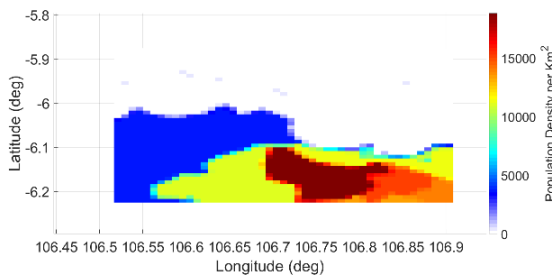
Figure 2-4: Population Area Density

2.5. Problem Formulation

The dynamic model and problem formulation are discussed in this subsection. There are eight states and three control variables within the problem. Writing the states and controls in vector form yield:

$$x = \begin{bmatrix} n \\ e \\ d \\ v \\ \chi \\ \gamma \\ \delta_T \\ m \end{bmatrix} \qquad (2\text{-}13)$$

$$u = \begin{bmatrix} \alpha \\ \delta_{T,cmd} \\ \mu \end{bmatrix} \qquad (2\text{-}14)$$

The first three states, $n, e,$ and d are the 3D spatial representation of the aircraft in the NED-frame, v is the absolute velocity, χ is the course angle, γ is the climb angle, δ_T is the thrust lever position, $\delta_{T,cmd}$ is the commanded thrust lever position, m is the mass of the aircraft, α is the angle of attack, and μ is the bank angle. Then, we introduce the output of this model as:

$$Y = \begin{bmatrix} n_z \\ h \\ h_{dot} \\ T \end{bmatrix} \qquad (2\text{-}15)$$

where n_z is the load factor in the z-direction of the body frame, h is the aircraft's height above the reference ellipsoid, h_{dot} is the kinematic vertical speed corresponding to h, and T is the absolute thrust value in which the value is dependent on the aircraft types. The dynamic equations governing the evolution of the states are:

$$\begin{bmatrix} \dot{n} \\ \dot{e} \\ \dot{d} \end{bmatrix}_O^E = \mathcal{R}_{OK} \cdot \begin{bmatrix} v \\ 0 \\ 0 \end{bmatrix}_K \qquad (2\text{-}16)$$

$$\begin{bmatrix} \dot{v} \\ \dot{\chi} \\ \dot{\gamma} \end{bmatrix} = \begin{bmatrix} 1 & 0 & 0 \\ 0 & \frac{1}{v \cdot \cos(\gamma)} & 0 \\ 0 & 0 & -\frac{1}{v} \end{bmatrix} \cdot \frac{1}{m} \sum(F)_K \quad (2\text{-}17)$$

$$\dot{\delta_T} = \frac{1}{T_T} \cdot (\delta_{T,cmd} - \delta_T) \qquad (2\text{-}18)$$

$$\dot{m} = -\dot{m}_f \cdot (F_P, h, v, \rho) \qquad (2\text{-}19)$$

In which $\mathcal{R}_{OK}$ is the coordinate transformation matrix from kinematic frame to NED frame, h is the altitude, ρ is the Atmospheric air density based on the International Standard Atmosphere

(ISA), and $\sum(\boldsymbol{F})_K$ is the summation of forces in the kinematic frame given by (Gerdts & Grüter, 2019):

$$\sum(\boldsymbol{F})_K = \mathcal{R}_{KO}\mathcal{R}_{OA}(\boldsymbol{F_A})_A + \mathcal{R}_{KB}(\boldsymbol{F_P})_B + \mathcal{R}_{KB}(\boldsymbol{F_P})_B + \quad (2\text{-}20)$$
$$\mathcal{R}_{KO}(\boldsymbol{F_G})_O$$

In which $\mathcal{R}_{KO}$ is the coordinate transformation from NED frame to kinematic frame, $\mathcal{R}_{OA}$ is the coordinate transformation matrix from aerodynamic frame to NED frame, and $\mathcal{R}_{KB}$ is the coordinate transformation matrix from the body frame to the kinematic frame. The force vector $\boldsymbol{F_A}, \boldsymbol{F_P}, \boldsymbol{F_G}$ stands for aerodynamic, propulsion, and gravitation force, respectively, and are given by:

$$\boldsymbol{F_A} = \begin{bmatrix} -D \\ 0 \\ -L \end{bmatrix}_A \quad (2\text{-}21)$$

$$\boldsymbol{F_P} = \begin{bmatrix} T \\ 0 \\ 0 \end{bmatrix}_B \quad (2\text{-}22)$$

$$\boldsymbol{F_G} = \begin{bmatrix} 0 \\ 0 \\ m \cdot g \end{bmatrix}_O \quad (2\text{-}23)$$

In which D is the drag force, L is the lift force, T is the thrust output, m is mass of the aircraft, and g is Earth's gravitational acceleration.

3. Results

The result compares the fuel minimization trajectories for all aircraft types (trajectory 1) with the fuel/noise optimization trajectories for all aircraft types included in this research (trajectory 2). Trajectory 1 uses the aircraft's mass as its objective to be maximized, and the resulting minimum fuel consumption is used for fuel consumption benchmark in trajectory 2. On the other hand, trajectory 2 uses the number of awakenings as its objective to

be minimized, and the epsilon constraint is applied to restrict the additional fuel consumption. The values chosen for the epsilon constraint are 0.025 (2.5%), 0.05 (5%), and 0.075 (7.5%) additional fuel to see the impact of fuel to the number of awakenings.

In general, trajectories 1 follow RNAV guidelines where after takeoff, the aircraft takes a right turn immediately and flies straight towards NABIL. Also, all aircraft types take similar fuel minimal trajectories except for CRJ9 and B773, which exhibit larger radii. On the other hand, trajectories 2 display a different approach towards NABIL. After takeoff, they avoid the densely populated areas first before flying towards NABIL, resulting in larger turning radii for all aircraft types. The resulting trajectories are shown in Figure 3-1, where the solid lines represent trajectories 1, the dotted lines represent trajectories 2 with 5% additional fuel, and the gridded population area is shown as a contour plot with its population density as the color map.

Figure 3-2 summarizes the parameters and objective function values for both trajectories, in which a similar pattern of increasing time and fuel noise while the decreasing number of awakenings can be found for all aircraft types. Principally, the time to fly trajectories 1 is about 252 seconds on average, while it took 291 seconds to fly trajectories 2 for the seven aircraft types. Additionally, all aircrafts' fuel consumption in trajectory 2 fulfilled the requirement of the epsilon-constraint. Figure 3-2 also shows the parameter of trajectory 2 when using 2.5% and 7.5% additional fuel restriction.

Looking into each aircraft class type, the narrow-body jets, A320, B735, B738, and B739 yield similar parameters in terms of time taken to fly both

trajectories. The four aircraft types result in 235 seconds for minimum fuel trajectory, 245 seconds for 2.5% additional fuel, 257 seconds for 5.0% additional fuel, and 271 seconds for 7.5% additional fuel. For the four aircraft types, every 2.5% additional fuel result in 5% relative additional time on average.

In terms of fuel consumption, the narrow-body airliners also have similar minimum fuel consumption. The minimum fuel consumption values are 386 kg for A320, 416 kg for B735, and 422 kg for both B738 and B739. The fuel consumption rises according to the epsilon constraint value.

In terms of noise exposure, however, the four types show different values compared to each other. For the minimum fuel trajectory, the average number of awakenings varies from 136 (A320) to 278 people (B739), while B735 and B738 yield 152 and 244 number of awakenings, respectively. Compared to the fuel-minimal trajectory, the four types have a significant reduction in terms of the number of awakenings. With 2.5% additional fuel, the number of awakenings for the four types reduces by 32.8% on average, 36.4% for 5% additional fuel, and 38.6% for 7.5% additional fuel. The B739, in particular, has the highest reduction regarding the number of awakenings among the narrow-body airliner aircraft types, reaching nearly 50% reduction for 5% additional fuel consumed compared to the number of awakenings in minimum fuel trajectory.

The two wide-body airliner types, the A332 and B773, exhibit similar patterns in their trajectories. In terms of time taken, the A332 takes 237 seconds for the fuel-minimal trajectory, and B773 takes 310 seconds for the same trajectory. When solving for noise and the epsilon constraint is applied, both types have an increase of flying time at about 4.7% for every 2.5% relative additional fuel is consumed. The trajectory 1 fuel consumption for A332 and B773 is 1106 and 1663 kg, respectively, and it changes according to the fuel restriction for trajectory 2.

The number of awakenings for the wide-body airliner is fairly surprising. The number of awakenings in the fuel-minimal trajectory for A332 is 201 people. This value is lower than that which is seen for B738 and B739. The B773 also has a lower number of awakenings value, 163 people, than the narrow airliner types due to a larger turn radius in its fuel-minimal trajectory, which in turn flying above a sparsely populated area. As a result, the reductions for the wide-body aircraft types are not as significant as those for the narrow-body airliners. The number of awakenings' reduction for A332 are 23.4%, 28.4%, and 30.9% for 2.5%, 5%, and 7.5% additional fuel, respectively. For B773, the reduction is lesser, yielding only 1.2%, 2.5%, and 3.7%, respectively, for the same additional fuel consumption.

The last aircraft type, CRJ9, has some unusual parameters. The flying time increases by 15% for every 2.5% increment of additional fuel consumption. This increase is more significant when compared to other aircraft types. The baseline fuel consumption for CRJ9 is 150 kg and increases accordingly to the epsilon constraint. For the fuel-minimal trajectory, CRJ9 has the number of awakenings value of 93 people. This value diminishes to 52, 49, and 49 people for 2.5%, 5%, and 7.5% additional fuel, a reduction worth of 46.2% on average for the type.

In summary, with 5.0% relative additional fuel, all aircraft types shows a reduction of the number of awakenings as follows: 25.74% for A320, 28.36% for A332, 23.03% for B735, 36.89% for B738, 48.56% for B739, 2.45% for B773, and 47.31% for CRJ9. These values result in an averagely 30.33% number of awakenings reduction for the seven aircraft types.
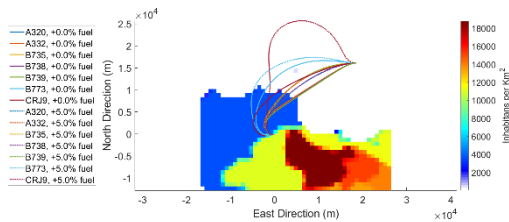
Figure 3-1:Different Aircraft Types Trajectory for Fuel/Noise Optimization
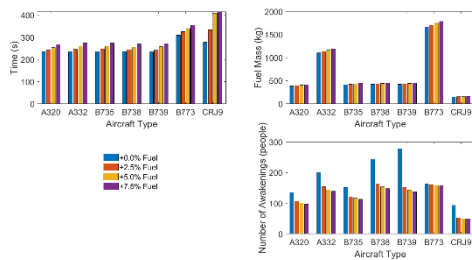
Figure 3-2:Trajectory Data for different Aircraft Types (Top-Left: Time Parameter, Top-Right: Fuel Consumption, Bottom-Right: Number of Awakenings)

The B739's noise footprint is discussed in detail since it produces the highest noise exposure among the seven aircraft types, whereas all noise footprints of the other aircraft types are provided in appendix A. Figure 3-3 shows the noise footprint in terms of SEL for the B739 aircraft. The top picture is the SEL footprint of the fuel-minimal trajectory (trajectory 1), and the bottom picture is for the noise-minimal trajectory (trajectory 2) with 5.0% additional fuel consumption. The most significant exposure happens at the start

of the trajectory where the aircraft applies its full thrust, and due to its low altitude, the noise exposure level reaches its highest at about 130 dB in this area. As the aircraft climbs and reduces its thrust output progressively, the SEL reduces in the greater area accordingly. Trajectory 2, in turn, trades off noise levels with fuel consumption. the second part of Figure 3-3 shows the highest noise levels when using an additional 5.0% fuel consumption yields about 100 dB at the start of the trajectory instead of 130 dB. This result then affects the overall noise levels on the trajectory, which is lower than that in trajectory 2.
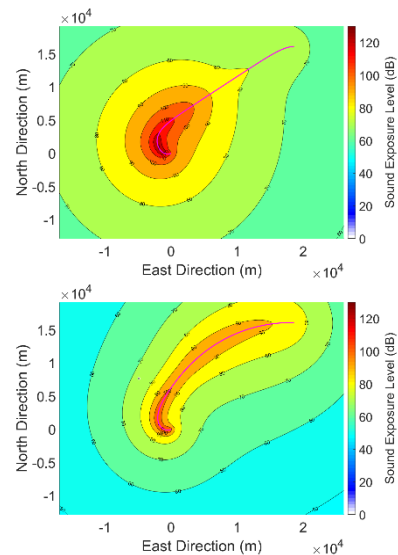
Figure 3-3:Sound Exposure Level Footprint for B739 (Top: +0.0% Fuel-minimal Trajectory, Bottom: +5.0% fuel Noise-minimal Trajectory)

The number of awakenings (Figure 3-4) due to a departing B739 is profoundly affected by the population density in the area (Figure 2-4) and the sound exposure level (Figure 3-3). For trajectory 1, even when the southeast area gets exposed to a similar level of noise, it yields in a higher number of awakenings than the northwest area due

to its high-density inhabitants, with the highest number yields as high as 1,200 people. Trajectory 2 then avoided these high-density areas as much as possible, resulting in lower noise and awakenings percentage to the area. Hence, the same area which previously had between 1,000 and 1,200people awakened now is reduced to about 400 to 800 people.
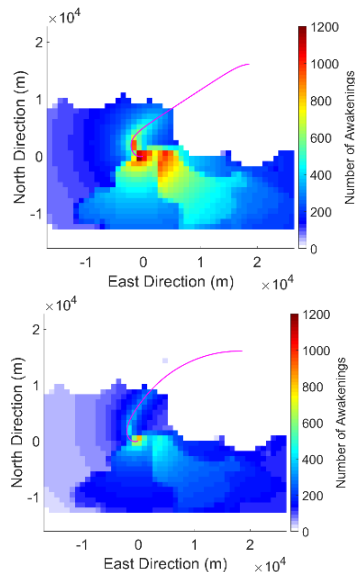
Figure 3-4:Number of Awakenings Footprint for B739 (Top: +0.0% Fuel-minimal Trajectory, Bottom: +5.0% fuel Noise-minimal Trajectory)

4   Conclusions

OCT has been successfully applied to generate noise-optimized trajectories on the airport, in which the resulting trajectories have been discussed in detail. The results regarding the departure trajectories indicate a potential reduction of the average number of awakenings by 30.33% for 5% additional fuel consumption in the seven aircraft types, benefitting the environments by reducing noise emissions. It is important to note that although the research methodology is applied for the Soekarno-Hatta International Airport in Jakarta

geographically, the research method can be applied in any airport. Furthermore, the algorithm used in this research can also be applied to any aircraft types, making it a generic algorithm that can be adapted in any airport and aircraft. Therefore, the methodology of the research can be used for a tool to plan SIDs in airports worldwide.

The research results in new noise-minimization trajectories for one RNAV procedure in the departure scenario. It would be interesting to see other RNAV procedures of this airport go through the same process of noise optimization to see a significant reduction in noise emission. Also, the scope of this work is applied for one aircraft at a time. It is intriguing to see multiple aircrafts operation and see the resulting noise footprints for the area below it. Nevertheless, the application of OCT to minimize noise by generating new trajectories contributes to a further sustainable aircraft operation in terms of noise exposure.

Contributorship Statements

Vincentius N.S. Suryo (VS) is the main contributor of this manuscript. VS made the research concept and planning as well as finding references and solving the research problem. Benedikt Grüter (BG) and Johannes Diepolder (JD) provided the tool to conduct the research as well as compiling the

necessary data required to the research. Neno Ruseno (NR) helped with the verification and validation of the research results as an internal reviewer. Lastly, Florian Holzapfel (FH) provided the research group with authorization and final approval for the manuscript to be published.

References

AEF, (2016). Aircraft Noise and Public Health: The Evidence is Loud and Clear.[Online] Available at: https://www.aef.org.uk/uploads/Aircraft-Noise-and-Public-Health-the-evidence-is-loud-and-clear-final-reportONLINE.pdf
[Accessed 21 August 2019].

Chatterjee, D. K., (2011). Encyclopedia of Global Justice. Dordrecht: Springer Netherlands. DOI: 10.1007/978-1-4020-9160-5.

Columbia University, n.d. Gridded Population of the World (GPW), v4 | SEDAC.[Online] Available at: https://sedac.ciesin.columbia.edu/data/collection/gpw-v4
[Accessed 6 March 2020].

Directorate General of Civil Aviation Indonesia, 2019. AIP Indonesia (VOL II) WIII AMDT 76. [Online] Available at: https://aimindonesia.dephub.go.id/index.php?page=product-aip-electronik-vol123.html&id_aip=119
[Accessed 18 September 2019].

EUROCONTROL Experimental Centre, n.d. Aircraft Performance Database. [Online] Available at: https://contentzone.eurocontrol.int/aircraftperformance/default.aspx?
[Accessed 12 February 2020].

EUROCONTROL, (2020). ANP - Eurocontrol Experimental Centre. [Online] Available at: https://www.aircraftnoisemodel.org/[Accessed 12 September 2019].

Gerdts, M. & Grüter, B., (2019). Aircraft Trajectory Optimization, München: Lehrstuhl für Flugsystemdynamik.

Haimes, Y. Y., Lasdon, L. S. & Wismer, D. A., 1971. On a Bicriterion Formulation of the Problems of Integrated System Identification and System Optimization. IEEE Transactions on Systems, Man, and Cybernetics, SMC-1(3), pp. 296 - 297.DOI: 10.1109/TSMC.1971.4308298.

Ho-Huu, V. et al., (2018). Optimization of noise abatement aircraft terminal routes using a multi-objective evolutionary algorithm based on decomposition. Transportation Research Procedia, Volume 29, pp. 157-168.DOI: 10.1016/j.trpro.2018.02.014.

Jeppesen Sanderson Inc., (2018). Airport Information for WIII, Englewood: s.n.

Kelly, M., (2017). An Introduction to Trajectory Optimization: How to Do Your Own Direct Collocation. Society for Industrial and Applied Mathematics (SIAM) Review, 59(4), pp.849-904.DOI: 10.1137/16M1062569.

Miller, N. P. & Gardner, C. R., (2008). How Many people will be awakened by Night time Aircraft Noise?. Foxwoods, 9th International Congress on Noise as a Public Health Problem (ICBEN), pp. 1 - 8..

Nuic, A., Poles, D. & Mouillet, V., (2010). BADA: An advanced aircraft performance model for present and future ATM systems. International Journal of Adaptive Control and Signal Processing, 24(10), p. 850–866. DOI: 10.1002/acs.1176.

Park, S. G. & Clarke, J.-P., (2015). Optimal Control Based Vertical Trajectory Determination for Continuous Descent Arrival Procedures. Journal of Aircraft,

September, 52(5), pp. 1469-1480. DOI: 10.2514/1.C032967.

Prats, X. et al., (2006). A Framework for RNAV Trajectory Generation Minimizing Noise Nuisances. pp. 1 - 10.Retrievedfrom: https://core.ac.uk/download/pdf/41755854.pdf.

Prats, X., Puig, V. & Quevedo, J., (2010). A Multi-Objective Optimization Strategy for Designing Aircraft Noise Abatement Procedures. Case Study at Girona Airport. Transportation Research Part D, 16(1), pp. 31 - 41. DOI: 10.1016/j.trd.2010.07.007.

Prats, X., Puig, V., Quevedo, J. & Nejjari, F., (2010). Multi-Objective Optimization for Aircraft Departure Trajectories Minimizing Noise Annoyance. Transportation Research Part C, 18(6), pp. 975 - 989.DOI: 10.1016/j.trc.2010.03.001.

Richter, M., Bittner, M., Rieck, M. & Holzapfel, F., (2014). A Non-Cooperative Bi-Level Optimal Control Problem Formulation for Noise Minimal Departure Trajectories. 29th Congress of the International Council of the Aeronautical Sciences, pp. 1 - 7.

Rieck, M. et al., n.d. FALCON.m | TUM – Institute of Flight System Dynamics –Software.[Online] Available at: https://www.fsd.lrg.tum.de/software/falcon-m/ [Accessed 7 August 2019].

The Blue Swan Daily, (2018). Airport Insight: Jakarta Soekarno-Hatta International Airport – Blue Swan Daily.[Online] Available at: https://blueswandaily.com/airport-insight-jakarta-soekarno-hatta-international-airport/ [Accessed 12 August 2019].

Thomas, J. L. & Hansman, R. J., (2019). Framework for Analyzing Aircraft Community Noise Impacts of Advanced Operational Flight Procedures. Journal of Aircraft, 56(4), pp. 1407 - 1417. DOI: 10.2514/1.C035100.

Wijnen, R. & Visser, H., (2003). Optimal Departure Trajectories with respect to Sleep Disturbance. Aerospace Science and Technology, 7(1), pp. 81 - 91. DOI: 10.1016/S1270-9638(02)01183-5.

Appendix A: Noise Footprint Figures

- A320 Noise Footprint
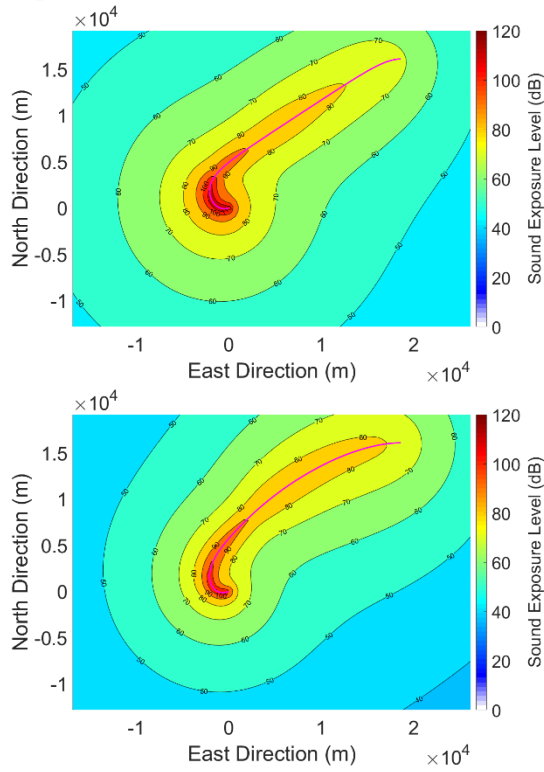
Figure A-1: Sound Exposure Level Footprint for A320 (Top: +0.0% Fuel-minimal Trajectory, Bottom: +5.0% fuel Noise-minimal Trajectory)
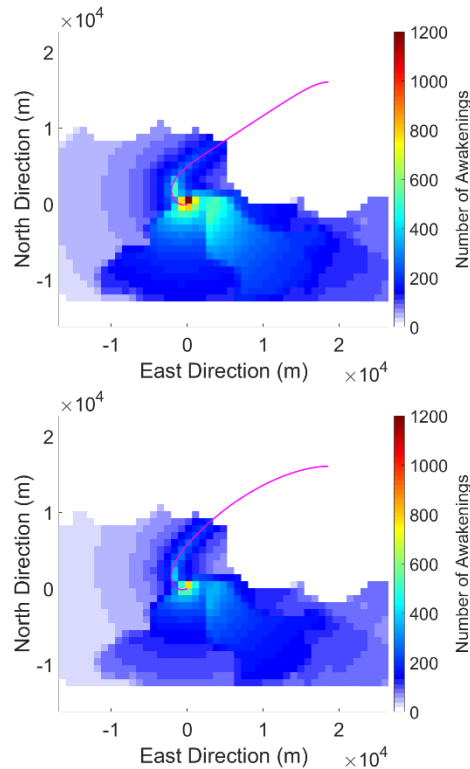
Figure A-2: Number of Awakenings Footprint for A320 (Top: +0.0% Fuel-minimal Trajectory, Bottom: +5.0% fuel Noise-minimal Trajectory)

- A332 Noise Footprint
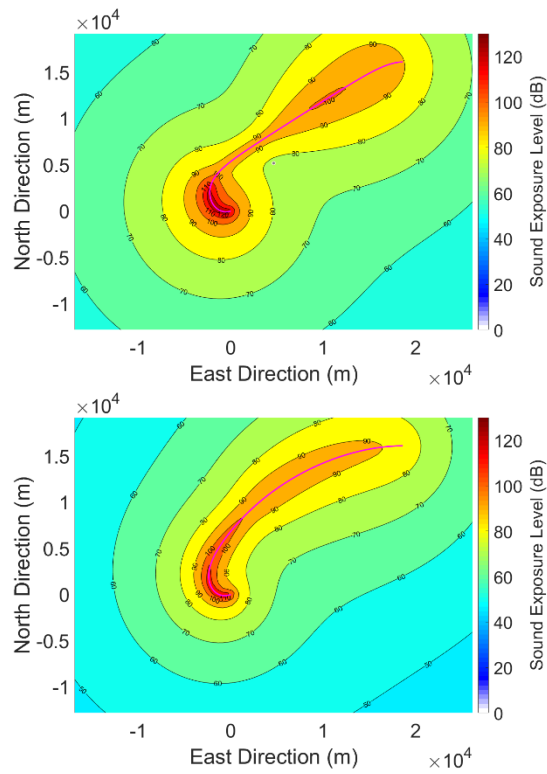
Figure A-3: Sound Exposure Level Footprint for A332 (Top: +0.0% Fuel-minimal Trajectory, Bottom: +5.0% fuel Noise-minimal Trajectory)
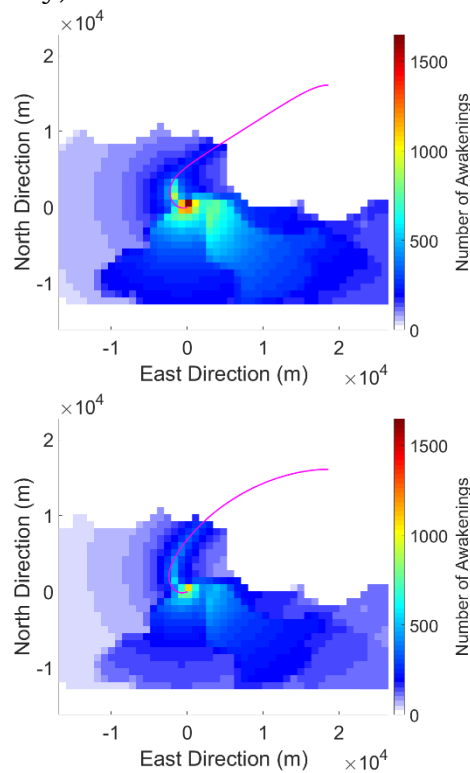
Figure A-4: Number of Awakenings Footprint for A332 (Top: +0.0% Fuel-minimal Trajectory, Bottom: +5.0% fuel Noise-minimal Trajectory)

- B735 Noise Footprint
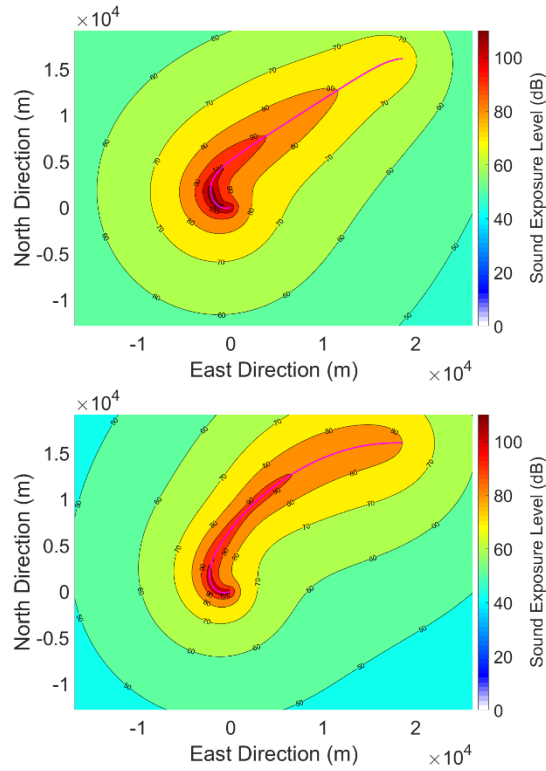
Figure A-5: Sound Exposure Level Footprint for B735 (Top: +0.0% Fuel-minimal Trajectory, Bottom: +5.0% fuel Noise-minimal Trajectory)
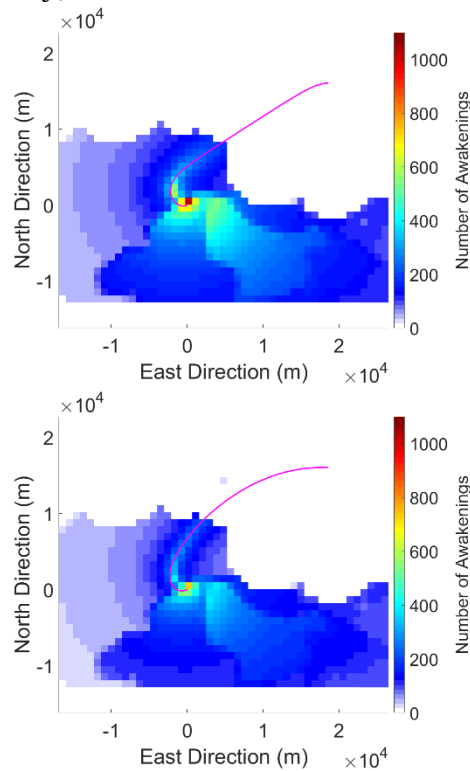
Figure A-6: Number of Awakenings Footprint for B735 (Top: +0.0% Fuel-minimal Trajectory, Bottom: +5.0% fuel Noise-minimal Trajectory)

- B738 Noise Footprint
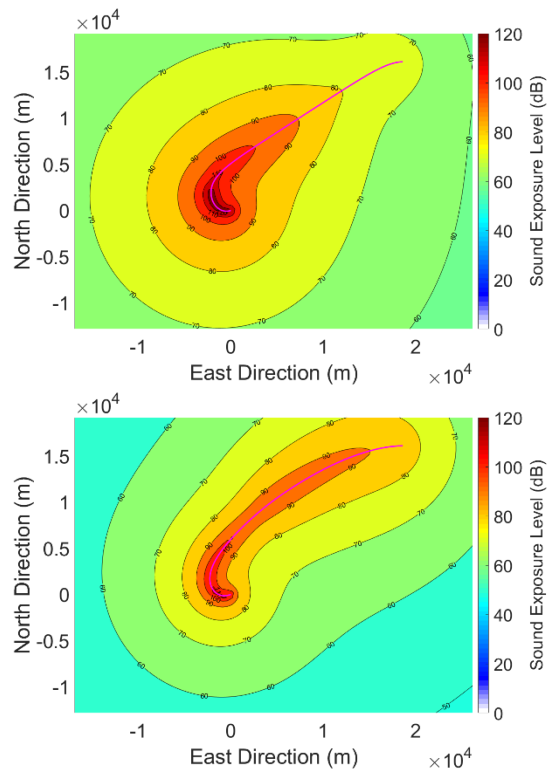
Figure A-7: Sound Exposure Level Footprint for B738 (Top: +0.0% Fuel-minimal Trajectory, Bottom: +5.0% fuel Noise-minimal Trajectory)
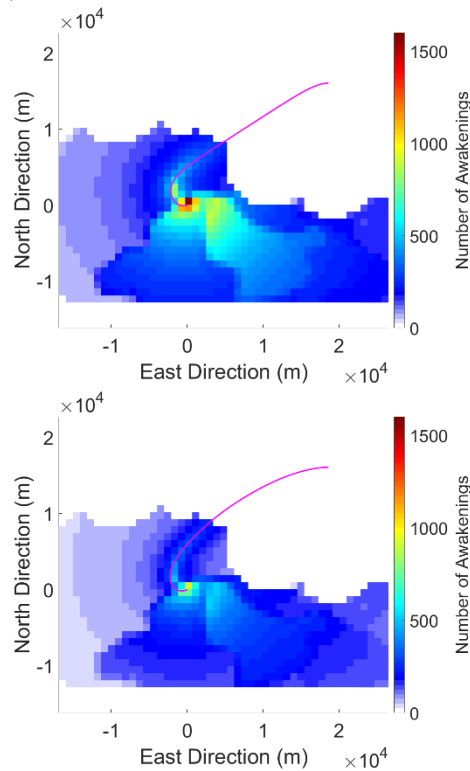
Figure A-8: Number of Awakenings Footprint for B738 (Top: +0.0% Fuel-minimal Trajectory, Bottom: +5.0% fuel Noise-minimal Trajectory)

- B773 Noise Footprint
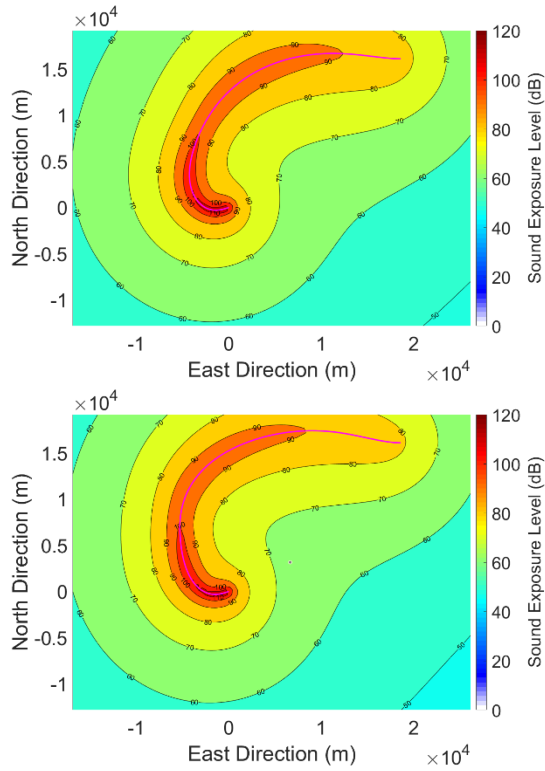
Figure A-9: Sound Exposure Level Footprint for B773 (Top: +0.0% Fuel-minimal Trajectory, Bottom: +5.0% fuel Noise-minimal Trajectory)
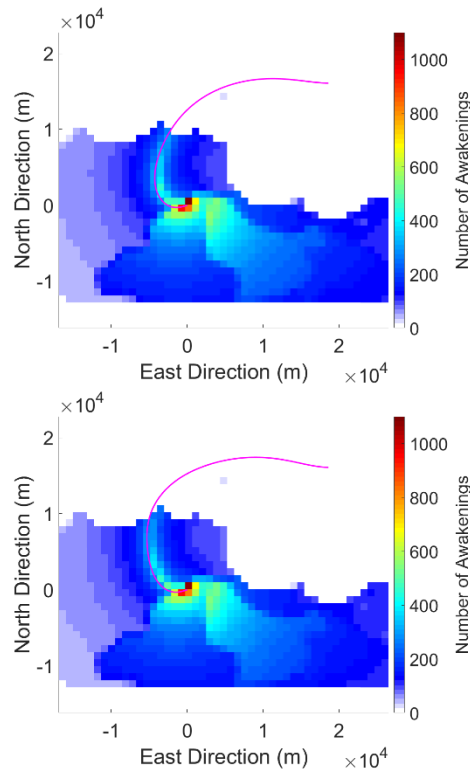
Figure A-10: Number of Awakenings Footprint for B773 (Top: +0.0% Fuel-minimal Trajectory, Bottom: +5.0% fuel Noise-minimal Trajectory)

- CRJ9 Noise Footprint
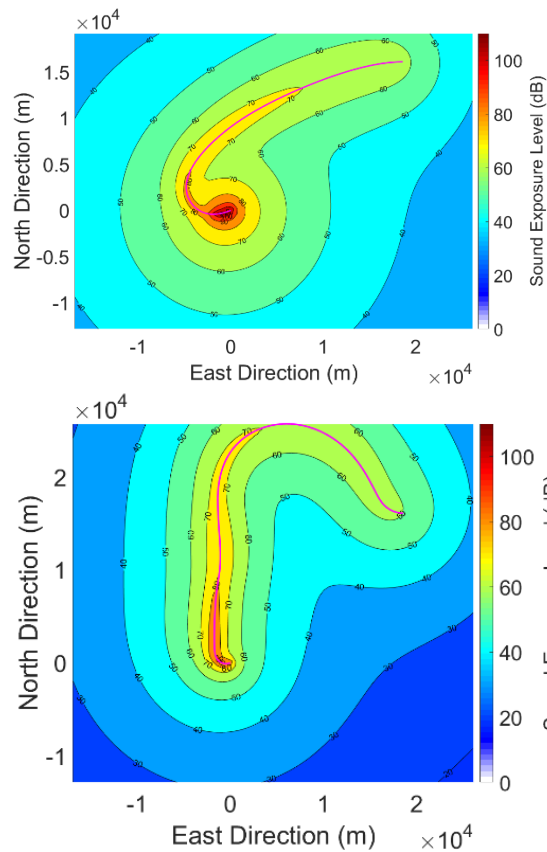
Figure A-11: Sound Exposure Level Footprint for CRJ9 (Top: +0.0% Fuel-minimal Trajectory, Bottom: +5.0% fuel Noise-minimal Trajectory)
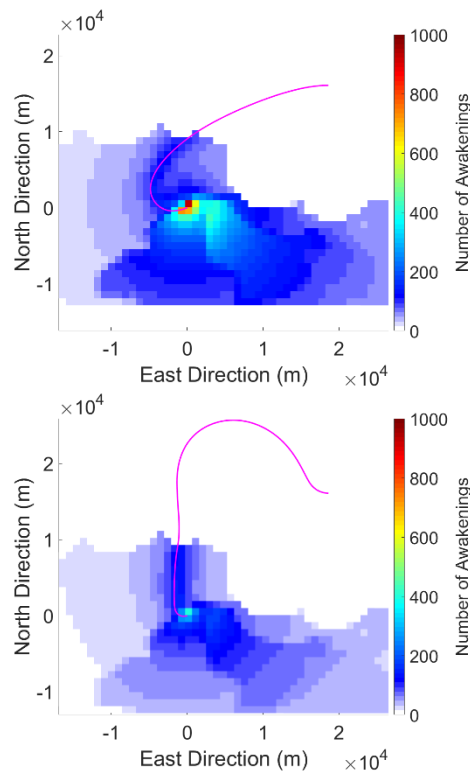
Figure A-12: Number of Awakenings Footprint for CRJ9 (Top: +0.0% Fuel-minimal Trajectory, Bottom: +5.0% fuel Noise-minimal Trajectory)

DESIGN OF FORCE MEASURING SYSTEM ON MAIN LANDING GEAR WEIGHT DROP TESTING MACHINE FOR THE APPLICATION OF LSU SERIES

Yusuf Giri Wijaya[1], Abian Nurrohmad
Aeronautics Technology Center - LAPAN
[1]e-mail: yusuf.giri@lapan.go.id

ABSTRACT

In this research, the design of the force measuring system on the main landing gear weight drop test for the LSU series developed by LAPAN was carried out. The principle of this machine is to apply the load according to the weight of the aircraft on the main landing gear and drop it at a certain height assisted by the guiding rail. At the bottom of this machine, there is an impact platform where each angle is mounted with a load cell that functions to measure the reaction force due to the impact of the main landing gear. Besides, there is a data acquisition system whose function is to process the output signal from the load cell and display measurement data. The data acquisition system used consists of DAQ measurement hardware made by national instruments and LabVIEW software installed on a PC. The design of this testing tool aims to carry out a dynamic impact test on the main landing gear structure of the UAV. The results of the test and calibration show that the force measurement system has an average relative error value is 0.49% and linearity (R^2) is 0.99.

1 Introduction

The development of UAV (Unmanned Aerial Vehicle) is growing rapidly both in Indonesia and all around the world. The demands of research activities related to UAV is not only created high performances products but also must be able to enter the downstream phase.

The most important thing in downstream aerospace technology products is the requirement to have the capabilities required by regulation. In the world of aviation, the safety aspect is mandatory. To ensure the safety aspect, the certification process is carried out by the applicable regulations.

One of the main components in the UAV with a fixed-wing configuration is the landing gear. The landing gear has the function to assist the aircraft in the process of take-off and landing. In several regulations governing aircraft design, both manned and unmanned explained how the minimum specifications of the landing gear structure must be met.

In this research, a device was designed to test the strength of unmanned aircraft landing gear, especially for dynamic loads. The design of this tool is dedicated to LSU (LAPAN Surveillance UAV) Series aircraft. As it is known that LAPAN, especially the Aeronautics Technology center has succeeded in developing UAV variants of LSU starting from LSU 01, LSU 02, LSU 03, LSU 04, LSU 05, LSU 02 NGLD, and LSU 05 NG. This tool is expected to become the standard testing tool for the landing gear UAV that was developed in

Indonesia to meet the safety aircraft regulation certification.

Previously at the LAPAN Aeronautics Technology Center (Wijaya, *et al.*, 2019), LSU landing gear testing was carried out using a static method where the landing gear was given a static load up to its strength limit. The dynamic testing is carried out following the representation of the landing gear load in the flying environment by free fall of the landing gear frame complete with the wheels and the MLW (maximum landing weight) load according to the design of the aircraft's landing gear.

Drop weight testing is one of the destructive testings to investigate the behavior and material characteristics (Mahesh, *et al.*, 2017). One of the functions of drop weight testing is to know the energy absorption of some specimens or part of the structure component. From this testing, the force versus displacement graph can be obtained to analyze the energy absorption characteristics (Taheri-Behrooz, *et al.*, 2013). A similar design is also provided by Galdino et.al (Galdino, *et al.*, 2013). Not only have the function to know the energy absorption but drop weight testing is also can be used to test the performance of the helmet. Shell helmet is impacted using a strike impactor (Yaakob, *et al.*, 2015). Amin et.al use the weight drop test to investigate the characteristics and the behavior of 3D printed bi-material structure, especially on its dynamics characteristics (Amin, *et al,*, 2017).

There is so many research before that developed the weight drop test system for so many applications. One of the weight drop test development has been done by Sharma et.al in 2017. This system is dedicated to investigating the impact force on a carbon composite. This tool also has some function to

determine the material toughness of composite material (Sharma, *et.al.*, 2017). The design and manufacture of low-speed impact tester have been done by Navarrete et.al. This machine is used to investigate the impact response of composite sandwich panel structure. This weight drop testing machine can drop the impactor toward the testing specimen from the maximum height of 2 m. The mass of the impactor is varied from 5 to 25 kg so can provide the maximum kinetic energy to the testing specimen up to 500 Joule (Navarrete, Godinez, & Serrania, 2004). Kurşun et.al investigate the different shapes of the impactor of the weight drop testing machine. This test is done on a sandwich structure to investigate its rigidity (Kurşun, *et al.*, 2016)

Miguel and Alves have done their design of high energy drop weight rig to perform a drop weight tearing test (DWTT). This drop weight rig has a maximum capacity of 42 kJ. To hold the high impact load, some 4.6 tons of steel anvil is used to be the impact platform. At the bottom of this impact platform, 31.8 ton reinforced concrete is used to be its foundation (Miguel & Alves, 2014).

Tanadrob and Suvanjumrat compare the experimental testing and numerical analysis of drop weight testing. The numerical analysis is done using the finite element method. This research is done to benchmarking the material that is used in a speed boat to support the collision accident (Tanadrob & Suvanjumrat, 2017). Kara et.al use image processing to investigate the damage of composite structure when this specimen is tested using drop weight impact machine (Kara, *et al.*, 2017).

From all of this research so it is important to develop the weight drop test machine to investigate the dynamics

characteristics of the landing gear of UAV. The landing gear structure must not fail during its take-off and landing operation. To evaluate this aspect, it is necessary to do the drop impact test on the landing gear structure. The most important thing about this machine is to obtained the force impact data to analyze the absorption energy and the strength of the material.

2 Methodology

2.1. Location and time

Research activities in the form of designing and testing were done in the aerostructure laboratory located in the aeronautics technology center – LAPAN. This research was conducted from October 2019 to February 2020.

2.2. Research Methodology

Figure 2-1 is the flow of this research activity. This research is consists of several steps. The first thing to do is to design the test rig of the weight drop test machine. This tool is operated by drop the mass using a guiding rail by gravity. In the impact area, the force platform is designed to obtain the force data. This design then manufactures in the aerostructure laboratory of the Aeronautics technology center.
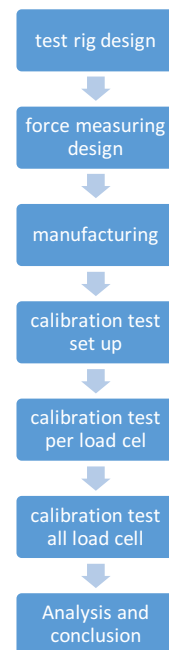
Figure 2-1: Research workflow

After the manufacturing process is done the next step is to do the calibration testing to make sure this machine is can work well. This machine is good to do a test on low strength to weight ratio materials (El-Ariss, 2011).

According to Gunawan, et.al, if there is no friction on the guide rail with the fixture, then to calculate the speed at which the fixture falls, the free fall object equation can be used (Gunawan, *et.al.*, 2011).

The theoretical approach to calculate the speed of the free fall object shown in the equations below:

$$Ep + Ek = constant \qquad (2\text{-}1)$$

$$Ep + Ek = constant \qquad (2\text{-}2)$$

$$mgh_1 + \frac{1}{2}mv_1{}^2 = mgh_2 + \frac{1}{2}mv_2{}^2 \qquad (2\text{-}3)$$

The first state is the condition of the object that has an altitude and has no speed, so the object just has the potential energy due to its height. The second state is the condition of the object that impacts the ground, so the object has no altitude.

$$mgh_1 + 0 = 0 + \frac{1}{2}mv_2{}^2 \qquad (2\text{-}4)$$

So, the speed of the object that impacts the force plate can be expressed on the equation below:

$$v = \sqrt{2gH} \qquad (2\text{-}5)$$

Where g is the value of earth's gravity, which is 9.8 m / s² and H is the height of the test object to be dropped.

To perform the energy absorption analysis some data is required such as the force, acceleration, distance, velocity, and time unit. The energy absorption is present in the Joule unit (Metz, 2007). The calibration process is done in each load cell and then all of the force sensors, in total are four load cells. The final step is to analyze the data obtained from this calibration process.

3 Hardware And Software Design
3.1 Design and principle of Weight drop testing machine

This weight drop testing machine is designed to simulate the conditions under which the UAV is makes a landing. Therefore the method used is to imitate the principle of free fall objects, as has been done by Sharma et.al in 2017 which is used for composite testing (Sharma, *et.al.*, 2017).

The mechanical system in this weight drop testing machine consists of several constituent components, namely: mainframe, guide rail, fixture release mechanism, fixture, and impact platform. The mainframe of this machine is made of H beam iron which functions as a platform to place the guide rail. The guide rail is used as a place for the fixture to slide attached to the landing gear. The fixture attached to the landing gear can be lifted and removed using the fixture release mechanism system.

Between the guide rail and the fixture is made as smooth as possible to eliminate the friction. The design of the landing gear drop test machine can be seen in Fig. 3-1.

The way this machine works is by attaching the landing gear to the fixture. The fixture is positioned at its altitude using a control panel that is adjusted to the desired test specifications. At a suitable height, the fixture is released by means of a release mechanism system so that it will fall in the direction of the guide rail and will hit the impact platform.
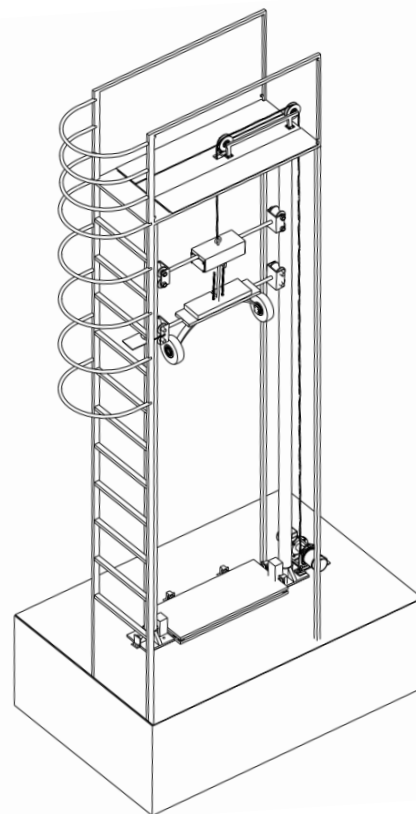
Figure 3-1: The design of landing gear drop test machine
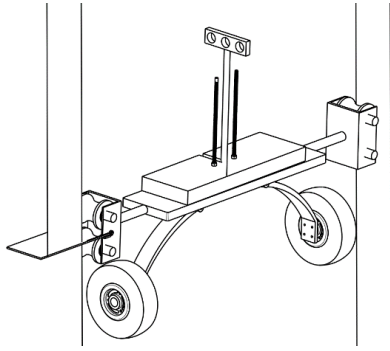
Figure 3-2: The release mechanism of free-fall landing gear

Figure 3-4: The design of impact Platform

The release mechanism of the machine showed in Fig. 3-2. The test article is locked on the plate with three holes at the top of the machine. When the fixture locking is released, the test article will drop freely due to its weight. The impact force that occurs on the impact platform will be measured using a load cell. The final build of the machine can be seen in Fig. 3-3.

Impact platforms are made of iron plates with dimensions of length times width of 0.5m x 1m and with a thickness of 10cm. The weight of the impact platform is 100 kg. With this size, it is expected to be used for various sizes of landing gear or various types of UAV sizes. The design of the impact platform can be seen in Fig. 3-5.

Figure 3-3 : Landing gear drop test Machine

3.2 Impact platform

The impact platform is a part of the landing gear drop test machine whose function is to receive the impact load from the fall of the landing gear when tested. Impact platforms must be designed strong, rigid, and not curved when receiving impact loads. Impact platforms must have a flat surface. The

Figure 3-5: Impact platform

A load cell is installed to support the impact platform. The impact force received by the impact platform will be forwarded to the load cell, so we can find out the value of the impact load. Four load cells are installed at each edge of the impact platform. The load cell is bolted firmly on a base plate with iron material and is embedded in a cast cement so that it is strong, rigid, and not easily swayed. To isolate the effect of vibrations on the surface of the ground that can affect the results of the test,

163

then around the base plate is made a ditch filled with sand.

3.3 Instrumentation

A load cell is a sensor or device used to measure force or weight. The selected load cell is the Strain gauge load cell type. It converts the forces on its surface into changes in electrical resistance. To acquire these sensors, a Wheatstone bridge is used to convert the change in resistance to a change in voltage.

The selected load cell is type H8C manufactured by Zemic. The maximum capacity of the load cell is 500 Kg. Based on information from the datasheet, this sensor has a good level of accuracy and reliability. This load cell sensor material is made from nickel plated alloy steel. The recommendation for the excitation voltage in this load cell is 5 to 12V DC. This load cell has an output rate is 3mV/V. 3mV/V means that the load cell will provide a 30 millivolt signal at full load when excited with 10V DC. Figure 3-6 is the load cell used in this research.
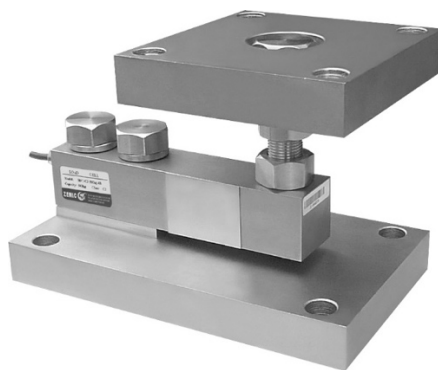
Figure 3-6: Load cell instrument

The output signal from the load cell is processed with a signal processing module made by a national instrument with type NI 9237. This module has 4 analog input channels with half / full Wheatstone bridge configuration and 24-bit ADC circuit resolution. The NI 9237 module is installed in the cDAQ-9184

module, which is a data acquisition system made by NI and is connected to a PC using a LAN cable (Ethernet). The configuration of the force measurement system can be seen in Fig. 3-7.
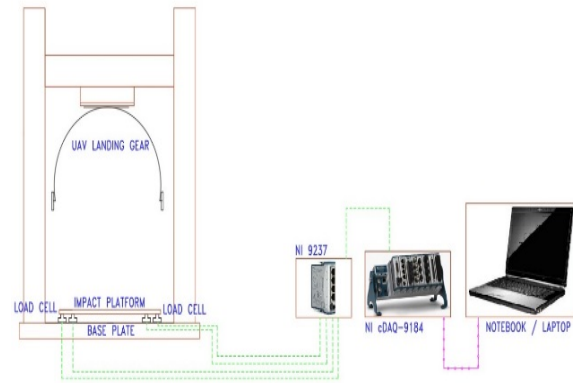
Figure 3-7: Block diagram of the force measuring system

Using Labview to create a user interface software to display the results of force measurements. Labview can be used to create user interface software because of its easy, stable, and powerful programming. With LabVIEW, we can create systems for measuring, controlling, monitoring, and storing data in one application. Data from the test results are stored in Excel form which will simplify the processing and analysis of data. The design of the user interface software made using the LabVIEW program can be seen in Fig. 3-8.
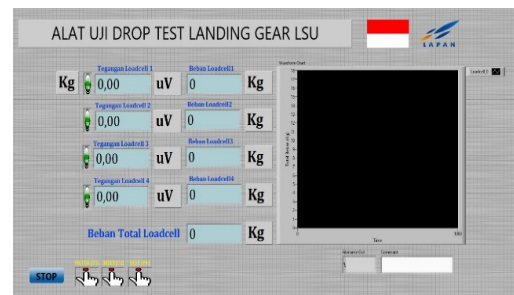
Figure 3-8: Experimental software

4. Results and Analysis
4.1 Calibration test

The system must be validated first using calibration Calibration is performed to ensure that the

measurement data is accurate. Calibration is performed on a data acquisition system for measuring force and load cells. Calibration in the data acquisition system is done by measuring the force input which seems to be an output signal from the load cell. The signal can be simulated using a device called the weight system calibrator manufacture by Vishay with a type 325 model. Figure 4-1 is a tool used to perform system calibration.

Figure 4-1 : Weight system calibrator manufacture by Vishay with type 325 model

The calibration process in the system is done by comparing the values listed in the calibrator, starting from 0 mV/V, 0.5 mV/V, 1 mV/V, 1.5 mV/V, 2 mV/V, 2.5 mV/V, and 3 mV/V with the results of the voltage reading on the LabVIEW. Because what is compared is the voltage value, the values listed on the calibrator need to be multiplied by 10 which is the excitation voltage. From the results of the comparison then the relative error value is calculated. Here is a table of the results of each load cell measurement.

Table 4-1. The result from system Calibration

The rated output voltage from weight system	The output voltage from weight system calibrator	Voltage reading with a force measuring system based

calibrator model 325 (mV/V)	model 325 (uV)	on LabVIEW (uV)
0	0	0
0,5	5000	4968.57
1	10000	9948.44
1,5	15000	14928.47
2	20000	19908.89
2,5	25000	24890.99
3	30000	29870.91

The relative error value from the calibration process is 0.49%. This value is the average of the relative error values in each measurement calculated using the equation:

Relative error value   (4-1)

$$= \frac{[(\text{read value}) - (\text{true value})]}{\text{read value}} \, x \, 100\%$$

The process of calibrating load cells is using a scale made of iron with varying sizes. The size of the scales is 1.1 kg, 5.2 kg, and 10.6 kg. Measurements were started by adding the scales of 1.1 kg 10 times, the scales of 5.2 kg 5 times, and the scales of 10.6 kg 2 times. Then the measurement is continued by reducing the scales in reverse order from the addition of the weight earlier. The values of the scales are compared with the reading voltage values in the Labview GUI, then the data is recorded or stored on a worksheet. The calibration activity is carried out on all four load cell sensors used. The data that has been recorded is then made into a graph. Figure 4-2 to 4-5 show the calibration of the first load cell until the fourth loadcell, namely.
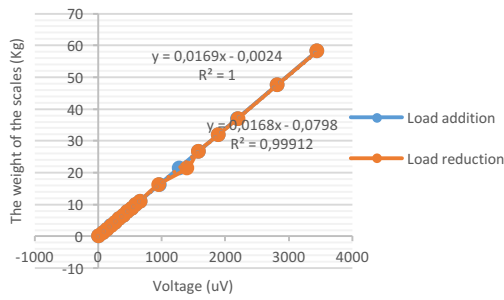
Figure 4-2: First Load cell Calibration
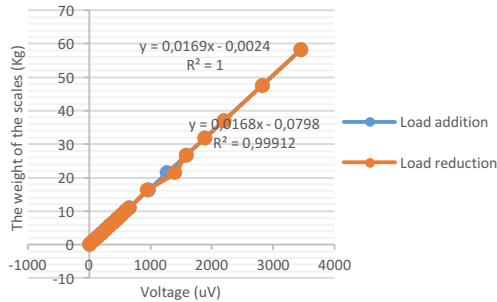
Figure 4-3: Second Load cell Calibration
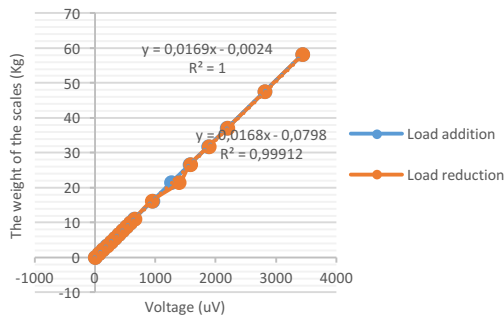
Figure 4-4: Third Load cell Calibration
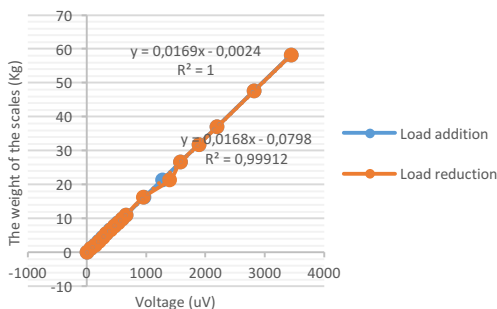
Figure 4-5: Fourth Load cell Calibration

From the results of the calibration for all load cell sensors as seen in Figure 8, 9, 10, and 11, they have almost the same equation that is when adding weight obtained the equation $y = 0.0169x - 0.0024$, and when reducing

weight obtained the equation $y = x - 0.0168x - 0.0798$. Where y is the weight value of the scale with kg and x is the voltage with a microvolt unit.

The calibration process is continued by measuring the weight of the scales with all four load cells at the same time that have been installed on the impact platform. The calibration method is likened to the time of calibration for one load cell.
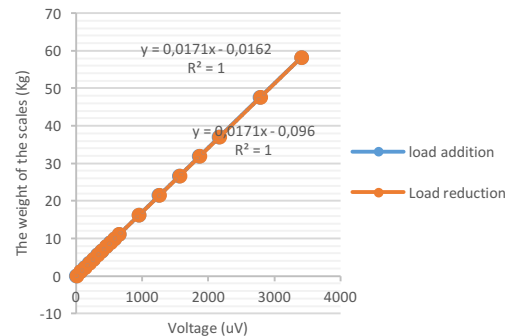
Figure 4-5: Calibration Using Four Load cell

From the calibration as seen in Fig. 4-5, obtained Equation $y = 0.0171x - 0.0162$ when adding weight and Equation $y = x - 0.0171x - 0.096$ when reducing weight. Where y is the weight of the scale with kg and x is the voltage value with the microvolt unit. It can be seen from the two activities of adding and reducing weights on calibration we get a similar equation.

5 Conclusion

Force measurements on main landing gear weight drop test machines for the LSU series aircraft using 4 load cells mounted on impact platforms that are designed to be strong and rigid produce accurate data. The data is processed using hardware which is a national instrument data acquisition system and displayed on Labview-based software.

This system has been validated by calibration both on the data acquisition system and also on every load cell sensor used. Calibration is also carried out on the force measurement system using 4 load cells at the same time mounted on the foot of the impact platform. The results of the test and calibration show that the force measurement system has an average relative error value is 0.49% and linearity (R^2) is 0.99.

Acknowledgment

Reference

Amin, A. R., Kao, Y.-T., Tai, B. L., & Wang, J. (2017). Dynamic Response Of 3d-Printed Bi-Material Structure Using Drop Weight Impact Test. *MSEC2017*, 1–7.

El-Ariss, B. (2011). Instrumented drop weight impact test set-up design and assessment. *International Journal of Structural Engineering*, *2*(1), 85–99. https://doi.org/10.1504/IJSTRUCT E.2011.038071

Galdino, F., Gomes, R., & Ferreira, W. (2013). Development of a Machine Per Drop Weight Impact for, (Cobem), 7633–7641.

Gunawan, L., Dirgantara, T., & Putra, I. S. (2011). Development of a Dropped Weight Impact Testing Machine. *International Journal of Engineering & Technology IJET-IJENS*, *11*(December), 98–104.

Kara, M., Uzun, Y., & Arikan, H. (2017). Mapping with the Image Processing Method of Damage Regions with Respect Composite Laminates Subjected to Low Velocity Publication Info Mapping with the Image Processing Method of Damage Regions with Respect Composite Laminates Subjected to Low Velocity, (March), 1–8.

Kurşun, A., Şenel, M., Enginsoy, H. M., & Bayraktar, E. (2016). Effect of impactor shapes on the low velocity impact damage of sandwich composite plate: Experimental study and modelling. *Composites Part B: Engineering*, *86*, 143–151. https://doi.org/10.1016/j.composit esb.2015.09.032

Mahesh, S., Hemantha, B. S., Hiremath, N. M., & Chethan, M. (2017). Design , Development and Fabrication of a Fixture for Drop Weight Machine, *4*(04), 131–136.

Metz, R. (2007). Impact and drop testing with ICP® force sensors. *Sound and Vibration*, *41*(2), 18–20.

Miguel, C., & Alves, M. (2014). Design of a high-energy drop weight rig. *Congresso Nacional de Engenharia Mecânica 2014*, (March 2015). https://doi.org/10.13140/2.1.3430 .7361

Navarrete, M., Godinez, F. ., & Serrania, F. (2004). Design and Fabrication of a Low Speed Impact Tester. *Journal of Applied Research and Technology*, *2*(3), 249–254.

Sharma, A., Karthik, D., Kumar, H. J., & Naveen, H. E. (2017). Design and Fabrication of Drop Weight Impact Testing Machine. *Imperial Journal of Interdisciplinary Research (IJIR)*, *3*(6).

Taheri-Behrooz, F., Shokrieh, M. M., & Abdolvand, H. R. (2013). Designing and manufacturing of a drop weight impact test machine. *Engineering*

Solid Mechanics, *1*(2), 69–76. https://doi.org/10.5267/j.esm.2013.08.001

Tanadrob, K., & Suvanjumrat, C. (2017). Composite material modeling under drop weight impact test using finite element analysis. *Materials Science Forum*, *889 MSF*, 3–8. https://doi.org/10.4028/www.scientific.net/MSF.889.3

Wijaya, Y. G., Ula, N. M., & Muksin. (2019). Integration Of Data Acquisition System For Main Landing Gear LSU-02 NGLD Static Test. In *Seminar Nasional Iptek Penerbangan dan Antariksa XXIII* (pp. 137–147). Tangerang Selatan: Indonesian book Project.

Yaakob, M. S., Abdullah, M. N., Muda, M. K. H., & Mustapha, F. (2015). Drop-Weight Impact Test for Measuring the Damage Resistance of Aero Helmets. *Journal of Advanced Research in Applied Mechanics*, *8*(1), 31–39.

BALLISTIC FLIGHT AND CONTROL SIMULATION OF RKX200TJ/BOOSTER DURING BOOST AND CLIMB-PHASES

Hakiki

Rocket Technology Center, LAPAN

e-mail: haqq.lapan@gmail.com

ABSTRACT

The problem encountered while developing the RKX-200TJ/booster is the measurement of vehicle mass (center of gravity). The thrust line of the rocket booster does not coincide with the center of gravity can induce a pitch disturbance. By controlling the pitch parameter, the pitch disturbance phenomenon can be minimized. In this paper presents the flight performance and dynamics analysis and the design of the pitch and roll control system for RKX200TJ/booster during rocket boost and climb phase. The result indicates that the pitch disturbance can be reduced until 27% decrease whereas roll angle (ϕ) can be damped at zero level ($\phi = 0$). Pitch angle (θ) can be maintained at angle 5° for the climb phase. Although the one of moment arm case shows the static instability and uncontrollability during rocket boost phase, the control system can control the vehicle to further phase. This simulation is presented in X-Plane and Simulink. The PID controller is selected in the control system design.

Keywords: *PID controller, RKX200TJ/booster, rocket booster, X-Plane, Simulink.*

1 Introduction

The development of unmanned aerial vehicle (UAV) technology has been growth more progress, such as the variantions of configuration form, advances in electronic system devices and increased thrust engine power. UAVs are commonly categorized into three groups based on configuration, capability and flight mission, namely fixed-wing UAVs, rotary-wing UAVs, and Hybrid UAVs (R. Austin, 2010). In the last decade, as several small industries and hobbies have made UAV known as drones, so that researchers or academics who working in the field of system devices often use them as a vehicle to develop their avionics systems.

Researchers or engineers have been conducting experiments to develop the concept of a short take-off in UAV in the last decade, although this concept has emerged a long time ago. The main idea of the concept is that the UAV can be launched in a catapult or booster environment. The last type is an assistance take-off device to assist the vehicle by providing an additional small rocket boost. This type can be used anywhere, even on the ships because it does not require a runway (Hakiki, 2020).

Rocket Technology Center (Pustek Roket) still develops the UAV technology, in particular the control system. The control system used is software and hardware system which have an open-source research platform enable full onboard processing on a micro air vehicle (Lorenz, *et al.*, 2011). This control system has been applied on high subsonic speed vehicle and it works but there are still inaccuracy. Based on several experience in testing, it is

necessary to research independent control system further.

RKX-200TJ/booster is an designed unmanned aerial vehicle (UAV) flies at speed 200 – 250 km/h and can be used to the telemetry control system testing (Satrya, *et al.*, 2014). The vehicle has not landing gear for take-off dan landing. The vehicle uses pneumatic launcher for take-off (Hakiki and Edi Sofyan, 2013), besides a single rocket booster. Whereas the second thrust using jet engine for cruise phase of flight.

Previously, several studies have been published concerning the RKX200 vehicle, in regarding to design, simulation, measurement and manufacturing. Riyadl in (Riyadl, 2015) researched the effect of moments on the flight dynamics of the RKX-200TJ/booster to determine the optimal moment distance so that the vehicle can fly quite stable during take-off phase. During take-off phase by using booster rocket, there are the change in aerodynamic forces and the shift of vehicle's center of mass. The shift of the mass center will result in a moment force on the vehicle because of the booster thrust, (Riyadl and Hakiki, 2014). In this case is not explained how the control system is applied on vehicle so that the vehicle can fly adequately stable in spite of disturbance occurrence. Shandi *et al.*, predicted the location of the center of gravity of the RKX200TJ/booster. The center of gravity (CG) prediction based on mathematical calculations. The calculation is done by knowing the weight of each component of the vehicle and then calculating its effect on the vehicle's center of gravity. Calculations are carried on in the X-axis direction (X_{CG} abscissa point) and Z-axis direction (Z_{CG} ordinate point) in two flight conditions, namely take-off phase and the rocket booster is burned out.

(Shandi and Hakiki, 2016). Shandi *et al.*, only performed the CG calculations and did not discussed the flight performance dan dynamics. This calculation provided a reference for other further designs. Meanwhile, Bo Liu *et al.*, analyzed the take-off process on UAVs with a single rocket booster. Modeling is done using ANSYS, wind tunnel testing, and empirical calculations. Simulations were performed by varying the booster angle deviation longitudinally and laterally (Liu, *et al.*, 2011) instead of the moment arm in their paper. Once the single rocket booster has burned out, the velocity of UAV decreased. So, the designed control system was less effective.

Riyadl explained the occurrence of a wobbling movement on a ballistic rocket. This phenomenon can occur because the point of the rocket's center of mass which is not located on the symmetry axis of the rocket. The asymmetry of the center of mass causes disturbance in the roll, pitch and yaw moments on the rocket, where the perturbation of the roll, pitch and yaw moments triggers the wobbling motion (Riyadl, *2015*). The asymmetry effect of the rocket itself is taken into consideration in the control system design of RKX-200TJ/booster.

Based on the above background, this paper analyzes the pitching moment effect of the RKX-200TJ/booster in terms of flight performance and stability, and then carried on the pitch and roll control system design for rocket booster and climb phases so that the vehicle flies stable.

2 Methodology

The line of force of the rocket booster usually passes through the center of the vehicle's mass (center of gravity, CG) in ideal conditions. In real condition, this is not a fact. This problem often occur a

measurement error. The misalignment of the rocket's propulsion line to the CG point generates a moment arm (d_{arm}) so that it affects the stability and its flight path. If the CG point lies above the thrust line, it will cause a pitch-up moment, as shown in Figure 2-1 (a). Otherwise, if the point CG lies below the thrust line, it will cause a pitch-down moment, as shown in Figure 2-1 (b). In this case, the point CG is assumed to lie only in the direction of the longitudinal axis and the vertical axis of the vehicle.
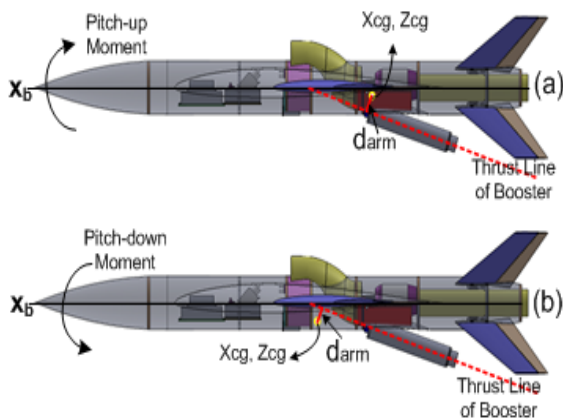
Figure 2-1: Illustrates the pitch effect

The aircraft model is simulated in X-plane in which the characteristics of aerodynamic can be used to predict the flying qualities. So, the block aircraft dynamics is replaced by the flight simulator X-plane (Kaviyarasu and Senthil, 2014), whereas the control system design is presented in Simulink, as shown in Figure 2-2. The UDP (*User Datagram Protocol*) communication is built between Simulink and X-Plane in one computer by using IP address (Bittar A., *et al.*, 2013). In this paper is not addressed in term of UDP in detail. It has been discussed by Hakiki, 2020.
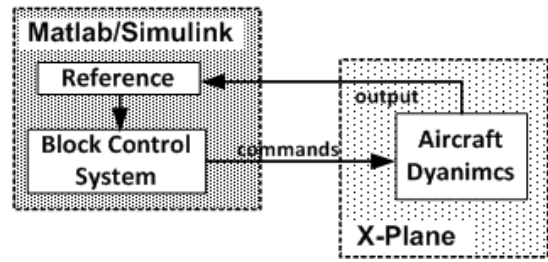
Figure 2-2 : Block diagram construction

2.1 Simulation Parameters

The setting angle of the rocket booster to longitudinal axis has the same angle size as the flight elevation angle of 18°. The launcher is modeled as a landing gear which is a skids type gear (Laminar Research, 2013), as shown in Figure 2-3. The simulation is conducted by varying the selected moment arms referring to the references (Shandi and Hakiki, 2016). The selected moment arms are shown in Table 2-1. A positive sign indicates that the CG point lies above the thrust line of the rocket. Otherwise, a negative sign indicates that the CG point lies below the line of thrust of the rocket.

Figure 2-3 : Display RKX200TJ/booster

Table 2-1 : Data of mass and size of arm Moment

Vehicle Types	Total Mass (kg)	Moment Arm, d_{arm} (cm)
W_{CG1}	30.5	2.87
W_{CG2}	29.2	1.32
W_{CG3}	29.4	-1.91
W_{CG4}	25.8	0.4

2.2 Design of Control System

The designed pitch control system aim to maintain and control the pitch disturbances during a booster and climb phases. Whereas the roll control system keeps wing symmetrical wing position (wing leveler).

The configuration of the pitch control system is used, as shown in Figure 2-4. This system has three loops. Outer loop is in the feedback pitch angle (θ_c) and there are two inner loops, namely the pitch damper and the feedback elevator deflection. The pitch damper system is implemented to increase the damping ratio of the pitch oscillation mode (Hakiki, 2020). The pitch angle reference (θ_{ref}) and the angle θ_c pass through the comparator, resulting in an error signal (θ_e). This is then multiplied by the controller's pitch gain (θ_{gain}), yielding the input for the pitch damper system block. Signal ($\Delta\theta$) and signal (q), which is amplified by the pitch rate gain (q_{gain}), are compared to produce an elevator deflection signal ($\Delta\delta_e$). This signal is added to the feedback elevator deflection signal (δ_{ec}), obtaining a new elevator deflection position (δ_e), as shown in Figure 2-4 (Bittar, *et al.*, 2013), (Hakiki, 2020).
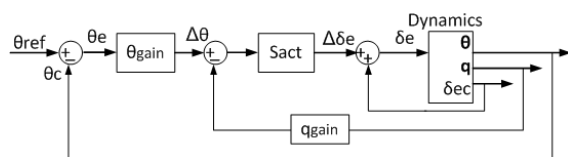
Figure 2-4 : Pitch control block diagram

Control system block diagram is responsible to maintain wing leveler, as shown in Figure 2-5. The roll damper helps to improve the effect of artificial increase in wingspan. The roll mode can also influence the aircraft's trajectory by causing a delay of the time when a turn is commanded (Peters and Konyak, 2012). Block Diagram is shown Figure 2-

5 indicates that the signal (ϕ_e) is deviation between the reference *roll* (ϕ_{ref}) and the current *roll* (ϕ_c). The signal is ehnanced with the roll signal gain (ϕ_{gain}) to become signal Δp. The servomotor for moving the deflection of aileron is generated from the ratio of the signal Δp to the feedback angular velocity signal (p) which is amplified by the roll rate gain (p_{gain}) (Bittar, *et al.*, 2013), (Hakiki, 2020).
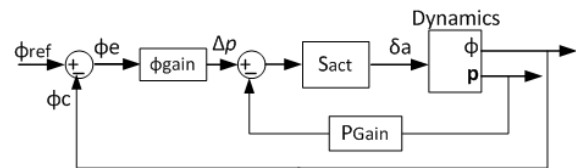
Figure 2-5 : Block diagram of roll control

The control system chosen is PID. To get the PID control feedback effect on the system motion by varying the gain value (Purwanto, *et al., 2013*). In this research, the PID coefficient is obtained based on trial and error. S_act is a transfer function for actuators. The transfer function is represented as a first-order system as seen in equation 2-1. τ is a time constant , which is set to 0.1 s (Nelson, 1998).

$$S_{act} = \frac{1}{\tau s + 1} \qquad (2\text{-}1)$$

3 Result dan Analysis

The simulation conducted at two flight condition, that is :

a. Ballistic flight.
   The vehicle is pushed by a single rocket booster which has an average mass and thrust of 3 kg and 150 kgf, respectively. It has a burn time of about 1.2 s.

b. Flight by control system.
   During the booster phase, θ_{ref} is adjusted according to the flight elevation angle. θ_{ref} is set at 5° to the climb phase. After the rocket booster phase, the turbo jet engine

(sustainer) acts as a propulsion in the next phase. The sustainer is idled prior to take-off.

3.1 Ballistic Flight

The three flight parameters indicate that the vehicle is statically stable but the only one is instability. Stability of the vehicle can be seen from the response to the changes in the pitch angle (θ), the roll angle (ϕ), angle of attack (α) and side-slip angle (β) as shown in Figure 3-1, Figure 3-2, Figure 3-3, and Figure 3-4. Whereas Figure 3-5 and Figure 3-6 illustrate the aircraft flight performance.

The first case (d_{arm1}) which refers to Table 2-1, the vehicle experiences a pitch-up where the change in θ reaches 86° for 1.8 s, as shown in Figure 3-1. The vehicle tends to be unstable. The vehicle even experiences a pull-up accompanied by rolling movement, such as showing a spiral motion or the starting of a wobbling motion. The graph is shown in Figure 3-2 indicates that the change in ϕ reaches -180° in 1.4 s, followed by a roll movement of +180° at the 2nd second so that it causes a spiral motion. The other graph can also be seen the change in α during the first 1.8 s. The change in α occurs from 5° at 0.4 s to 25° at 1.4 s, as shown in Figure 3-3. The vehicle experiences a loss of lift or a stall at the 1.4 s in this regime. Overall, the change in β decreases and tends to move stable after the first second. It does not really affect the vehicle dynamics, except at the 6.6th second where there is the change in β by -8°. The vehicle experiences instability in the initial phase so that it affects its flight path further as shown in Figure 3-6.

The change in θ reaches 71° within 1.5 s occurs in the second flight condition (d_{arm2}), as shown in Figure 3-1. Once the rocket booster has burned out,

the vehicle is quite stable. Because the static stability range is still fulfilled so that it can restore its attitude towards the disturbance direction. The changes in ϕ, α and β tend to be stable, as shown in Figure 3-2, Figure 3-3, and Figure 3-4, so that the flight path is according to its azimuth direction, as seen in Figure 3-6. The altitude and range of the vehicle are 126.8 m and 173.3 m, respectively, whereas the flight time is 11.6 s. The range calculation can be seen on the reference (Jan-Philip, 2010).

The next variation of the moment arm (d_{arm3}), the vehicle tends to move a pitch-down until the change in θ reaches -5° within 1.2 s, as shown in Figure 3-1. Despite returning to pitch up, the vehicle has lost its lift. Range and altitude are quite short about 66.4 m in 2.8 s with and 3.65 m, respectively, as shown in Figure 3-6. The angles of ϕ, α, and β are stable tendency, as shown in Figure 3-2, Figure 3-3, and Figure 3-4.

In last variant, the vehicle flies very stable although the angle θ rises to 36°, as shown in Figure 3-1. The other motion responses also indicate that the vehicle is stable. The rocket booster thrust can push the vehicle achieving nearly 250 m for 9.2 s while altitude approaches 78 m, as shown in Figure 3-6.

The flight speed profiles generally show the same pattern characteristics, as seen in Figure 3-5. There are differences of velocity which is affected by the difference in the mass of the vehicle, the angle θ and the moment arm size. The effect of θ indicates that the great pitch angle comes low velocity. The pitch angle effect is related to the gravity factor. The greatest velocity occurs on a vehicle with a moment arm (d_{arm3}) of 61.2 m/s, followed by d_{arm4}, d_{arm2}, and d_{arm1}, respectively, are 56.7 m/s, 49 m/s and 43 m/s. The last one, shows the

vehicle speed in unstable conditions. At 1.4 s, a stall occurs when the angle α reaches 25° and the velocity of about 36 m/s.

Figure 3-3 : Angle of attack response

Figure 3-1 : Pitch angle response
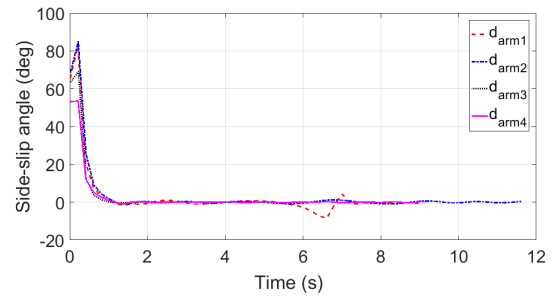
Figure 3-4 : Side-slip angle response

Figure 3-2 : Roll angle response
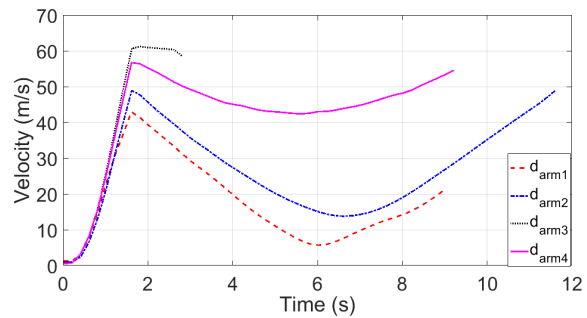
Figure 3-5 : Velocity profile
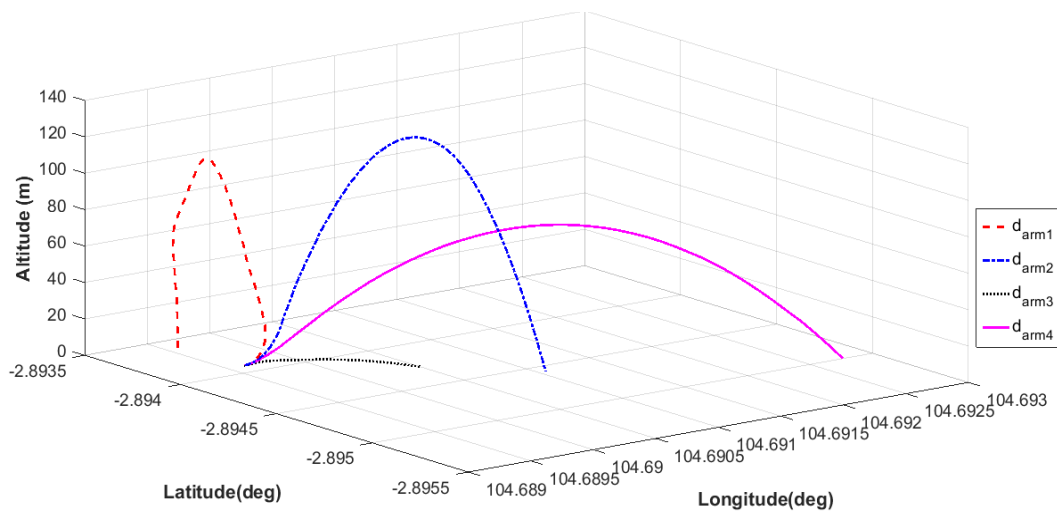
Figure 3-6 : Trajectory of ballistic flight

3.2. Flight by Control System

The PID coefficient values are selected as shown in Table 3-1. Overall, the control system manage to control the vehicle well, except the case of d_{arm1}.

Table 3-1 : The PID Coefficient chosen

Gain Controller	P	I	D
θ_{gain}	-0.3	0	0.1
q_{gain}	-0.1	0	0.15
φ_{gain}	-0.1	0	0
p_{gain}	0	0	0.1

In the case of d_{arm1}, the stability disturbance is large enough so that the vehicle is quite difficult to control parameters of θ and ϕ in the first 10 s as shown in Figure 3-7 and Figure 3-8. Since parameters of θ and ϕ are disrupted, the other parameters also are disturbed such as angles α and β. The control system can stabilize the parameters of θ and ϕ subsequently. In the second flight condition (d_{arm2}), the pitch angle can be reduced from 71° in ballistic flight to 56°. The pitch angle control further manages to maintain the angle of 5° with a settling time of 2.8 s. In the third case, the angle θ can be reduced to -1.5° for 1.2 s, while a settling time is 2.8 s next phase. The latter case, the angle θ can be damped a 27% drop compared to the ballistic phase. Settling time even is faster than others by 2.5 s.

During the autopilot phase, the lateral disturbance can be well damped, as shown in Figure 3-8, except the case of d_{arm1}. In contrast to the response of angle α, the disturbance occurs at the beginning of the rocket booster phase. After the 5th second, the angle α is adequately stable, as shown in Figure 3-9. The change in the angle θ affects the angle α and the flight path angle so that it can be altered its trajectory. Overall,

the response of the angle β is stable, as shown in Figure 3-10.

The flight speeds in the case of d_{arm1}, d_{arm2}, d_{arm3}, and d_{arm4}, respectively, were 41 m/s, 50 m/s, 57 m/s and 54 m/s as shown in Figure 3-11. There are value difference of flight speed occurs between the autopilot phase and ballistic flight after the rocket booster is burned out. This difference is due to the effect of drag on the deflected control plane and the change in the angle α. The flight parameter (d_{arm4}), there is a disturbance after the 16th second, but it was still within a reasonable limit of stability, as shown in Figure 3-7, although this disturbance slightly affects the vehicle flight speed, as seen in Figure 3-11.

The cases of d_{arm2}, d_{arm3}, and d_{arm4} indicate that the trajectory corresponds to the azimuth angle by 113° North. In contrast, there is a flight path deviation which the case of d_{arm1} strays around 90° to the azimuth angle, as shown in Figures 3-12 and 3-13.
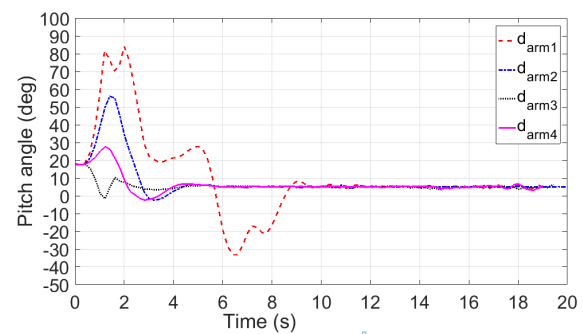
Figure 3-7 : Response of the change in θ
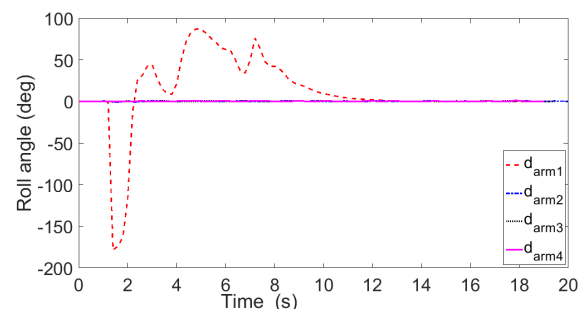
Figure 3-8 : Response of the change in ϕ
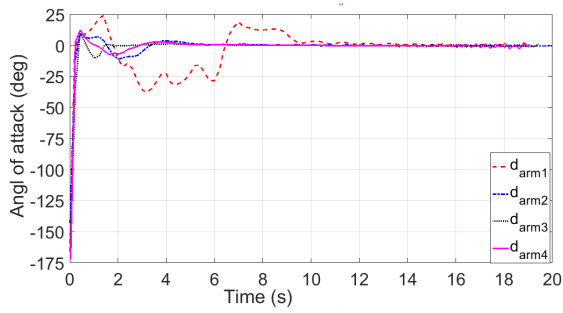
Figure 3-9 : Response of angle of attack change
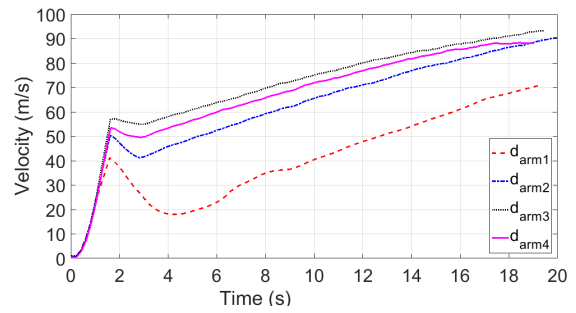
Figure 3-11 : Flight speed profile
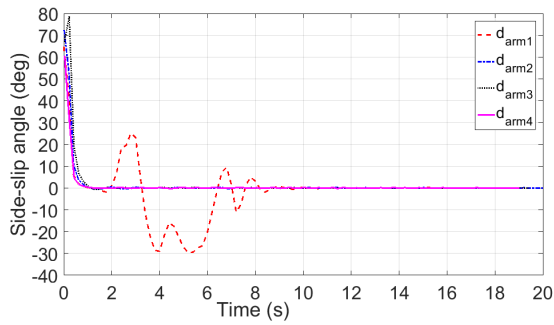
Figure 3-10 : Change in β response
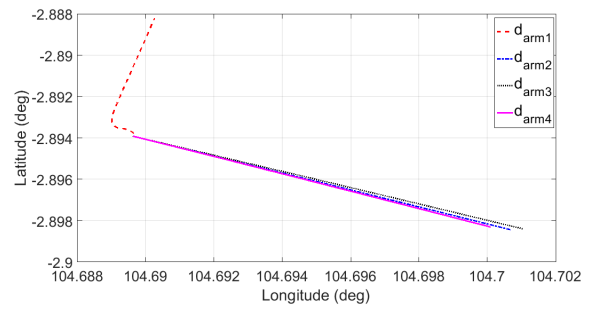
Figure 3-12 : A flight path in a geographiccoordinate system
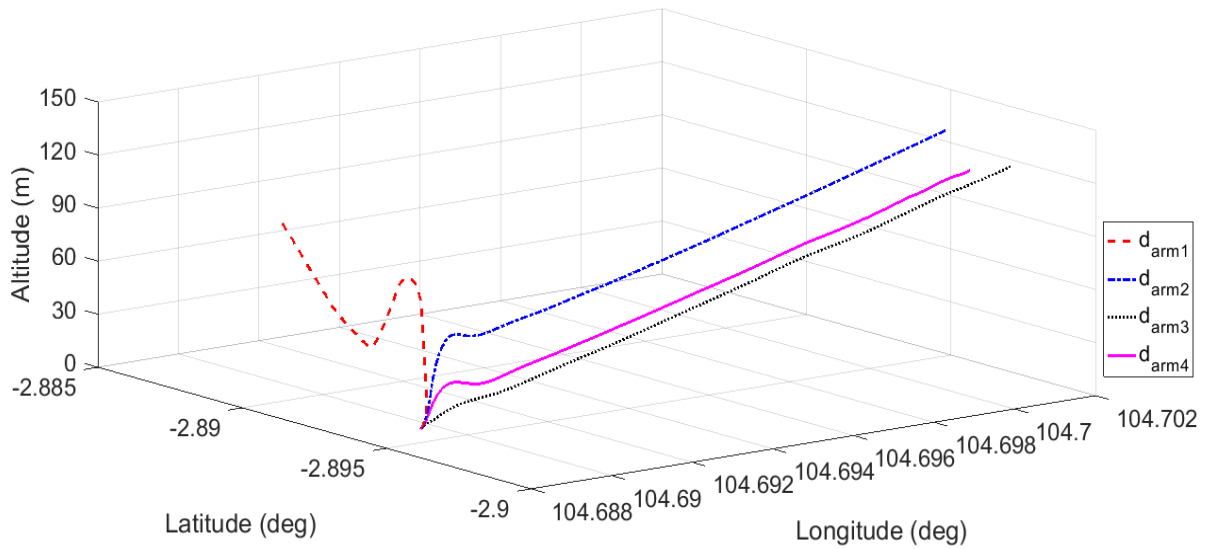
Figure 3-13 : Path flight

4   Conclusions

Overall, the control system which the PID coefficient value above indicates an overview of the characteristics of the vehicle controlled. Except, in the case of the moment arm (d_{arm1}) which shows static instability and uncontrollability during the rocket booster phase. The pitch control system can control parameter θ so that reduce the pitch angle increase of 21-27% and maintain the angle θ of 5°. While the roll control system can reduce lateral interference by maintaining the wing position at zero level ($\phi = 0$).

This paper provides conclusions and input for further design, namely the maximum limit of the moment arm value that is still feasible for the designed vehicle is 1.32 cm which the CG point lies above the thrust line of the booster.

Whereas the CG point lies below the thrust line of the booster is 1.9 cm.

Acknowledgements

References

R. Austin, (2010), *Unmanned Aircraft Systems UAVS Design*, Development and Deployment, John Wiley & Sons Ltd, Great Britain, pp. 35–43.

Hakiki, (2020), *Research on Co-Simulation of Flying for an Unmanned Aerial Vehicle (UAV)*, Keimyung University, South of Korea.

Lorenz Meier, Petri Tanskanen, Friedrich Fraundorfer, Marc Pollefeys, (2011), *PIXHAWK: A system for autonomous flight using onboard computer vision*, Proceedings - IEEE International Conference on Robotics and Automation May 2011, DOI: 10.1109/ICRA.2011.5980229.

Satrya, E., Riyadl, A., Sudiana, O., Hakiki., Sofyan, E., (2014). *Proses Perancangan Wahana RKX 200-EDF*, Hasil Penelitian Dan Pemikiran Ilmiah Tentang Teknologi Pesawat Terbang, Tangerang.

Hakiki., Sofyan, E., (2013), *Controlling X-Plane Flight Simulator Environments From Matlab For RKX-EDF Launch Scenario*, Proceedings International Seminar Of Aerospace Science And Technology 17th SIPTEKGAN, Tangerang.

Riyadl, Hakiki, (2014), *Pengaruh Momen Akibat Gaya Dorong Roket Booster Pada Dinamika Terbang Wahana RKX-200TJ : Studi Kasus Pada saat Take-off*, pp 196-203 , SIPTEKGAN XVIII, Rumpin

Shandi, Hakiki, (2016), *Prediksi letak pusat Gravitasi RKX-200TJ/Booster*, pp 57-64, SIPTEKGAN XX 2016 Rumpin Bogor 2016

Bo Liu, Zhou Fang, Ping Li and Chuanchuan Hao, (2011), *Takeoff analysis and simulation of a small scaled UAV with a rocket booster*, Advanced Materials Research Vol 267 (2011) pp 674-682 ©(2011) Trans Tech Publications, Switzerland,doi:10.4028/www.scientific.net/AMR.267.674

Riyadl, (2015), *Pengaruh dari Posisi Pusat Massa Roket yang tidak Terletak pada Sumbu Axis Simetri Terhadap Dinamika Terbang Roket Balistik*, pp 139-148 – Journal of Aerospace Technology vol 13 December 2015 ISSN 1412-8063.

Kaviyarasu, A., and Senthil, K. K., (2014), *Simulation of Flapping-wing Unmanned Aerial Vehicle using X-plane and Matlab/Simulink*, Defence Science Journal, 64(4), pp. 327-331. DOI: 10.14429/dsj.64.4933.

Bittar A.; Oliveira N., (2013), *Central*

Processing Unit for An Autopilot : Description and Hardware-In-the-Loop Simulation Autopilot. In Journal of Intelligent and Robotic Systems, April 2013, pp. 557–574. DOI 10.1007/s10846-012-9745-y.

Laminar Research, (2013), "*Plane Maker for X-Plane 10,*"

Eko B. Purwanto, Sufendi Lie, Syahron H. Nasution, 2013, *Pemodelan dan Simulasi Sistem Kendali Proportional Integral Derivative untuk Kestabilan Dinamika Terbang,* Majalah Sains dan Teknologi Dirgantara Vol. 8 No. 2, 48-59.

Peters, M., and Konyak, M. A., (2012), *The Engineering Analysis and Design of the Aircraft Dynamics Model For the FAA Target Generation Facility,* Final Report, Simulation Branch and Laboratory Services Division, Atlantic City, pp. 17–20.

Nelson, R. C., (1998), *Flight Stability and Automatic Control,* 2nd ed., McGraw-Hill New York, pp. 210–215.

Matuscheck, Jan-Philip, (2010), *Finding Points Within a Distance of a Latitude/Longitude Using Bounding Coordinates,* from http://janmatuschek.de/LatitudeLongitudeBoundingCoordinates diakses pada 29 April 2019.

AUTHOR INDEX

KEYWORD INDEX

(Pedoman Penulisan Jurnal Teknologi Dirgantara)
JUDUL MAKALAH DITULIS DENGAN HURUF KAPITAL TEBAL SECARA SINGKAT DAN JELAS, (Studi Kasus : apabila ada)
(16 pt, Britannic Bold)

Judul dibuat dalam 2 bahasa (Indonesia dan Inggris), apabila tulisan dalam bahasa Indonesia, maka judul dalam bahasa Inggris ditulis dalam tanda kurung
(16 pt, Britannic Bold)

Penulis Pertama[1], Penulis Kedua[2], dst[n] ⟵ (Nama Penulis Tanpa gelar)
(10,5 pt, Franklin Gothic Medium, bold)

[1]Instansi Penulis Pertama
[2]Instansi Penulis Kedua
dst[n.]....
(10,5 pt, Franklin Gothic Medium)

e-mail: e-mail penulis pertama ⟵ (berwarna hitam)
(10,5 pt, Franklin Gothic Medium)

ABSTRACT
(10,5 pt, Bookman Old Style, bold)

Abstract is a summary of the most important elements of the paper, written in one paragraph in the one column of a maximum of 200 words. Abstract made in two languages written with the Bookman Old Style 9 pt. If the paper written in Indonesian, the Indonesian abstract written first then followed by English abstract and vice versa. The title "ABSTRAK" or "ABSTRACT" made with uppercase letters, and bold.

Keywords: *guidence, author, journal* ⟵ *(minimal 3 keywords)*
(10,5pt, Bookman Old Style, italic)

ABSTRAK
(10,5 pt, Bookman Old Style, bold)

Abstrak merupakan ringkasan elemen-elemen terpenting dari naskah, ditulis dalam satu paragraf dalam 1 kolom maksimal 200 kata. Abstrak dibuat dalam 2 bahasa ditulis dengan huruf 9 pt, Bookman Old Style. Apabila naskah dalam Bahasa Indonesia, maka abstrak dengan Bahasa Indonesia ditulis terlebih dahulu dilanjutkan abstrak Bahasa Inggris dan sebaliknya. Judul "ABSTRAK" atau "*ABSTRACT*" dibuat dengan huruf besar, *bold*.

Kata kunci: *panduan, penulis, jurnal* ⟵ *(minimal 3 kata kunci)*
(10,5pt, Bookman Old Style, italic)

1. PENDAHULUAN
(10,5pt, Bookman Old Style, bold)

Naskah dapat ditulis dalam Bahasa Indonesia maupun Bahasa Inggris. Naskah diketik dalam Microsoft Word dengan 1 kolom untuk abstrak dan 2 kolom untuk isi. Ukuran kertas A4 dengan ukuran panjang (*height*) 29,7 cm, lebar (*width*) 21 cm dengan dimensi

Top 3 cm, *Bottom* 2,5 cm, *Inside* 2,5 cm, *Outside* 2 cm, *Gutter* 1 cm, *Header* 1 cm dan *Footer* 1 cm. Jenis Huruf Bookman Old Style 10,5 pt, dan spasi

(*line spacing*) 1. Panjang naskah tidak melebihi 10 halaman termasuk tabel dan gambar.

Kerangka Tulisan disusun dengan urutan : Judul, Identitas Penulis, Abstrak, Kata Kunci, Pendahuluan, Metode, Hasil Pembahasan, Kesimpulan, Ucapan Terimakasih, dan Daftar Pustaka.

2.   METODOLOGI
(10,5pt, Bookman Old Style, bold)

Menguraikan tentang metode yang digunakan dalam penelitian termasuk data, peralatan, teori, diagram alir, beserta lokasi penelitian.

2.1. Lokasi dan Data
(10,5pt, Bookman Old Style, bold)

2.2. Standarisasi data
(10,5pt, Bookman Old Style, bold)

2.3. Metode Penelitian
(10,5pt, Bookman Old Style, bold)

Persamaan matematis atau formula diberi nomor secara berurutan yang diletakkan di ujung kanan dalam tanda kurung. Apabila penulisan persamaan lebih dari satu baris maka penulisan nomor diletakkan pada baris terakhir. Penggunaan huruf sebagai simbol matematis dalam naskah ditulis dengan huruf miring (*Italic*) seperti *x*. Penjelasan persamaan diulas dalam naskah. Penurunan persamaan matematis atau formula tidak perlu dituliskan secara detil, cukup diberikan bagian yang terpenting, metode yang digunakan dan hasilnya.

$$RMSE = \sqrt{\frac{\sum_{i=1}^{n}(X_{obs,i} - X_{model,i})^2}{n}} \quad .....(1)$$

Disini X*obs* adalah nilai estimasi dan X*model* adalah nilai model. RSME ini merupakan perbedaan antara nilai-nilai model atau estimator dengan nilai sebenarnya yang diamati.

3.   HASIL PEMBAHASAN
(10,5pt, Bookman Old Style, bold)

Tabel dibuat ringkas dan diberi judul yang singkat tetapi jelas hanya menyajikan data yang esensial dan mudah dipahami. Tabel diberi catatan secukupnya, termasuk sumbernya, sehingga tabel mampu menjelaskan informasi yang disajikan secara mandiri. Setiap tabel diberi nomor secara berurutan dan diulas di dalam naskah. Judul tabel diketik dengan jenis huruf Bookman Old Style 10,5 pt dan pada tulisan "Tabel 1." "Tabel 2." dan seterusnya diketik tebal.

Tabel yang ukurannya melebihi satu kolom, maka dapat menempati area dua kolom. Tabel tidak boleh dalam bentuk "*picture*", harus dalam bentuk tabel. Judul tabel dituliskan pada bagian atas tabel, rata tengah dan diberi tanda titik (.) pada akhir judul tabel.

Gambar, Grafik dan Foto harus tajam dan jelas agar cetakan berkualitas baik. Semua simbol di dalamnya harus dijelaskan. Seperti halnya tabel, keterangan pada gambar, grafik atau foto harus mencukupi agar tersaji secara mandiri. Gambar, grafik dan foto harus diulas di dalam naskah. Seperti halnya tabel, gambar, grafik dan foto yang ukurannya melebihi satu kolom, maka dapat menempati area dua kolom. Gambar, grafik dan foto memiliki kedalaman minimal 300 dpi.

Gambar 3-1: Suasana saat uji terbang roket tipe RX122 di Pameungpeuk Garut Jawa Barat
(9pt, Bookman Old Style)

Tabel 3-1: PARAMETER HASIL SIMULASI BESARAN DERAU DAN NILAI OPTIMAL α
(9pt, Bookman Old Style)

Besaran Derau (± km)	Nilai Optimal α	RMSE Raw Data	RMSE Estimated
1.5	0.0194	0.8481	0.6215
2.5	0.0165	1.4530	0.6705
5	0.0150	2.8793	0.8665

4. KESIMPULAN

Hal-hal penting dalam naskah yang merupakan kesimpulan dari hasil penelitian atau kajian.

UCAPAN TERIMAKASIH

Wajib dituliskan penulis, ditujukan kepada pihak-pihak yang membantu penulis baik penyediaan data, pengerjaan data, serta Tim Redaksi Jurnal Teknologi Dirgantara.

DAFTAR RUJUKAN

Referensi hendaknya dari sumber yang jelas dan terpercaya. Setiap referensi yang tercantum dalam daftar pustaka harus dikutip (disitir) pada naskah dan sebaliknya setiap kutipan harus tercantum dalam daftar pustaka. Penulisan acuan dalam pembahsan sebaiknya menggunakan "sistem penulis-tahun" yang mengacu pada karya pada daftar pustaka. Kutipan buku dalam bentuk saduran untuk satu sampai dua penulis ditulis nama akhir penulis dan tahun. Contoh: Muhammad Nasir dituliskan (Nasir, 2009).

Referensi primer lebih dari 80 % dan diterbitkan dalam 5-10 tahun terakhir. Referensi yang dicantumkan dalam naskah mengikuti pola baku dengan disusun menurut abjad berdasarkan nama (keluarga) penulis pertama dan tahun publikasi, dengan sistim sitasi *American Physiological Association 6th Edition*. Contoh penulisan di dalam Daftar Pustaka adalah sebagai berikut :

Artikel dalam Jurnal (Jurnal Primer)

Nair, C.P.R., *et al.*, 2013. *Effect of Process Parameters on the Viscosity of AP/Al/HTPB Based Solid Propellant Slurry*, Journal of Energy and Chemical Engineering Vol. 1 Issue 1, 1-9.

Buku

Pack D., Barrett S., 2012. *Atmel AVR Microcontroller Primer: Progamming and Interfacing, Second Edition.* Publication of Synthesis Lectures on Digital Circuits and Systems, ISBN : 9781598295412.

Artikel bagian dari Buku

Berjak, P., J.M. Farrant, D.J. Mycock and N.W. Pammenter. (1989). *The basis of recalcitrant seed behavior.* 98-112 pp. In Talorson, R.B. (ed.) *Recent advances in the development and germination of seeda.* Plenum Press, New York.

Skripsi/Tesis/Disertasi

Aziz, N. (2006). *Analisis Ekonomi Alternatif Pengelolaan Ekosistem Mangrove di Kecamatan Barru, Kabupaten Barru.* Tesis Sekolah Pascasarjana Institut Pertanian Bogor. Bogor. 105 hlm.

Naskah Prosiding

Wibowo, H. B., 2010. *Pengaruh Berat Molekul Terhadap Reaksi Pembentukan Poliuretan*, Prosiding SIPTEKGAN XIV-2010, November 2007, ISBN 978-978-1458- 08-05.

Naskah Konferensi

Torabi, H. B., & Sadi, M., 2011. *Solar Power System for Experimental Unmanned Aerial Vehicle (UAV); Design and Fabrication*, Paper presented at the Power Electronics, Drive Systems and

Technologies Conference (PEDSTC), 2011 2nd.

Naskah Laporan Hasil Penelitian

Koeshendrajana, S., Priyatna, F N. dan Mulyawan, I. (2008). *Riset Identifikasi, Karakterisasi dan Valuasi Sosial Ekonomi Sumber daya Perairan Umum Daratan.* Laporan Teknis Kegiatan Penelitian. Balai Besar Riset Sosial Ekonomi Kelautan dan Perikanan No. 10: 8-29. BRKP. Jakarta.

Naskah *Online*

Heein Yang, Sang-Burm Ryu, Hyun-Chul Lee, Sang-Gyu Lee, Sang-Soon Yong, JaeHyun Kim, *Implementation of DDS Chirp Signal Generator on FPGA*, Ajou University, Suwon. http://winner.ajou.ac.kr/publicatio/ data/conference/1570016207.pdf diunduh: 20 Maret 2015.